UNIVERSITÀ DEGLI STUDI DI PALERMO
Dottorato in Ingegneria dell'Innovazione Tecnologica
Dipartimento di Ingegneria
SSD: MAT/08

ADVANCED MESHLESS NUMERICAL METHODS AND APPLICATIONS

LA DOTTORESSA
MARTA PALIAGA

IL COORDINATORE
CH.MO PROF. ANTONIO CHELLA

IL TUTOR
CH.MO PROF. ANTONIO CHELLA

CO TUTOR
PROF.SSA ELISA FRANCOMANO

CICLO XXXI
ANNO CONSEGUIMENTO TITOLO 2019

Alla mia famiglia

Acknowledgements

I wish to thank Prof. Antonio Chella for being my supervisor during my PhD studies.
I would like to express my deeply-felt gratitude to Prof. Elisa Francomano, whose patient guidance, valuable suggestions and constant encouragement make me finishing my PhD thesis.

Contents

List of Figures

List of Tables

Chapter 1

Introduction

The object of this thesis is the analysis, the improvements and the applications of particular numerical strategies with the common idea to avoid the use of a mesh, upon which to discretize the governing problem domain. The studies on these methods, usually called *meshless*, are motivated by the important role that in these years they have been gained, not only in applied mathematics but in the engineering field. Thanks to their flexibility, they are largely used in multi-disciplinary areas of science. Namely, they can treat with problems in high dimension, scattered data approximation and problems defined over manifolds.

The meshless approximation methods have being studied by many researchers and nowadays fall under many names, including *meshfree, gridless, gridfree, Moving Least Squares (MLS), Partition of Unity (PU) or Smoothed Particle Hydrodynamics (SPH).* Despite their varied names, all these numerical approaches provide an essential functional structure, thus they can be analyzed or generalized independently on the particular problem studied.

These methods present a valid alternative to the widely used grid strategies such as the finite difference (FDM), finite volume (FVM), finite element (FEM), and the strategies for coupling them.

While these traditional schemes have directly impacted engineering and scientific developments, the state of art in computation investigations coupled with the increasing performance of moderns computers, has exposed the limitations of these conventional numerical methods. In fact, they have relied on the use of elements, grid or underlying structures to approximate the geometry of the problem domain. The construction of these lattices either limits the ability to handle very large deformation process or complicated modeling. Therefore, to avoid the overwhelming time consuming strategies in generating and maintaining high quality grids, the meshless methods represent an appealing and valid alternative to facilitate the numerical simulations that traditional schemes are incapable of modeling. In fact, the meshless strategies are based only on a set of independent points that are not linked to the others by a connectivity law, making the numerical applications better suited to cope with high dimensional data, irregular spatial domains or complex changes in the geometry of the domain of interest (e.g., free surfaces and large deformations).

In this thesis we investigate on some of these methods, introducing them into biomathematics context, to better understand some behaviors, and in approximating functions and its derivatives.

In the first part we deal with dynamical systems modeled by ordinary differential equations (ODEs). They are governed by suitable parameters, representing the most important relations between the variables. These models are deterministic, therefore, by fixing the values of the parameters, the solutions evolve toward the stable configuration, depending on the initial conditions.

Many models are multi-stable, i.e. they admit more than one possible final configuration. In real applications a stable point could represent an unfavorable condition, such as the extinction of a species or a virus spread. Therefore, it is fundamental to analyze the basins of attraction of these stable states, in order to avoid unpleasant outcomes. To accomplish this task, we have developed a method to reconstruct the surface between two different basins of attraction, called separatrices.

Starting from a bisection method proposed in literature [21], we present a new efficient strategy to detect the scattered points lying on the separatrix manifold. Moreover, dealing with a scattered data problem, we reconnect and reconstruct the surfaces by employing a Moving Least Squares (MLS) meshless method.

In Chapter 2 we resume some important theoretical basis of the dynamical analysis. Then, the bisection method to detect the separatrix points, is presented. To reconstruct the surfaces, we consider the Moving Least Squares algorithm by means of compactly supported radial basis functions. These particular functions have no prefer direction but only depend on norms in space (usually Euclidian). Therefore, a problem involving many space dimensions is converted into one that is virtually one dimensional.

In Chapter 3 we show the importance of the algorithm developed, by analyzing the Allee effect in a particular eco-epidemiological model. First, we give some backgrounds about the different classification of the Allee effect, then we analyze the dynamics of the model considering the bifurcation studies. Finally, we reconstruct the separatrix for different values of the parameters, underlying the most important process driving the eco-system dynamics.

Chapter 4 provides a new formulation to detect the threshold points, involving the invariant manifolds of the saddle points. This algorithm reduces the computational cost and it could be applied to multi-stable systems with any number of stable configurations and, more important, with complex attractors such as tori and limit cycle. Several models are analyzed to validate the new strategy.

The second part of this thesis is devoted in studying the Smoothed Particle Hydrodynamics (SPH) method, widely used in applications involving Partial Differential Equations (PDEs).
Many scientific process are modeled by means of PDEs equations or systems. Unfortunately, the exact solution of these models is very difficult or even impossible to find, making the numerical approximation fundamental to many applied scientists. The SPH was one of the first meshless method developed to substitute the classical grid methods in approximate the solutions for astrophysics problems. Since it has a long history, many improvements have been proposed to make the approximation more stable and accurate. However, the method still suffers of drawbacks treating non uniform distribution of points and in dealing with boundary evaluations. Here we work with a modified SPH method (M-SPH) to restore the accuracy of the standard procedure, in approximating a function and its derivatives.

In Chapter 5, after an overview on Meshless Particle Methods (MPMs) and the standard SPH, the improved algorithm is proposed. It provides simultaneously an approximation of a function and its derivatives with the desired accuracy by means of Taylor series expansion. Several numerical experiments, with different bi-variate test functions and different data distribution are provided, in order to test the validity of the M-SPH approach. We give evidence of the accuracy and convergence.

Finally in Chapter 6 some computational skills of the modified formulation are reported. By considering that the M-SPH formulation is more demanding than the standard one, requiring many summations on the employed RBFs and derivatives too, some efforts are performed with the aim to reduce the overall complexity. Fast transforms are taken into account, and the Improved Fast Gauss Transform (IFGT) is adapted to assembly the corrective linear system for each evaluation point.

Most of the contents of this thesis was presented at international conferences and published or accepted for publication.
In particular, the algorithm and the results presented in Chapter 2 and Chapter 3 are published in [35, 36, 37, 58]. The extended results on the invariant manifold discussed in Chapter 4 are published in [34, 38]. Finally, the second part of the thesis is the object of the papers [39, 40].
All the algorithms introduced and tested in this thesis have been implemented in MATLAB. The bifurcation and stability analysis of the model in [58] it was conducted with the XPPAUT program.

Chapter 2

Separatrix Reconstruction

In this chapter we will present briefly the fundamental elements of the analysis of the dynamical systems and their applications in bio-mathematical field.
The first part is organized to give the ground floor where the following results are rooted and to clarify the notation used. In this view, we will concentrate only on the basic definitions, that are fundamental for the following discussion.
We will introduce the problem of the basins of attraction analysis, focusing on the importance of the separatrix reconstruction. Finally a Moving Least Squares meshless method is presented to deal with the scattered data approximation.

2.1 Mathematical Modeling

In the last decades, mathematical modeling becomes a fundamental tool for the qualitative analysis of several natural phenomena. The unifying aim of theoretical description and experimental investigation is to analyze and to justify specifics processes explaining their intrinsic logic [65, 85]. The mathematical modeling translates the world process observed into a rigorous scientific language.
These models are applied for a several number of different reasons. Example of the range objectives are: developing scientific understanding, test the effect of changes in a system and decision making. Of course, the majority of the interactive process in the real world are far too complicated to be modeled their entirety. Therefore, analyzing a phenomena, the idea is to describe and to understand the fundamen-

tal mechanism, capturing the essence of various interactions, in order to obtain a predictive science that studies the possible outcomes.

In this scenario, the mathematical analysis represents a bridge between the experimental data measured and patterns describing in general the fundamental variable interactions.

There are two different approaches in modeling: deterministic and stochastic. In the first case, the random variations are ignored, therefore, starting from a fixed starting condition, the predictive evolution is always the same. On the other hand to describe the randomness presents in nature, the statistical model predicts the distributions of different outcomes.

In both cases the equations of the model depend on suitable parameters to describe the interactions between the variables that we want to describe.

In this part of the thesis we will focus on the analysis of the deterministic dynamical systems modeled by ordinary differential equations, ODEs, to study eco-epidemiological interactions. The dynamical theory is largely used to study the biological process in order to preserve the biodiversity of an eco-systems, to eradicate pest species or even in medicine to study the growth of the cancer cells or diseases spread.

Even if we focus our attention only on bio-mathematics field, the results that we will present could be applied in other field of science such as physics, engineering and even social science.

2.2 Dynamical systems

In mathematics, a dynamical system is a model describing the time dependence of a variable in a geometrical space.

The relation between the variables involved is either a differential equation or difference equation of other time scale. Our research is focused on continuous systems of ordinary differential equations:

$$\dot{\mathbf{x}} = f(\mathbf{x}) \quad \mathbf{x} \in M \subseteq \mathbb{R}^n, \tag{2.1}$$

where M is an open set called *phase-space*, i.e. the space where all motions

happen and $f : M \to \mathbb{R}^n$ is a vector field that we assume to be $f \in \mathcal{C}^1$.
To determine the state for all future times, it is required to re-iterate the function f. This iterative procedure, is referred to as "solving the system" or "integrating the system". If the model can be solved, given an initial state $\mathbf{x}_0$, we can determine all its future positions, i.e. the orbit of the point $\Phi^t(\mathbf{x}_0)$, where $\Phi : \mathbb{R} \to \mathbb{R}$ is an invertible map. The set of all these maps:

$$\Phi = \left\{ \Phi^t(\mathbf{x}) | t \in \mathbb{R} \right\},$$

is called *flow* of the system.
The dynamical theory is focused on the asymptotic behavior, meaning that the principal goal is the analysis of the different trajectories when $t \to +\infty$. This study allows to generalize and to predict the possible outcomes of the variables studied, rather than consider only a particular interval of time.
Starting from different initial states and by changing the parameter values, the system evolutions may be very different and lead to unfavorable conditions. To understand the possible outcomes of the model, the first step is looking for fixed states and to analyze their stability [52, 65].

Definition 1.
Given an autonomous system of ordinary differential equations $\dot{\boldsymbol{x}} = f(\boldsymbol{x})$*, an equilibrium or critical point* $\boldsymbol{x}^*$ *is a solution that does not change in time:*

$$\Phi^t(\boldsymbol{x}^*) = \boldsymbol{x}^* \quad \forall t \in \mathbb{R}.$$

The equilibrium points are the only one, whose trajectories are represented by the points themselves. Now, the question is what happens when we consider trajectories starting from initial states close to the fixed points. Namely, how change the system for small perturbations. If the trajectories remain close to the fixed point, it is called *stable*, in particular, if they collapse to the point, then it is *asymptotically stable.* Otherwise it is *unstable* [74].

Definition 2.
An equilibrium $\boldsymbol{x}^*$ *to an autonomous system of first order ODEs, is Lyapunov stable if*
$\forall \epsilon > 0, \exists \delta > 0$ *such that, if* $||\boldsymbol{x} - \boldsymbol{x}^*|| < \delta$ *then* $||\Phi^t(\boldsymbol{x}) - \boldsymbol{x}^*|| < \epsilon, \forall t > 0$*.*
It is Lyapunov asymptotic stable if
$\forall \epsilon > 0, \exists \delta > 0$ *such that if* $||\boldsymbol{x} - \boldsymbol{x}^*|| < \delta$ *then*

$$\lim_{t \to \infty} \Phi^t(\boldsymbol{x}) = \boldsymbol{x}^*.$$

Once the critical points are found the analysis of stability is conducted considering the system (2.1) in matrix form

$$\dot{\mathbf{x}} = \mathbf{A}\mathbf{x} \tag{2.2}$$

where $\mathbf{x} \in \mathbb{R}^n$ and A is a $n \times n$ matrix with real entries.
Assuming a linear vector field, the system has a constant solution at the origin: $\mathbf{x} = 0$. This solution is asymptotically stable, if and only if all eigenvalues λ of the matrix have negative real part: $Re(\lambda) < 0$. On the contrary if all the eigenvalues have positive real part, the origin is unstable. In Figure 2.1 it is shown the classification of critical points in $2D$ vector field with eigenvalues having the same signs. When the eigenvalues are complex the trajectories spiral around the point. In Chapter 4 a more detailed classification of the equilibrium point will be addressed, considering the case of the eigenvalues with opposite signs.
These results on the stability analysis can be generalized to non-linear ODEs system, thanks to the Hartman-Grobman theorem [50, 56].

Theorem 1 (Hartman-Grobman)**.**
Let (2.1) be a non-linear system with f *a smooth map with an hyperbolic equilibrium point* $\boldsymbol{x}^* \in M$*. Then there exists a neighborood* U *of* $\boldsymbol{x}^*$ *and an homeomorphism* $h : U \to \mathbb{R}^n$*, such that* $h(\boldsymbol{x}^*) = 0$ *in* U *and the flow of the system is topological conjugate by the continuous map* $N = h(u)$ *to the flow of its linearization* $\frac{dN}{dt} = AN$*.*

This theorem asserts that analyzing the Jacobian matrix associated to the system and the relative eigenvalues we have information about the local behavior around the equilibrium point of a non-linear system. In particular, it works only if the

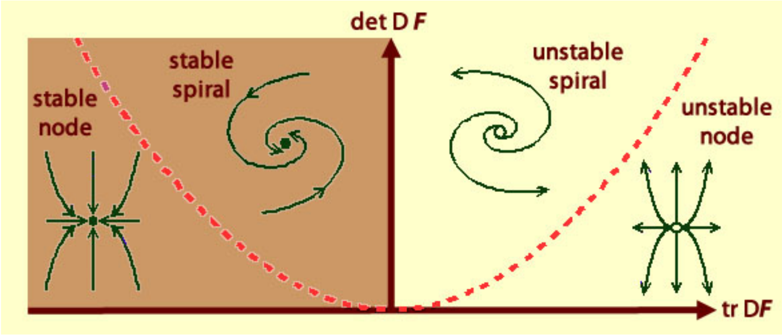

Figure 2.1: Classification of equilibrium points in a $2D$ vector field depending on the eigenvalue sign.

fixed states are assumed to be hyperbolic points, i.e. with no purely imaginary eigenvalues. Therefore, the attractive or repulsive direction depends only on the relative eigenvalues with negative or positive real part respectively (Figure 2.1). From now on, we assume that all the points have no eigenvalues with zero real part and these features will be fundamental for the future discussion in Chapter 4.

If the model admits only one stable configuration, the analysis is rather banal and simple because all the trajectories evolve toward that state. On the contrary, the analysis of the multi-stable models results more complex and interesting, namely the systems admitting more than one stable equilibrium simultaneously [51, 60, 65, 77, 88, 96, 102]. In this case the phase-space is partitioned into the basins of attractions of the equilibria, i.e. the sets of initial conditions evolving toward the corresponding stable configuration. The study of these domains of attraction is important in the research to avoid or to prevent an unfavorable outcomes, such as the growth of the cancer cell [18] or the extinction of a species [58]. Often the physical or biological phenomena studied are not in isolated systems, in this case such systems can shift abruptly from one state to another, a phenomenon also known as *ecological regime shift*. Well-known examples include shifts from clear to turbid waters [19], from grassland to shrubland [92], the collapse of fisheries [87], and the degradation of coral reefs [84].

In mathematical representation, modeling these shifts means change the values of the parameters or the initial state variables [11]. In the first case, it is described a change on the eco-system characteristics, therefore the relations between the variables are different. Changing the parameters could lead to new configuration, i.e. the appearance (or disappearance) of alternative stable states.

In the second case the systems are already multi-stable but an overcritical disturbance of the system causes unpredictable shifts from one basins of attraction to another.

For example, there are climatic factors, like the Indian Ocean Dipole and El Nino Southern Oscillation [10, 86], becoming more unpredictable and less regular because of the global warming. These changes makes harder to live in this environment. As consequence, the animal survival is jeopardised and this could lead to not have necessary newborns to avoid the decline of the population. Thus, it is important to understand the necessary density for survival in order to prevent the loss of biodiversity in the eco-system.

The *tipping points*, i.e. the boundary values between two basins of attraction, represent the most sensitive states to these changes. As regime shifts often imply catastrophic consequences for the ecosystem, failure to recognize alternative stable states or wrong predictions of these threshold points can turn out not only as a surprise, but also costly.

A complete knowledge of the existence and location of tipping points is fundamental for understanding and managing models [17, 19, 34, 75]. There is a need of methods that help in accomplishing this task. In this thesis, we provide a numerical tool to locate the boundary points and to reconstruct the relative separatrix manifold, which separates two domains of attraction.

2.3 Detection Problem

To analyze and to reconstruct the domains of attraction, the first goal is to find the tipping points lying on the separatrix manifold. In a simple system with only one state variable, the separatrix point corresponds to the unstable equilibrium collocated between the two stable steady states. However in higher dimensional systems, information about the separatrix is needed. In particular, the tipping point of a certain state variable is not anymore a single value for a given set of parameters, but it depends on the values of the other state variables as the separatrix is a higher dimensional object.

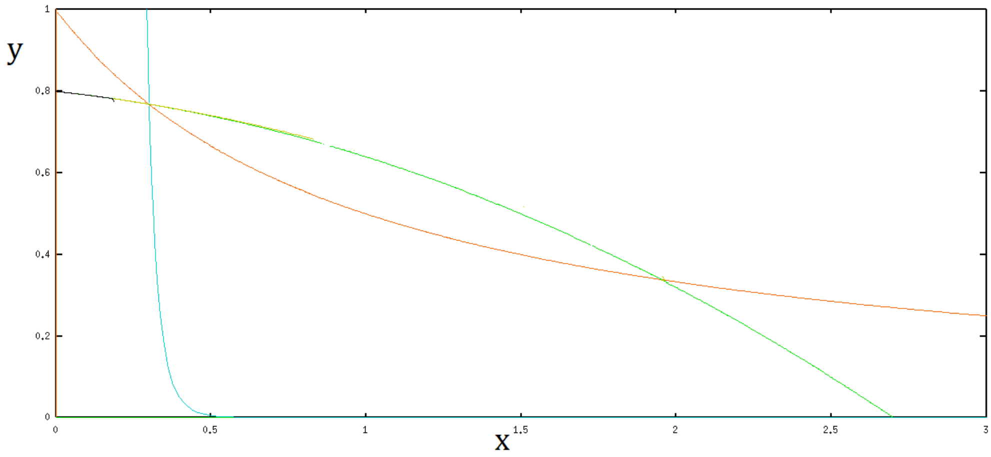

Figure 2.2: Phase-space of a planar model computed in XPPAUT. The green line represents the x-nullclines. In red the y-nullclines. The blue curve is the separatrix between the two stable points.

There are some packages such as MATCONT or XPPAUT that are capable to reconstruct the separatrix curves in bi-dimensional systems. In Figure 2.2 is depicted an example of a planar model analyzed by using XPPAUT. In this thesis we focus our study on the analysis of three dimensional dynamical systems with a particular interest on the eco-epidemiological models.

Our research starts from the method proposed in [21], in which a bisection algorithm is presented to detect the separatrix points with the desired accuracy.

2.3.1 Bisection Method

The bisection method has been presented for the first time in [21] to analyze the basins of attraction of a bi-dimensional competitive model with two different stable equilibria.

The algorithm starts considering a square domain with edge $l \in \mathbb{R}$: $[0, l]^2$, on the plane of the trajectories (x, y), i.e. the phase-portrait. Then a grid of $N \times N$ points is built, where N is the number of subdivision points in the interval $[0, l]$.

When the biological parameters are fixed, the evolution of the trajectories is unique and it depends only on the initial states (Figure 2.3A). Thus, the bisection routine

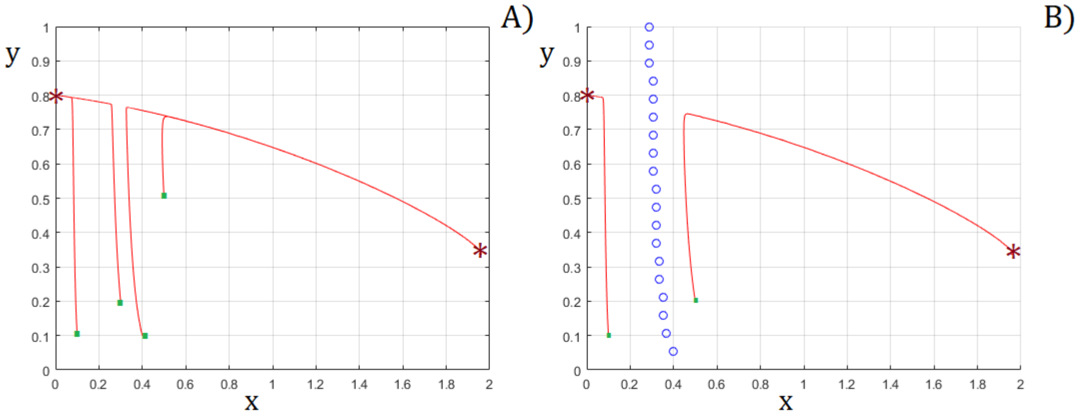

Figure 2.3: A) Some trajectories computed starting from different initial conditions (red curves). The green squares represent the starting points. The stars are the stable states. B) The separatrix points detected with bisection method are depicted in blue.

is applied to the following pairs of initial conditions

$$\begin{aligned} &(x_j, 0) \text{ and } (x_j, l), \quad j = 1, ..., N, \\ &(0, y_j) \text{ and } (l, y_j), \quad j = 1, ..., N. \end{aligned}$$

The orbits of these points are integrated. If they reach different equilibrium points then the bisection method is applied, i.e. the midpoint is the new initial state and the procedure is iterated until the required accuracy is obtained (Figure 2.3B).

Later, this procedure was extended to three dimensional systems with two or three stable fixed points [20, 22, 23, 24].

The idea is the same as the planar models. In this case a cubic domain is considered: $[0, l]^3$ and the bisection routine is applied to the following pairs of initial conditions

$$\begin{aligned} &(x_j, y_k, 0) \text{ and } (x_j, y_k, l), \quad j, k = 1, ..., N, \\ &(x_j, 0, z_k) \text{ and } (x_j, l, z_k), \quad j, k = 1, ..., N, \\ &(0, y_j, z_k) \text{ and } (l, y_j, z_k), \quad j, k = 1, ..., N. \end{aligned}$$

Of course, the fixed points have to be excluded from the initial conditions, because their orbits are the points themselves. Once that a sufficient number of separatrix points are detected, the authors use a Partition of Unity method to reconstruct the manifold.

Our studies begin by adopting the bisection procedure to find the tipping points, whilst a quasi-interpolant scheme has been considered to reconstruct the manifold. Namely, a Moving Least Square approximant, based on explicit formula of the Lagrange multipliers, is used to avoid the setting up of the interpolation system. The quasi-interpolant is formulated by means of compactly supported radial basis functions, providing a local approximation of each evaluation point and we will discuss in details on it in the next section.

2.4 Moving Least Squares approximant

The general Moving Least Squares method (MLS) is appeared in the approximation theory literature in the paper [64], whose authors also pointed out the connection to the earlier more specialized work of Shepard [97].

This scheme belongs to the class of meshless method that does not need the construction of any grids, making it suitable even in problems with complex domains and applicable in different area of science.

The idea of this method is to solve for each evaluation point a locally weighted least squares problem. At first, it seems to be rather expensive, however is proved to be an efficient method and it could be parallelized. Moreover in many applications, like the one considered in this work, it is not required a large number of evaluations.

In the literature there are many different approaches and representations of the moving least squares method [6, 32, 61, 64, 109]. Here we propose a discussion similar to the one in [64], following the Backus-Gilbert approach [6] reported in the monography [32].

Given a discrete set $\chi = \{\mathbf{x}_1, ..., \mathbf{x}_N\} \subset \mathbb{R}^d$ of data sites and knowing the evaluations $\{f(\mathbf{x}_1), ..., f(\mathbf{x}_N)\}$ of the function f at these points, we construct the quasi-interpolant

$$P_f(\mathbf{y}) = \sum_{i=1}^{N} f(\mathbf{x}_i)\Phi_i(\mathbf{y}), \tag{2.3}$$

where $\Phi_i(\mathbf{y}) = \Phi(\mathbf{y}, \mathbf{x}_i)$ are the *generating functions* that govern the approximation goodness.

If we consider a linear space generated by the linear function $\{\Phi_1, ..., \Phi_N\}$ to approximate the given measurements $\{f_1, ..., f_N\}$, we can find the coefficients $\{a_i\}_{i=1}^{N}$, to construct the interpolant

$$P_f(\mathbf{y}) = \sum_{i=1}^{N} a_i\Phi_i(\mathbf{y}), \tag{2.4}$$

such that $P_f(\mathbf{x}_i) = f(\mathbf{x}_i)$. In particular, if Φ_i are the cardinal functions, i.e. $\Phi_i(a_j) = \delta_{ij}$, then the coefficients are the given data: $a_i = f(\mathbf{x}_i)$. In general the MLS method considers a general space of generating functions to obtain an approximant instead of an interpolant. In this way it is not necessary to set up and to solve a possible large interpolation system to find the coefficient a_i.

Of course, it is necessary to find the best set of functions Φ_i to obtain a good fitness to the data. In the Backus-Gilbert formulation the goal is not to minimize the point-wise error but instead finding the generating functions that minimize the quantity

$$\frac{1}{2}\sum_{i=1}^{N} \Phi_i^2(\mathbf{y})\frac{1}{\omega(\mathbf{x}_i, \mathbf{y})}, \tag{2.5}$$

where ω is the weight function governing the data influence. In our application we choose the radial basis functions with compact support.

Therefore $\omega_i(\mathbf{x}) = \omega(\mathbf{x}_i, \mathbf{y})$ are strictly positive in a sub-domain Ω_i containing $\mathbf{x}_i$, but they are zero outside. This domain is called the *domain of influence* of the node $\mathbf{x}_i$. Specifically

$$\forall \mathbf{x}, \mathbf{y} \in \mathbb{R}^d \quad \omega_\epsilon(\mathbf{x}, \mathbf{y}) = 0 \ if \ ||\mathbf{x} - \mathbf{y}||_2 > \epsilon, \tag{2.6}$$

where ϵ is the so-called *shape parameter* indicating the domain size (Figure 2.4) and which influences the approximation goodness.

To ensure that the quasi-interpolant P_f achieves a certain approximation power,

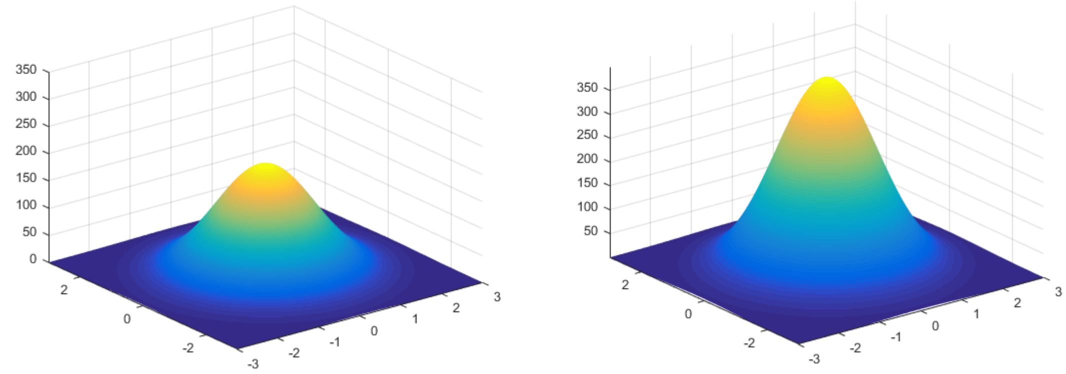

Figure 2.4: Weight Radial Basis Function (Gaussian) with $\epsilon = 0.5$ (left) and $\epsilon = 1$ (right)

it is required that the generating functions Φ_i, reproduce polynomials of a certain degree q. Thus they are subject to the constraints

$$\sum_{i=1}^{N} p(\mathbf{x}_i)\Phi_i(\mathbf{y}) = p(\mathbf{y}) \quad \forall p \in \mathbf{\Pi}_q^d, \tag{2.7}$$

where $\mathbf{\Pi}_q^d$ is the space of the d-variate polynomials of total degree at most q with dimension $Q = \frac{(d+q)!}{q!d!}$,spanned by the monomial basis functions: $\{p_1, ..., p_Q\}$.
By considering the vector $\Phi(\mathbf{y}) = [\Phi_1(\mathbf{y}), ..., \Phi_N(\mathbf{y})]^T$ we can rewrite (2.5) as follows

$$\frac{1}{2}\mathbf{\Phi}^T(\mathbf{y})\mathbf{W}(\mathbf{y})\mathbf{\Phi}(\mathbf{y}), \tag{2.8}$$

$$\text{with} \quad \mathbf{W}(\mathbf{y}) = diag\left(\frac{1}{\omega(\mathbf{x}_1, \mathbf{y})}, ..., \frac{1}{\omega(\mathbf{x}_N, \mathbf{y})}\right), \tag{2.9}$$

and the linear polynomial constraint (2.7) becomes

$$\mathbf{A\Phi}(\mathbf{y}) = \mathbf{p}(\mathbf{y}), \tag{2.10}$$

with $A_{ki} = p_k(\mathbf{x}_i)$, $k = 1, ..., Q$, $i = 1, ..., N$ being the entries of matrix A and $\mathbf{p} = [p_1(\mathbf{y}), ..., p_Q(\mathbf{y})]^T$ being the known vector. The generating functions Φ satisfying

(2.8) and (2.10) are given by [32, 109]:

$$\Phi_i(\mathbf{y}) = \omega(\mathbf{x}_i, \mathbf{y}) \sum_{k=1}^{Q} \lambda_k p_k(\mathbf{x}_i) \quad i = 1, ..., N, \tag{2.11}$$

where λ_k are the Lagrange multipliers, i.e. the only solutions of the system

$$\sum_{k=1}^{Q} \lambda_k \sum_{i=1}^{N} \omega(\mathbf{x}_i, \mathbf{y}) p_k(\mathbf{x}_i) p_q(\mathbf{x}_i) = p_q(\mathbf{y}) \quad 0 \leq q \leq Q. \tag{2.12}$$

Therefore, by considering the vector $\Lambda = [\lambda_1, ..., \lambda_N]^T$, and by letting $K(\mathbf{x}_i, \mathbf{y}) = \omega(\mathbf{x}_i, \mathbf{y}) \Lambda^T(\mathbf{y}) p(\mathbf{x}_i)$, the quasi-interpolant is

$$P_f(\mathbf{y}) = \sum_{i=1}^{N} f(\mathbf{x}_i) K(\mathbf{x}_i, \mathbf{y}). \tag{2.13}$$

In order to improve the stability of the method, the polynomials are centered on the evaluation points, i.e. $p(\mathbf{x}_i) = p(\mathbf{y} - \mathbf{x}_i)$ so that only $p_1(\mathbf{y}) \equiv 1 \neq 0$ [32, 109]. Constructing the quasi-interpolant (2.13), most of the computational cost is for the estimation of Lagrange multipliers λ_k, requiring the solution of system (2.12) for each evaluation point $\mathbf{y}$. This appears to be quite expensive, but there are two important factors to consider.

First, for our purpose, to reconstruct the surface we do not need a large number of evaluation points. Second, the linear polynomial reproduction ($q = 1$) will show to be of approximation order $\mathcal{O}(h^2)$, and it is accurate enough in our contest [32]. Since we are in $\mathbb{R}^2$, the linear system (2.12) that we have to solve is

$$G(\mathbf{y}) \lambda(\mathbf{y}) = p(\mathbf{y}), \quad \mathbf{y} \in \mathbb{R}^2, \tag{2.14}$$

where G is the Gram matrix with entries $G_{jk}(\mathbf{y}) = \sum_{i=1}^{N} p_k(\mathbf{x}_i) p_l(\mathbf{x}_i) \omega(\mathbf{x}_i, \mathbf{y})$ and $j, k = 1, .., 3$.

Thanks to the low dimension of the problem, in the computation we use Maple to find the explicit formula for the Lagrange multipliers

$$\begin{aligned}\lambda_1(\mathbf{y}) &= \frac{1}{|G|}(G_{11}^2 - G_{22}G_{33}),\\ \lambda_2(\mathbf{y}) &= \frac{1}{|G|}(G_{12}G_{31} - G_{13}G_{23}),\\ \lambda_3(\mathbf{y}) &= \frac{1}{D}(G_{22}G_{13} - G_{13}G_{23}).\end{aligned}$$

In this way the solution of the linear system is avoided at all and for each evaluation point $\mathbf{y}$ the computational cost is at most:

$$O(Q^3 + Q^2 N_y + QN_y), \tag{2.15}$$

where N_y is the number of data sites inside the support of the weighted functions $\omega(\cdot, \mathbf{y})$ [109].

2.4.1 Estimation Error

To derive the point-wise error estimates it is considered the polynomial reproduction property of the generating functions [32]. Therefore we obtain

$$\begin{aligned}|f(\mathbf{x}) - P_f(\mathbf{x})| &\leq |f(\mathbf{x}) - p(\mathbf{x})| + |p(\mathbf{x}) - \sum_{i=1}^{N} f(\mathbf{x}_i)\Phi_i(\mathbf{x})| \leq\\ &\leq |f(\mathbf{x}) - p(\mathbf{x})| + |\sum_{i=1}^{N} p(\mathbf{x}_i)\Phi_i(\mathbf{x}) - \sum_{i=1}^{N} f(\mathbf{x}_i)\Phi_i(\mathbf{x})|, \quad (2.16)\end{aligned}$$

thus we have

$$|f(\mathbf{x}) - P_f(\mathbf{x})| \leq ||\mathbf{f} - \mathbf{p}||_\infty \left[1 + \sum_{i=1}^{N} \Phi_i(\mathbf{x})\right]. \tag{2.17}$$

To find the order of the approximation we have to discuss the upper bound of the quantities $||\mathbf{f} - \mathbf{p}||_\infty$ and $\sum_{i=1}^{N} \Phi_i(\mathbf{x})$.

Considering the $q - th$ order Taylor expansions of f centered at the point $\mathbf{x}$, we obtain that

$$||\mathbf{f} - \mathbf{p}||_\infty \leq Ch^{q+1}\max|D^\alpha f(\xi)|, \tag{2.18}$$

where the shape parameter is scaled, according to the fill distance

$$h_{\chi,\Omega} = \sup_{\mathbf{x}\in\Omega} \min_{\mathbf{x}_j\in\chi} \|\mathbf{x}_j - \mathbf{x}\|_2, \tag{2.19}$$

that gives a measure of the data distribution. To estimate the uniform bound for $\sum_{i=1}^{N}\Phi_i$ let's start considering the simplest case: $q = 0, d = 1$. In this case the quasi-interpolant obtained reproduces the constants and it is the so-called Shepard approximant

$$\sum_{i=1}^{N} f(\mathbf{x}_i)\Phi_i = \sum_{i=1}^{N} f(\mathbf{x}_i)\frac{\omega_i(\mathbf{x})}{\sum_{j=1}^{N}\omega_j(\mathbf{x})}, \tag{2.20}$$

satisfying that $\sum_{i=1}^{N}\Phi_i = 1$. Therefore

$$||f(\mathbf{x}) - P_f|| \leq 2||\mathbf{f} - \mathbf{p}||_\infty. \tag{2.21}$$

The authors in [109] extend the results for the general case, demonstrating that the moving least squares method that reproduces polynomials of degree q has an approximation error of $\mathcal{O}(h^{q+1})$. However some properties have to be satisfied in order to prove this result. In particular it is required a quasi-uniform distribution for the data sites and the weighted functions have to be compactly supported functions as we previously assumed.

2.5 Sketch of the algorithm

We are now ready to construct the separatrix manifold. We assume the data sites χ as the scattered separatrix points projected onto the (x, y) plane, while the data values $f_i = f(\mathbf{x}_i)$ describe the height at $\mathbf{x}_i$. Then we apply the MLS method just described in generating the local approximation.
The sketch of the overall algorithm is shown in the following:

- - $\mathbf{E} \in \mathbb{R}^{n\times 3}$: matrix whose rows contain the fixed points of the model.
- - **parameter** $\in \mathbb{R}^{1\times k}$: the parameters vector.
- - $\mathbf{l} \in \mathbb{R}$: the edge length of the cubic domain considered.

- - $\mathbf{t} \in \mathbb{R}$: size of integration interval.
- - $\mathbf{N} \in \mathbb{R}$: number of initial conditions on each axis.
- - $\mathbf{y} \in \mathbb{R}^{2\times M}$: matrix whose rows contain the evaluation points.

```
• STEP 1   Define the cubic domain $[0,l]^3$, and consider $h = 1,2,3$ the parallel cubic faces.
      STEP 1.1 Define the pairs of grid points on parallel faces:
               $P^h_{ij},\ i = 1,2,\ j = 1,...,N^2$.

• STEP 2   for $j = 1 : N^2$
      STEP 2.1   if $P^h_{1j}$ or $P^h_{2j}$ are in $E$ then return
      STEP 2.2     else if $P^h_{1j}$ and $P^h_{2j}$ tend toward different equilibrium
                     then SeparatrixPoints=Bisection($P^h_{1j}$,$P^h_{2j}$);

• STEP 3   Repeat STEP 2 changing $h$.

• STEP 4   Calculate the Lagrange multipliers using the explicit formula:
      $\lambda = LagrangeMultipliers(\mathbf{y}, SeparatrixPoints, \omega)$

• STEP 5   Find the MLS approximant:
               $P_f = MLS(\lambda, \mathbf{y}, Separatrixpoints, \omega)$
```

Chapter 3

Analysis of the Allee effect

In this chapter we will present a study on the Allee effect of a particular eco-epidemioligical model. The algorithm presented in the previous chapter will be employed to reconstruct the separatrix manifold, representing the Allee threshold. The obtained results show interesting insights that were not previously observed with a classical dynamical analysis.

3.1 Allee effect

In many biological systems animals exhibit social behavior: they use cooperative strategies to hunt or to fools predators [29, 30, 101], they forage together [63], they join forces to survive unfavorable conditions [8, 42] or simply they seek sexual reproductions at the same moment or place [14]. In the 1930s W.C. Allee discovered that the goldfish grow more rapidly when there are more individuals in the tank [5] and concluded that aggregation can improve the survival rate of individuals and that cooperation could be crucial for the evolution and survival of the species. The Allee effect describes the positive correlation between the population density and populations fitness (measured at the per-capita growth rate) [5, 28]. When there are too few individuals it may be that they will each benefit from more resources, but in many cases they will also suffer from a back conspecific. Thus, there is the possibility of extinction, if the population density falls below a critical value known as "*Alee threshold*" [13, 14, 28, 51, 75].

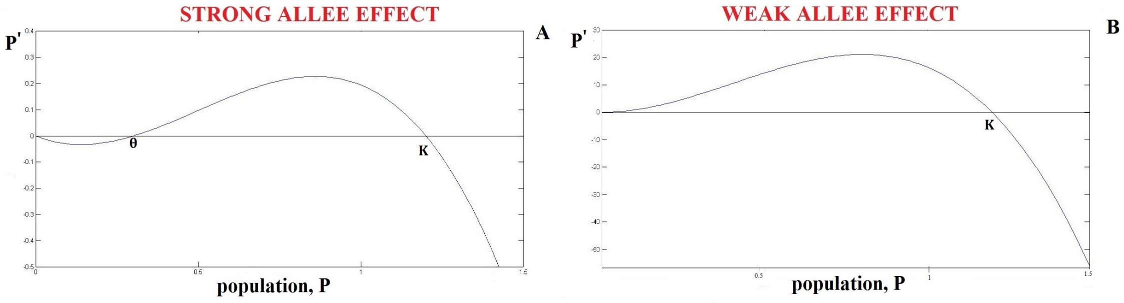

Figure 3.1: Study of the Allee effect on the plane (P, P^t). Strong Allee effect (A): the growth rate is negative for low density $(P < \theta)$. Weak Allee effect (B): the growth rate is always positive.

The Allee effects can be classified in Strong Allee effect with a critical population size and weak Allee effect without this critical threshold (Figure 3.1).

More than the weak effect, the strong one has obtained large attention especially in studying endangered species. In fact it is important the study of the critical quantity in order to protect the biodiversity or to guide eradication campaigns of pest species. Recently, many researchers have studied the impact of the Allee effects on population interactions as well as they interplay with disease on species establishment and persistence [8, 29, 36, 37, 42, 93, 104]. All these researches suggest the profound effects of the disease in population when it is coupled with the Allee effect [62].

In this chapter we recap an eco-epidemiological model introduced and analyzed in [58]. This combines disease transmission in a predator population with the ecological dynamics of a predator-prey system. In addiction the predators cooperate by hunting in packs.

Through the reconstruction of the separatrix manifold we will analyze the strong Allee effect induced by this cooperation. In fact, the critical density needed for survival corresponds to the tipping point between extinction and persistence. We will use the method presented in previous section, to study the changes of the Allee threshold when the biological parameters are varied.

3.2 Eco-epidemiological model

The eco-epidemiological model considered here is based on prey and predator populations with densities N and P, respectively. Because of the infectious disease the predator population is split into susceptible (S) and infected (I), with $P = S + I$. The population dynamics in time T can be described by a three-dimensional system of nonlinear ordinary differential equations:

$$\begin{aligned}
\frac{dN}{dT} &= r\left(1-\frac{N}{K}\right)N-\left(a_0+a_1P\right)NP,\\
\frac{dS}{dT} &= -\beta\frac{SI}{P}-mS+\epsilon\left(a_0+a_1P\right)NS+\left(1-\theta\right)\epsilon\left(a_0+a_1P\right)NI,\\
\frac{dI}{dT} &= \beta\frac{SI}{P}-mI-\mu I+\theta\epsilon\left(a_0+a_1P\right)NI.
\end{aligned}$$

It is assumed a logistic growth in prey, with K the carrying capacity and r being the per capita net growth rate. Predators grow by consuming prey and die with a natural per-capita death rate m. In order to model the cooperative hunting among predators, the functional response to prey is represented by the term

$$(a_0 + a_1P)N,$$

where a_0 is the density-independent predation rate corresponding to a linear functional response and a_1 represents the strength of hunting cooperation. Parameter ϵ is the efficiency with which predators consumed prey into their own growth. The disease transmission in the predator population is frequency-dependent, with β being the transmission parameter. Moreover, we assume that the mothers could pass the disease to the offspring, i.e. a vertical transmission, and $\theta \in [0, 1]$ is the fraction of offsprings acquiring infection from their mothers. Furthermore, infected predators are subject to an additional disease-related per-capita mortality μ.

All the variables and parameters involved in the mathematical modeling have different unit of measurement. Therefore before to analyze a dynamical system it is necessary non-dimensionalize.

First we perform a change of variables, which allows to deal with the singularity in the frequency dependent transmission and to distinguish the disease-induced extinction.

We replace the state variables S and I by the entire predator population $P = S + I$ and its prevalence $i = I/P$. Then we introduce the dimensionless quantities

$$n = \frac{\epsilon a_0}{m} N, \quad p = \frac{a_0}{m} P, \quad t = mT.$$

This leads to:

$$\begin{aligned} \frac{dn}{dt} &= r' \left(1 - \frac{n}{k'}\right) n - (1 + \alpha p)\, np, && (3.1) \\ \frac{dp}{dt} &= -\left(1 + \mu' i\right) p + (1 + \alpha p)\, np, && (3.2) \\ \frac{di}{dt} &= i\,(1 - i)\,(\beta' - \mu') - (1 + \alpha p)\,(1 - \theta)\, ni, && (3.3) \end{aligned}$$

where

$$r' = \frac{r}{m}, \quad k' = \frac{\epsilon a_0 K}{m}, \quad \alpha = \frac{m a_1}{a_0^2}, \quad \mu' = \frac{\mu}{m}, \quad \beta' = \frac{\beta}{m}$$

are dimensionless parameters. In particular we will focus our analysis on the relation between the parameters β and α, representing the transmissibility of the infection and the strength of predator cooperation, respectively. To simplify the notation, from now on, we drop the dashes appearing in the parameters.

Solving for the equilibria of model (3.1)–(3.3), and through the analysis of the Jacobian matrix and its eigenvalues, the study of the stability is conducted. In Table 3.1 there are resumed all the fixed steady states and the parameter conditions for the stability.

An important quantity in the stability analysis is the basic reproduction number of the disease in the predator population,

$$R_0 = \frac{\beta}{\mu + (1 - \theta)k}, \tag{3.4}$$

which gives the number of secondary infections caused by a single infected predator during its lifetime when the predator–prey system is at disease-free coexistence equilibrium. Depending on the value of this quantity we can distinguish two cases. If $R_0 < 1$, the infection will disappear in the long run. In this case, the model reduces to the disease-free predator–prey system with predator cooperation. On

Table 3.1: Equilibria of model (3.1)–(3.3) and their existence and stability conditions. $\beta_c = k(1-\theta) + \mu$

Equilibrium	Meaning	Existence	Stability
$E_0 \equiv (0,0,0)$	Extinction of all species	Always	Unstable
$E_n \equiv (k,0,0)$	Prey only	Always	Unstable
$E_i \equiv (0,0,1)$	Extinction of all species	Always	$\beta < \beta_c$
$E_{ni} \equiv (k,0,1-\frac{(1-\theta)k}{\beta-\mu})$	Disease-induced predator extinction	$\beta > \beta_c \vee \beta < \mu$	$\beta > \beta_c$
$E_{np} \equiv (n^*,p^*,0)$	Disease-free coexistence	-	-
$E_{npi} \equiv (n^*,p^*,\frac{\beta-\mu-(1-\theta)}{(\beta-\mu\theta)})$	(Endemic) coexistence	$\beta > \mu + 1 - \theta$ $\vee \beta < \mu\theta$	-

the contrary, if $R_0 > 1$, the disease will spread in the predator population; in this case, the predators could either coexist or go extinct because the infection its too strong. To investigate the impact of pack hunting we study the bifurcation behavior, namely we numerically continue the equilibria and their stability as functions of the hunting cooperation parameter α. In Figure 3.2 are reported the results confronting two cases: when the disease cannot establish ($R_0 < 1$; left panels of Figure 3.2) and the endemic case ($R_0 > 1$; right panels of Figure 3.2).

Both panels show that the cooperation is fundamental for the survival of the predators. In fact, when the hunting pack is absent or small ($\alpha < \alpha_c$; Fig. 3.2C,D) the predators go extinct. As a consequence, the prey stabilize to the carrying capacity k. In this case the model is equivalent to the classical Lotka-Volterra model with prey self-regulation in a parameter range where the prey-only equilibrium (E_n or E_{ni}) is the only attractor. When α reaches the limit value $\alpha = \alpha_c$, there is a saddle–node bifurcation from which starts two branches of nontrivial equilibria, one being stable and the other one being unstable. Consequently for $\alpha > \alpha_c$ there is a bi-stability (the two red lines in Figure 3.2). Predators either go extinct (E_n or E_{ni}) or coexist with the prey (E_{np} or E_{npi}), depending on the initial population densities. In this range of parameters, when $\alpha > \alpha_c$ and hunting cooperation increases, the prey population density at stable coexistence equilibrium decreases

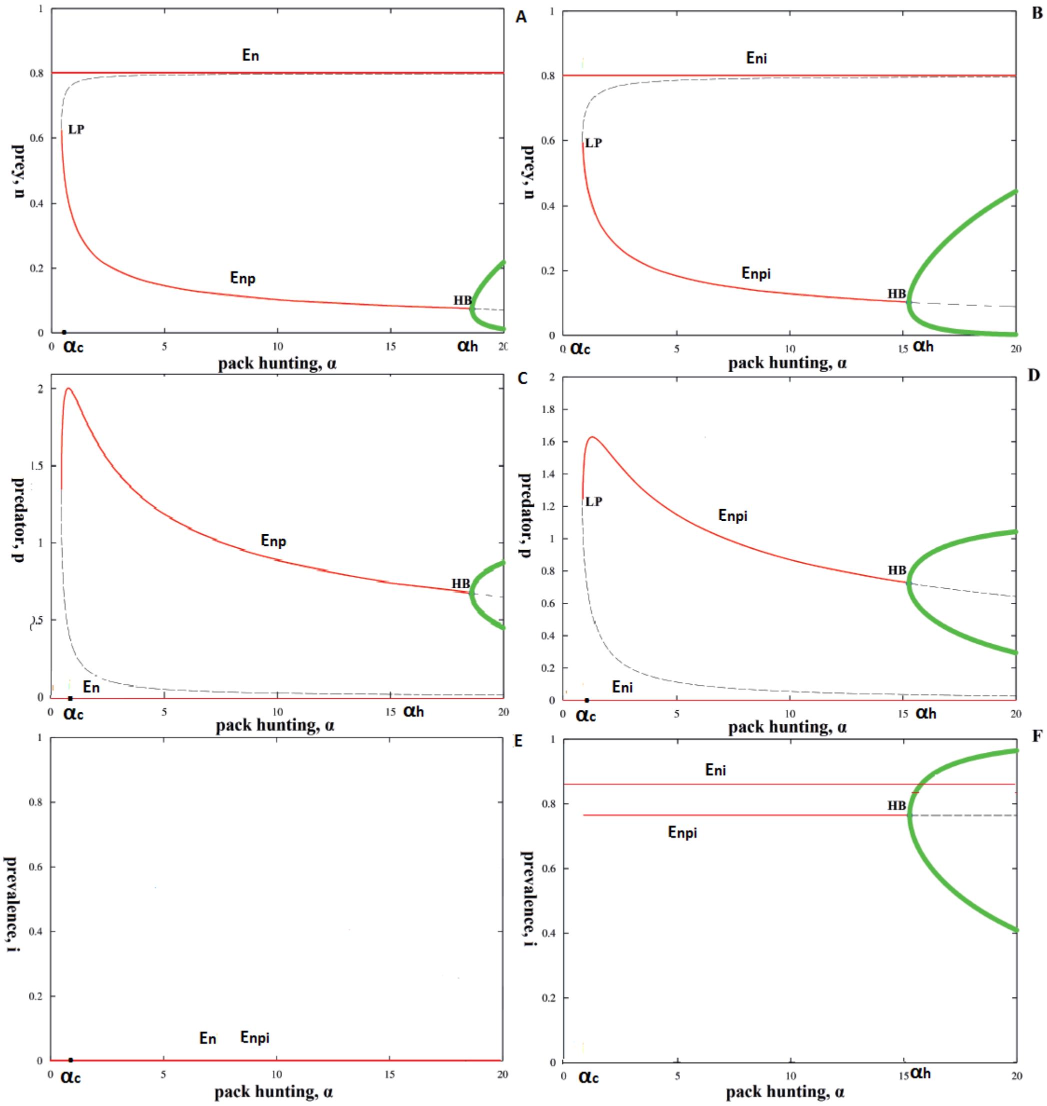

Figure 3.2: Bifurcation diagrams of model (3.1)–(3.3) for varying hunting cooperation. The left panels are the disease-free case ($\beta = 0.7; R_0 < 1$) and the right panels are the endemic case ($\beta = 5; R_0 > 1$). Red lines indicate stable equilibria and dashed black lines unstable equilibria. LP marks limit point bifurcations occurring at $\alpha = \alpha_c$ and HB marks Hopf bifurcations at $\alpha = \alpha_h$. The bold green lines are the amplitudes of limit cycles. Other parameter values: $r = 10$, $k = 0.8$, $\theta = 0.1$, $m = 0.3$.

because cooperating predators become more effective in exploiting the prey. In turn, predator density increases initially with increasing cooperation, but declines for larger values of α when the prey becomes overexploited.

Furthermore, for high values of predator cooperation, there is a Hopf bifurcation, where the coexistence equilibrium becomes unstable and populations start to oscillate (at $\alpha = \alpha_h$ in the bifurcation diagrams). Meanwhile the prey-only equilibrium remains stable, i.e. we continue to have bi-stability.

The two panels apparently seem showing the same behavior, however there are some important differences that underline the impact of the disease on the population dynamics.

First, the disease tends to reduce the impact of hunting cooperation. In fact, comparing the bifurcation diagrams of predators and prey, we observe that the limit point occurs for larger values of α in the presence of the disease. This makes sense as due to infection there is a higher mortality rate in the predator population. This requires higher hunting cooperation to mediate predator survival, and it also reduces the peak density of predators (compare Fig. 3.2D with 3.2C).

Analyzing the prevalence diagrams, we observe that, when $R_0 < 1$, the infection prevalence always vanishes, as we expect (Fig. 3.2E). By contrast, when the disease is established, the prevalence can reach two different levels, depending on whether or not predators survive. Since the spread of the disease is assumed not be influenced by the cooperation, the prevalence levels at the equilibrium are independent of α (Fig. 3.2F and Tab. 3.1).

It is interesting notice that, even if the predators population die out, the steady state E_{ni} is stable. This point is feasible from a mathematical point of view, because the prevalence is the ratio of predators infected ($i = \frac{SI}{P}$) in the limit process of the predator population density approaching zero. Therefore, when $P \to 0$ consequently S and I approach zero too. Thus in the limit scenario we have a $\frac{0}{0}$ situation. Depending on the dynamics of the population, it could be that the limit of the prevalence is different from zero, making the steady state E_{ni} feasible.

Moreover the infection transmission is frequency dependent, therefore it is constant in time, even when the population of predators approaches zero.

In reality the points E_{ni} and E_n represent the same stationary state, but their biological meaning are different. In the first case the predators die out because the infection is too strong: it represents the disease-induced extinction point. While E_n represents the trivial extinction and it depends only on ecological reasons, i.e. the prey cannot sustain the predator population.

From these analysis emerges that pack hunting can thus mediate the survival of predators even when the prey density cannot sustain predators in the absence of hunting cooperation. This is a new property not present in the classical Lotka–Volterra model and it represents the strong Alee effect induced in the predator population.

The Alee threshold is the predator density below which predator populations go extinct, and above which they survive. In this eco-system depends both on the value of the prey density to sustain the predator and on the number of the prevalence of infection.

In particular, the presence of the disease, increases the Allee threshold. Meaning that the size of predators has to be bigger than the disease-free case, to contrast the additional mortality. In this case we talk about *epidemiological Allee threshold.*

The unstable coexistence state, represented in panels C,D of Figure 3.2, gives an idea of the boundary points between the two basins of attraction. However, because we are dealing with a higher dimensional system, it does not correspond to the Allee threshold. Instead, we have to find the separatrix between the prey-only state and the coexistence state. From these analysis and the results presented in [58], we conclude that the two most important forces driving the population dynamics are pack hunting and the disease infection working in contrast in the survival of predator population.

In order to provide a more complete overview of these two features, we show a two parameter bifurcation diagram in the (α, β) plane reported in Figure 3.3 (see also [58]). We can distinguish four different dynamical regimes:

1. For low values of β ($R_0 < 1$) the infection is not endemic and there are three different scenarios depending on the level of hunting cooperation. First, for small values of α ($\alpha < \alpha_c$), the pack hunting is too inconsistent to overcome the predator extinction. The result is basically corresponding to a simple Lotka–Volterra model with prey self-regulation. Second, for higher hunting cooperation, there is a bi-stability induced by the cooperation, between the prey-only state E_n and the predator–prey coexistence state E_{np}. Third, for

even higher values of hunting cooperation, E_{np} becomes unstable. There is bi-stability between the prey-only state and the predator–prey oscillations. The following regimes assume disease persistence ($R_0 > 1$) but are analog to the cases just described.

2. For low values of α (to the left of the limit point curve), hunting cooperation is too weak to contrast the effect of the disease and to sustain the population. Therefore the only possible stable state is predators extinction E_{ni}.

3. The third scenario occurs for the widest range of the parameters α and β. It represents the bi-stability connected to the Allee threshold. Depending on the initial conditions the three population can coexist E_{npi}, otherwise the predators die out because of the infectious disease E_{ni}.

4. For large values of α a periodic behavior erases. On the right of the Hopf bifurcation curve, the endemic coexistence is cyclic. The system remains bistable, with the other attractor being E_{ni}.

For our goal, we are particularly interested in the bi-stable regime, where the system shows tipping behavior in the sense that predators either go extinct or survive at stable equilibrium. We shall focus on the endemic case and therefore consider the dynamical regime no. 3, which covers a large part of the parameter range shown in Fig. 3.3. However, the analysis so far has not given us any information about the Allee threshold. Therefore, we do not know anything about the critical extinction threshold for the predators. Is it very high such that predators would have a hard time to survive in the bistable case, or is the Allee threshold quite low such that survival chances in the bistable case would be much better? With this is mind we proceed in studying the basins of attraction and in particular the surface that allows to separate them in the phase space.

3.3 Separatrix Reconstruction

Before to reconstruct the separatrix surface, it is always advantageous to integrate and to represent some solutions of the system, in order to individuate the cubic domain to apply the bisection method.

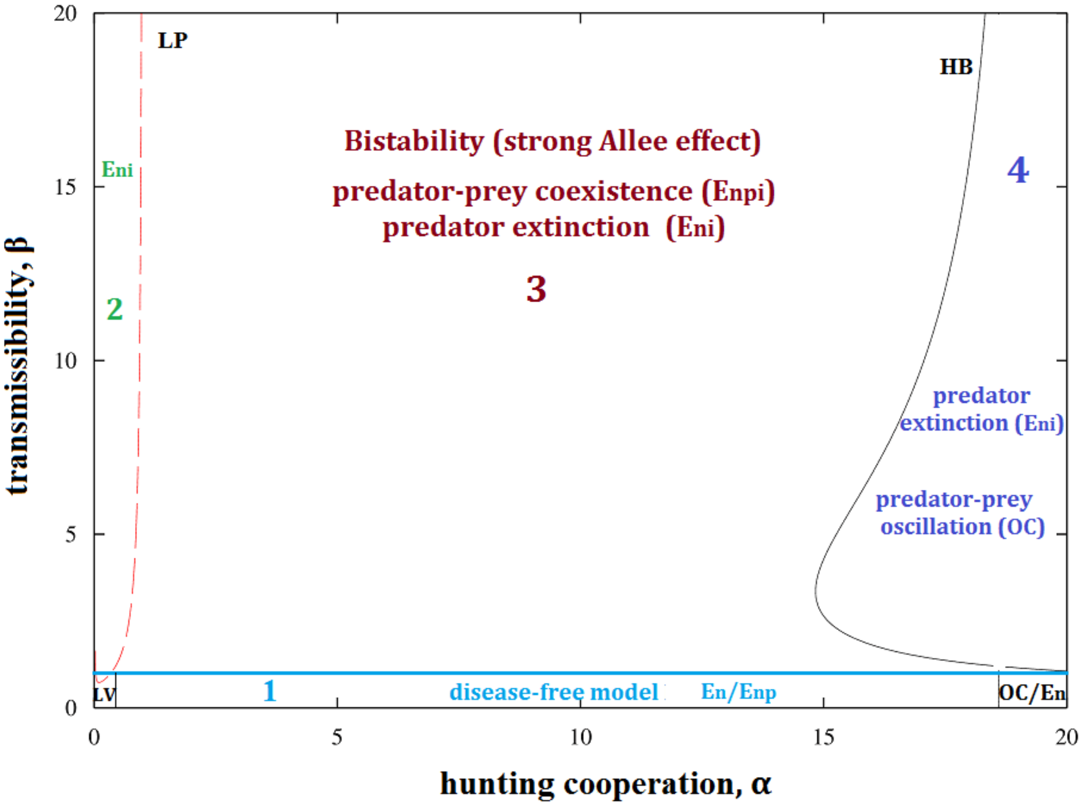

Figure 3.3: Two-parameter bifurcation diagram of model (3.1)–(3.3) when varying predator cooperation α and disease transmissibility β. The red dashed line represents the limit point bifurcation curve (LP) and the black one the Hopf bifurcation curve (HB). There are four different scenarios in the endemic case: (1) Disease-free model, (2) Extinction of predators, (3) Bistability between predator extinction and stable endemic coexistence, and 4) Bistability between predator extinction of oscillatory endemic coexistence (OC). In the disease-free case, LV stands for the prey-only state of the Lotka–Volterra model with logistic prey growth.Other parameter values as in Fig. 3.2.

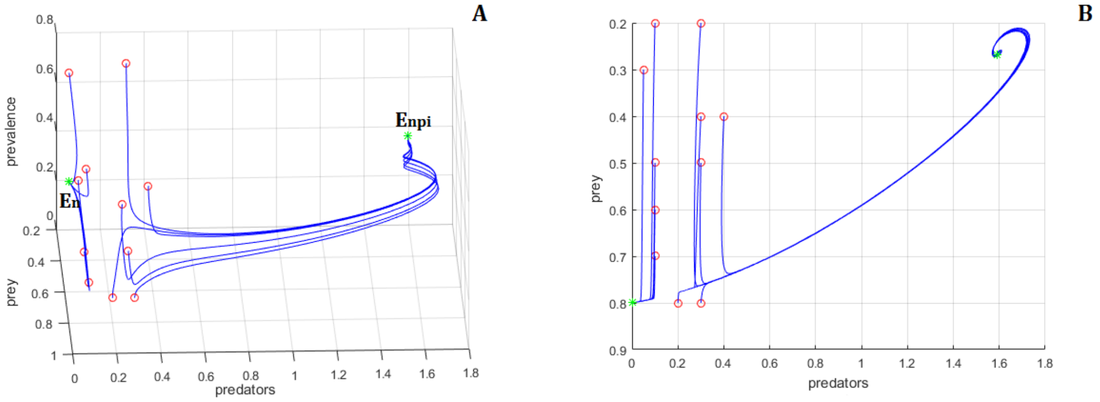

Figure 3.4: Example of trajectories of model (3.1)–(3.3) starting from different initial conditions represented by the red empty circles and approaching equilibrium points (green stars) in 3D phase space (A) and projected on the phase plane (n, p) (B). Parameter values: $\alpha = 2$, $\beta = 2$, and the other ones as in Fig. 3.2.

Fixing the biological parameters, in Figure 3.4 we show different trajectories starting from several initial conditions (red circles). In this case the populations can reach one of the two different stable equilibria (green stars).
Looking at the diagram and considering the bifurcation analysis conducted, we already get an idea about the location of the separatrix points.

In particular, by visualizing the projection on the plane (p, n) (Fig. 3.4B), we note that the possible future outcomes of the system depend mainly on the initial predator densities. This is due to the strong Allee effect in predators, linked with the bi-stability. The separatrix represents the Allee threshold separating the domains of attraction of the predator extinction E_{ni} and coexistence point E_{npi}.
From these observations we can state that the separatrix surface is located between the planes: $\pi_1 : p = 0$ and $\pi_2 : p = l$. Hence, the set of the initial conditions reduces to

$$(n_j, 0, i_k), \quad (n_j, l, i_k), \quad j, k = 1, ..., N. \tag{3.5}$$

Therefore, we solve the model (3.1)–(3.3) on the cubic domain $[0, 1]^3$ by considering $N = 10$ equispaced points on both n-axis and the i-axis. The Figure 3.5A shows the separatrix points detected iterating the bisection method to the 100 pairs of initial conditions, until the tolerance 10^{-4} is obtained.

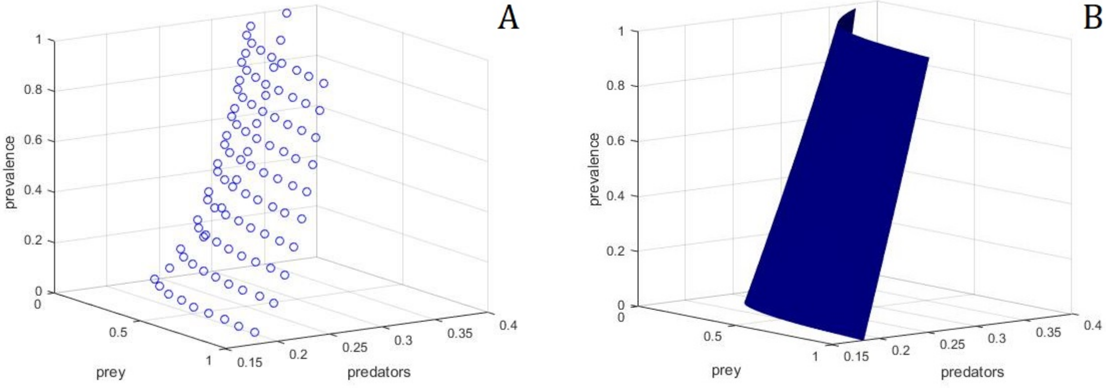

Figure 3.5: (A)Scattered separatrix points detected with bisection method. (B) Reconstruction of the surface. Parameter values as in Fig. 3.4.

We choose the Wendland C2 compactly supported function, centered on $\mathbf{y}$

$$\omega(\mathbf{x}_i, \mathbf{y}) = (1 - \epsilon||\mathbf{y} - \mathbf{x}_i||_2)_+^4(4\epsilon||\mathbf{y} - \mathbf{x}_i||_2 + 1), \tag{3.6}$$

as weights. The goodness of the approximation depends on the size of the support. Therefore the approximation goodness is influenced by the shape parameter ϵ. From empirically simulations we have found that for our applications a good range for the parameter is $1 \leq \epsilon \leq 3$. The numerical test presented in this section are obtained considering $\epsilon = 3$ (Figure 3.5B).

The bifurcation analysis has showed as the two most important forces, driving the dynamics of the systems, are the disease and the cooperation between predators. To this aim, we reconstruct the separatrix surface by considering different values of α and β, in order to understand the impact on the Allee threshold of the pack hunting coupled with the infectious transmission.

As previous observed (Figure 3.4), the long term evolutions of the orbits mainly depends on predators densities and the Allee threshold decreases for larger values of prey. This seems plausible because with more resources, the predators do not need a strong cooperation to guarantee the survival.

However by fixing all the parameters and by varying only the parameter β, the separatrix manifold shifts to the right, reaching bigger values of predators densities. This is due to the stronger transmissibility generating more infected on predators population. Increasing the prevalence, the predators have to face with an additional mortality disease-induced, thus to contrast the extinction the initial density has to be larger than before. Therefore, the Allee thresholds tend to be larger, which is why the separatrix has shifted to the right-hand side (i.e., in the positive predator direction) in comparison to Figure 3.6A.

Opposite results are obtained by varying hunting cooperation, α (Fig. 3.7). If hunting cooperation increases, the separatrix surface moves closer to the plane $p = 0$, considerably reducing the basin of attraction of the prey-only state E_{ni} (compare Fig. 3.7B with Fig. 3.7A). Therefore, the trajectories of the system almost always tend to the coexistence state E_{npi} except for very low predator densities.

So far we have seen that disease transmissibility tends to increase the Allee threshold, whereas hunting cooperation tends to decrease the Allee threshold. If we increase the two parameters β and α simultaneously, we observe, for the parameter set chosen in Figure 3.7C, that the separatrix surface moves close to the plane $p = 0$. This means that the impact of pack hunting prevails even when disease transmission increases. The location of the Allee thresholds thus complement the results from a bifurcation analysis.

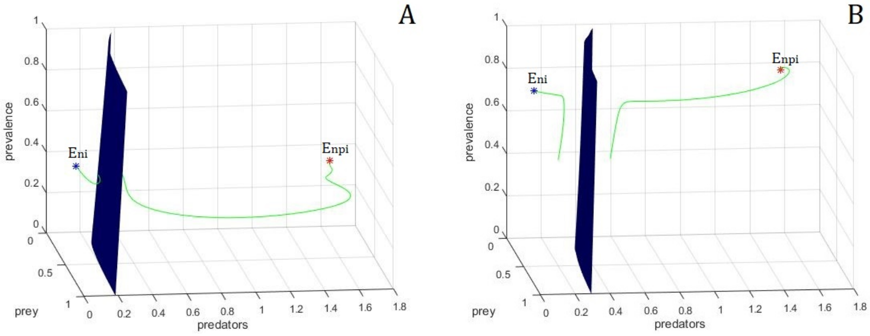

Figure 3.6: Separatrix curve for different values of β. (A) $\alpha = 2$, $\beta = 2$; (B) $\alpha = 2$, $\beta = 8$. The red star represents E_{npi} and the blue one is E_{ni}. Two trajectories, belonging to different basins are integrated and represented in green. Other parameter values as in Fig. 3.2.

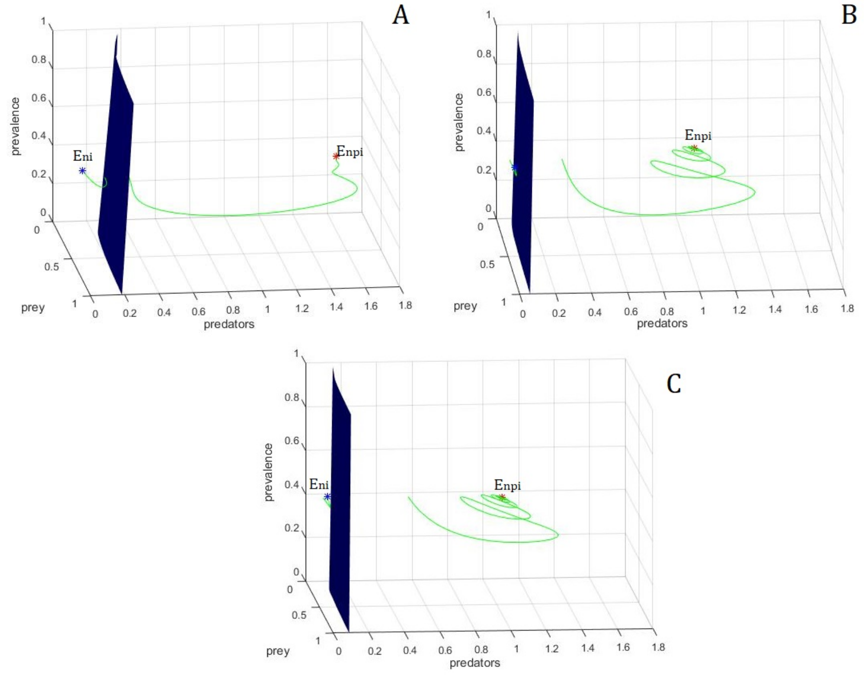

Figure 3.7: Separatrix curve for different values of α and β. (A) $\alpha = 2$; $\beta = 2$, (B) $\alpha = 6$; $\beta = 2$ (C) $\alpha = 6$, $\beta = 8$. The red star represents E_{npi} and the blue one is E_{ni}. Two trajectories, belonging to different basins are integrated and represented in green. Other parameter values as in Fig. 3.2.

Table 3.2 reports the execution times to detect and to reconstruct the separatrices for different values of the parameters α and β.

Separatrix	Detection Time	Reconstruction Time
$\alpha = 2$, $\beta = 2$	2.50 min	35 sec
$\alpha = 2$, $\beta = 8$	2.35 min	40 sec
$\alpha = 6$, $\beta = 2$	2.27 min	47 sec
$\alpha = 6$, $\beta = 8$	2.42 min	32 sec

Table 3.2: Execution times for the detection and the reconstruction of the separatrices by fixing different values of α and β.

3.4 Results Interpretations

In this chapter we have addressed about an important application of separatrix reconstruction in the study and the analysis of the Allee effect. The algorithm presented in the previous chapter is a fundamental tool to represent the basins of attraction and to understand the possible outcomes of the model. The algorithm makes use of a bisection method proposed in [22, 23, 24] to detect the scattered data points lying on the surfaces, that are reconnected employing a Moving Least Squares method.

Standard model analysis, such the equilibrium and stability study, as well as bifurcation and continuation methods, offers various insights and give important information about the research domain for the separatrix points. However they do not give any information about the Allee effect. In particular the bifurcation analysis presents bi-stability for a large range of parameter α, suggesting an induced strong Allee effect in predator population.

During the first analysis of this eco-epidemiological model, the authors already noticed that the populations almost always evolve toward the coexistence state when the parameter α is big. They observed this phenomenon through empirical experiments, i.e. integrating several trajectories from different initial conditions, even close to the extinction point. These results suggested that the basin of attraction of the point E_{ni} was very small. However it was not possible demonstrated it without the reconstruction of the separatrix.

Here we proved that, even if the mathematical analysis shows a bi-stability, i.e. a strong Allee effect, actually when the cooperation is really strong the Allee threshold is almost zero, in which case the predators almost always survive. In other terms, pack hunting can not only mediate predator survival by inducing a strong Allee effect, but it can be so powerful that it turns a strong Allee effect effectively into a weak Allee effect. The difference is that in the latter case predator survival is (almost always) guaranteed, whereas in the former case an initial number of predators above the Allee threshold is needed for survival. The numerical strategy allows us to underline the impact of the pack hunting and the disease transmission directly on the Allee threshold. This quantity is important in control programs to eradicate predators that are pests (e.g. in the case of biological invasions) or one may think to preserve an endangered predator population considering a sufficient number of re-introductions.

Chapter 4

Invariant Manifolds Reconstruction

In the previous chapter we have presented the bisection method. This routine represents a valid and easy to implement algorithm to detect the separatrix points of dynamical models.

However a controversial aspect is the high computational cost. In fact, for each iteration, it is required the integration of the trajectory of the new initial state until the desired accuracy is obtained. Moreover this procedure is applicable only for dynamical systems admitting equilibria that are fixed points. In order to deal with these problems, we consider the vector field properties of dynamical systems. Recently, to visualize and to study the phase-space, many topological methods have been developed. The principal aim is the representation of the topological skeleton, i.e. the vector field analysis, considering only the fixed state and the separatrices of the basins of attraction. Many studies have been conducted to analyze the planar topological skeletons [9, 57, 107, 108, 110]. While only few approaches exist to apply them to three dimensional vector field [45, 89, 106]. In fact, in the former case the integration of the separatrix orbits is less stable and the visualization of these manifolds is difficult to be treated. Therefore the existing methods either are focused only on stable analysis, ignoring the separatrix, or consider simple flow dynamics.

Here we present a new detection procedure to deal with three dimensional vector field. It is based on a particular class of equilibrium, the saddle points, and their invariant manifolds.

4.1 Vector Field Topology

Before to describe the new detection method, we recall some important properties of the vector field topology, that are fundamental to deal with the new algorithm. In Section 1.6 we briefly introduced the stability analysis. In particular, we said that, given a fixed point $\mathbf{x}_0$ for the model

$$\dot{\mathbf{x}} = f(\mathbf{x}), \quad \mathbf{x} \in M \subseteq \mathbb{R}^n, \tag{4.1}$$

if the Jacobian matrix $\mathbf{A}(\mathbf{x}_0)$ has all eigenvalues with negative real part, then it is stable. On the contrary, a critical point is called unstable node when all the eigenvalues have positive real part. We did not consider the eigenvalues with real part with opposite sign. In this case the point is unstable but it is called *saddle*. Therefore, assuming that the model (4.1) is a three dimensional system and that all the eigenvalues are real, the following classification holds:

Stable Node	$\mathrm{Re}(\lambda_1) \leq \mathrm{Re}(\lambda_2) \leq \mathrm{Re}(\lambda_3) < 0$
Unstable Node	$0 < \mathrm{Re}(\lambda_1) \leq \mathrm{Re}(\lambda_2) \leq \mathrm{Re}(\lambda_3)$
Repelling Saddle	$\mathrm{Re}(\lambda_1) < 0 < \mathrm{Re}(\lambda_2) \leq \mathrm{Re}(\lambda_3)$
Attracting Saddle	$\mathrm{Re}(\lambda_1) \leq \mathrm{Re}(\lambda_2) < 0 < \mathrm{Re}(\lambda_3)$

Each of these classes can be further divided, if the Jacobian matrix $A(\mathbf{x}_0)$ admits two complex conjugate eigenvalues. In this case the trajectories of the system spiral around the critical point and the equilibrium could be:

Stable Node–Focus	$\mathrm{Re}(\lambda_1) < \mathrm{Re}(\lambda_2) = \mathrm{Re}(\lambda_3) < 0$ $\mathrm{Im}(\lambda_2)$=-$\mathrm{Im}(\lambda_3)$
Unstable Node–Focus	$0 < \mathrm{Re}(\lambda_1) < \mathrm{Re}(\lambda_2) = \mathrm{Re}(\lambda_3)$ $\mathrm{Im}(\lambda_2)$=-$\mathrm{Im}(\lambda_3)$
Repelling Saddle–Focus	$\mathrm{Re}(\lambda_1) < 0 < \mathrm{Re}(\lambda_2) = \mathrm{Re}(\lambda_3)$ $\mathrm{Im}(\lambda_2)$=-$\mathrm{Im}(\lambda_3)$
Attracting Saddle–Focus	$\mathrm{Re}(\lambda_1) = \mathrm{Re}(\lambda_2) < 0 < \mathrm{Re}(\lambda_3)$ $\mathrm{Im}(\lambda_1)$=-$\mathrm{Im}(\lambda_2)$

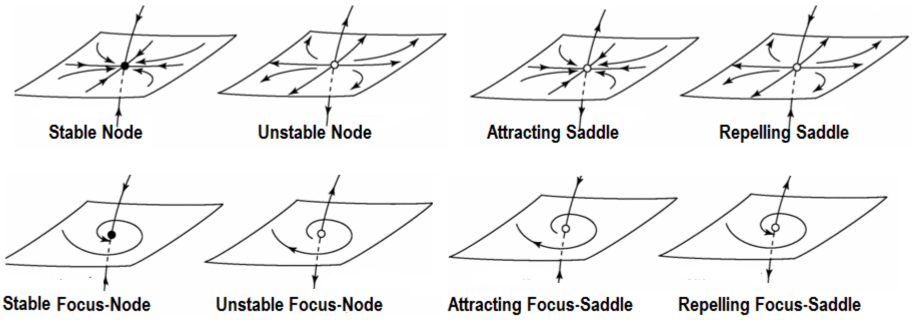

Figure 4.1: Example of Equilibria in a three dimensional space.

In this classification we exclude the non hyperbolic equilibria because they are not important for the topic of this thesis. A detailed discussion of the theory of equilibrium points can be retrieved in [85].
Instead, for our goal, we are focused on the saddle points. In fact, the separatrices are curves or surfaces separating regions of the vector field with different flow behavior. Around the stable or the unstable node, all the trajectories have the same direction, namely incoming or outgoing respectively. On the contrary, around the saddle points we observe an inflow or outflow behavior, depending on the signs of the eigenvalues. For example, a *repelling saddle* has a one direction of inflow behavior and a plane where a $2D$ outflow behavior occurs (Figure 4.1). These subspaces depend on the eigenvectors of the points and they are the key to detect the invariant manifolds of the saddle.

Definition 3.
A subset $W \subseteq \mathbb{R}^n$ *is called* ***k-manifold****, if it is locally homeomorphic to a k-dimensional affine subspace of* $\mathbb{R}^n$*.*

The definition of a manifold is more general, but this will serve our goal. These particular surfaces have well defined tangent spaces at each point that are independent on the representation of the manifolds.

Definition 4.
A k-manifold $W \subseteq \mathbb{R}^n$ *is said to be* ***invariant*** *under the flow of a vector field if:*

$$\boldsymbol{x} \in W \Rightarrow \Phi^t(\boldsymbol{x}) \in W \quad \textit{for small} \quad t \geq 0 \tag{4.2}$$

where $\Phi^t(\boldsymbol{x})$ *is the flow of* f*.*

This definition is equivalent to state that f is tangent to the manifold W, therefore an invariant manifold is a union of integral trajectories of the vector field. When the system (4.1) is linear with a fixed point at the origin $\mathbf{x}_0$, the real eigenspaces E^s and E^u of $A(\mathbf{x}_0)$, represent respectively the stable and unstable subspaces and they are invariant under the flow $\dot{\mathbf{x}} = A\mathbf{x}$.
In particular E^s and E^u are generated by the eigenvectors associated to the eigenvalues lying on the open left half plane and the open right half plane, respectively. When the system is not linear, these subspaces are provided by the linearization of the model: $A = Df(\mathbf{x}_0)$ and in a neighborhood of the fixed point, they are tangent to the invariant manifolds [95].

Theorem 2 (Local invariant Manifold Theorem for Hyperbolic Points)**.**
Let be f *a smooth vector field on* $\mathbb{R}^n$ *and* $\boldsymbol{x}_e$ *an hyperbolic equilibrium point. There is a* $k-$*manifold* $W^s(\boldsymbol{x}_e)$ *and a* $n-k$ *manifold* $W^u(\boldsymbol{x}_e)$ *each containing the point* $\boldsymbol{x}_e$ *such that the following holds:*

1. *Each of* $W^s(\boldsymbol{x}_e)$ *and* $W^u(\boldsymbol{x}_e)$ *is locally invariant under* f *and contains* $\boldsymbol{x}_e$*.*
2. *The tangent space to* $W^s(\boldsymbol{x}_e)$ *at* $\boldsymbol{x}_e$ *is* E^s *and the tangent space to* $W^u(\boldsymbol{x}_e)$ *at* $\boldsymbol{x}_e$ *is* E^u*.*
3. *if* $\boldsymbol{x} \in W^s(\boldsymbol{x}_e)$ *then the integral curve with initial condition* $\boldsymbol{x}$ *tends to* $\boldsymbol{x}_e$ *as* $t \to \infty$ *and if* $\boldsymbol{x} \in W^u(\boldsymbol{x}_e)$ *then the integral curve with initial condition* $\boldsymbol{x}$ *tends to* $\boldsymbol{x}_e$ *as* $t \to -\infty$*.*
4. *The manifold* $W^s(\boldsymbol{x}_e)$ *and* $W^u(\boldsymbol{x}_e)$ *are locally uniquely, they are determined by the preceding conditions.*

Considering these vector field features, we will present a detection strategy to represent the separatrix manifolds.

4.2 Detection of the invariant manifolds

Since in two dimension the problem of the separatrix manifold is fully addressed, in the following we consider only three dimensional systems.

Therefore the saddle node has a one dimensional invariant manifold consisting in a trajectory passing through the point itself and a bi-dimensional manifold tangent to the invariant plane E^s or E^u. We start our discussion, focusing on this latter.

The first step consists in computing the Jacobian matrix $\mathbf{A}(\mathbf{x}_0)$ and analyzing the associated eigenvalues λ_i with the respective eigenvectors $\mathbf{v}_i$, $i = 1, 2, 3$. If the saddle point is repelling, there are two eigenvalues with positive real part. Therefore, for Theorem 2, the corresponding eigenvectors generate an invariant plane that is tangent to the unstable manifold $W^u(\mathbf{x}_0)$. While, if the saddle point is attracting, the eigenvectors $\mathbf{v}_1$ and $\mathbf{v}_2$ generate an invariant plane that is tangent to the stable manifold $W^s(\mathbf{x}_0)$.

When the saddle is a focus we have a particular case and the tangent plane is generated by two complex conjugated eigenvectors such that

$$Re(\mathbf{v}_1) = Re(\mathbf{v}_2) \text{ and } \quad Im(\mathbf{v}_1) = -Im(\mathbf{v}_2).$$

Therefore, we consider as first generating vector the real part and as second the imaginary part (Step 2.1).

Now, to integrate the scattered data on the invariant manifold, we place N points on an ellipse centered at the saddle whose semi-axes are the corresponding eigenvectors. Because the subspace is invariant, by starting from these points, all their trajectories belong to the manifold itself. Therefore we numerically integrate with fourth order Runge-Kutta method, forward in time for repelling saddle and backward in time for the attracting one (Step 3-4).

Finally, all the trajectories are discretized in order to obtain all the scatter data on the separatrix. Indeed we identify the states obtained for each integration step (Figure 4.2A). If a higher number of separatrix points is required the eigenvectors could be rescaled in order to obtain a bigger ellipse. Then the procedure is repeated for the new ellipse points (Figure 4.2B).

Similar idea is applied to find the one dimensional manifold. In this case we integrate the flow starting from the point: $\mathbf{x}_0 + \mathbf{v}_3$, where $\mathbf{x}_0$ is the saddle point and $\mathbf{v}_3$ is the third eigenvector (Figure 4.3).

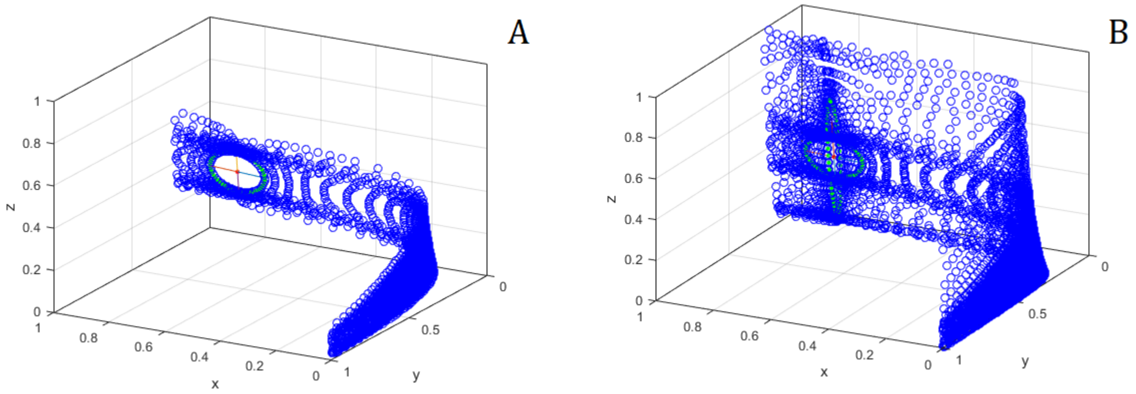

Figure 4.2: Detection of the separatrix points. The green points lying on the ellipses are the initial conditions for the backward integration. The blue points are the discrete values of the trajectories. In figure A only one set of seeding points is considered. In Figure B are taken up two sets.

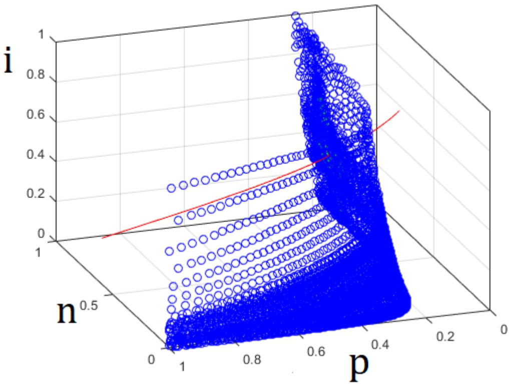

Figure 4.3: Scattered data lying on the bi-dimensional manifold (blue points) and the invariant curve in red.

When the system admits three or more equilibria the reconstruction of more separatrix surfaces is required. Therefore the detection procedure is applied to each saddle points (Step 5).

For the sake of clarity we illustrate the fundamental steps of computational process developed:

- - $\mathbf{s} \in \mathbb{R}^{n\times 3}$: matrix whose rows contain the saddles of the model.
- - **parameter** $\in \mathbb{R}^{1\times k}$: the parameters vector.
- - $\mathbf{l} \in \mathbb{R}$: the edge length of the cubic domain considered.
- - $\mathbf{t} \in \mathbb{R}$: size of integration interval.
- - $\mathbf{M} \in \mathbb{R}$: number of the seeding points on the ellipse.
- - ***String***: string with the name of the 3D model considered.

- **STEP 1** Consider one saddle point $\mathbf{x}_0 \in E^3$ and calculate the Jacobian matrix $J(\mathbf{x}_0)$.
- **STEP 2** Calculate and order the eigenvectors and eigenvalues in ascending order:
  $V = [\mathbf{v}_1; \mathbf{v}_2; \mathbf{v}_3]$ such that $Re(\lambda_1) < Re(\lambda_2) < Re(\lambda_3)$
  STEP 2.1 ***if*** $\mathbf{v}_1$ and $\mathbf{v}_2$ are complex conjugated

  $$\textbf{\textit{then}}\ \mathbf{v}_1 = Re(\mathbf{v}_1) \wedge \mathbf{v}_2 = Im(\mathbf{v}_1)$$

- **STEP 3** ***for*** $i = 0 : M$
  STEP 3.1 Consider the i-th point on the ellipse:

  $$\mathbf{x} = i * pi/M;\ \mathbf{y} = (1 - cos(\mathbf{x}))/2 * pi;$$
  $$\mathbf{v} = cos(x) * \mathbf{v}_2 + sin(y) * \mathbf{v}_1;$$

  STEP 3.2 Define the initial condition : $\mathbf{z} = \mathbf{x}_0 + \mathbf{v}$.

STEP 3.3 Integrate the system in the interval $[0, t]$.

```
if $\lambda_1 < 0 \wedge \lambda_2 < 0$ then $t = -t$
    $[t, u] = ode45(@system, [0, t], parameter, z)$
```

- **STEP 4** Plot the scattered data on the phase-plane:
  scatter3(u(:,1),u(:,2),u(:,3));
- **STEP 5** Repeat the procedure for each saddle point.

4.3 Refinement of the scattered points

In previous section, we observe that integrating the seeding points, every trajectory obtained is composed by a scattered separatrix point for each integration step. This step could be reduced, being very small, when a better accuracy is required. As result, many points could be overlapped, generating unnecessary information for the reconstruction.

To improve the algorithm and to reduce the computational effort, we follow the idea presented in [23], to refine the set of tipping points detected.

First of all, depending on the parameters and the problem analyzed, we have to consider the range for the variables involved. Once the domain of interest is individuated, the integration of the trajectories is forced to stop when they go outside the limit boundaries.

Then, the N points detected are collected in a matrix S of dimension $N \times 3$ and the values:

$$\begin{aligned} x_{min} &= min\left(S(1,:)\right); \quad x_{max} = max\left(S(1,:)\right) \\ y_{min} &= min\left(S(2,:)\right); \quad y_{max} = max\left(S(2,:)\right), \end{aligned} \tag{4.3}$$

are computed. The intervals $[x_{min}, x_{max}]$ and $[y_{min}, y_{max}]$ are divided into P and Q sub-intervals, respectively. The result is a grid of $P \times Q$ points on a plane parallel to $z = 0$. For each interval I_{PQ}, the average is computed by considering the separatrix points belonging to it.

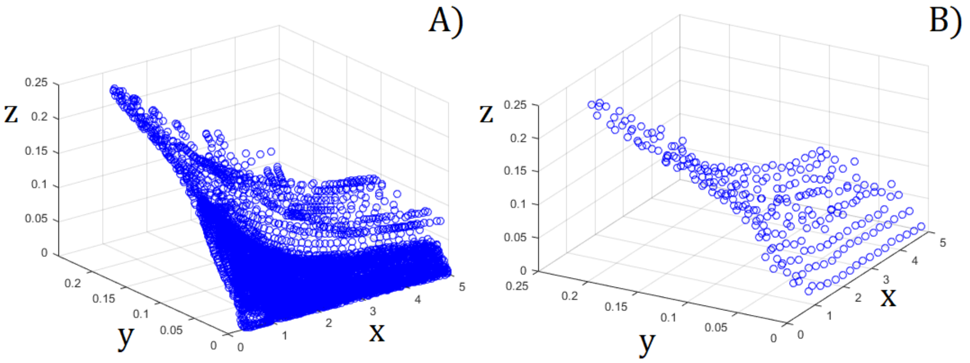

Figure 4.4: A) Separatrix Points obtained with the detection strategies. B) Separatrix points refined.

This refinement provides a new matrix C_1 with the following entries

$$C_1(i,:) = \sum_{i \in I_{PQ}} \frac{S(i,:)}{k_{PQ}}$$

where k_{PQ} is the cardinality of the sub-interval taken into account. Of course if an interval does not contain any points it is not considered.

When the separatrix presents particular geometry, it is necessary re-iterate the same process, but considering the grid on different planes. For example, when the manifold is represented by a plane parallel to $y = 0$ or to $z = 0$, the strategy proposed does not provide a good refinement. For this reason it is necessary to consider the other axis

$$z_{min} = min\left(S(3,:)\right), \quad z_{max} = max\left(S(3,:)\right),$$

and the interval $[z_{min}, z_{max}]$ is divided into M sub-intervals. Two matrices are obtained

$$\begin{aligned} C_2(i,:) &= \sum_{i \in I_{QM}} \frac{S(i,:)}{k_{QM}}, \\ C_3(i,:) &= \sum_{i \in I_{PM}} \frac{S(i,:)}{k_{PM}}. \end{aligned} \tag{4.4}$$

Finally, all the refinement points of the different matrices are collected in one set. Of course, depending on the separatrix surface, one chooses the opportune matrix. In Figure 4.4 we show the new set of points considering only C_1.

4.4 Bio-mathematical Applications

To validate the new method we will present three case studies, reconstructing the separatrix of particular eco-epidemiological predator-prey models.
To start we consider again the model of Section 3.2 to confront the results obtained:

$$\begin{aligned}
\frac{dn}{dt} &= r\left(1-\frac{n}{k}\right)n-(1+\alpha p)\,np,\\
\frac{dp}{dt} &= -(1+\mu i)\,p+(1+\alpha p)\,np,\\
\frac{di}{dt} &= i\,(1-i)\,(\beta-\mu)-(1+\alpha p)\,(1-\theta)\,ni,
\end{aligned}$$

We fix the parameter value to: $r=10$, $k=0.8$, $\theta=0.1$, $\mu=0.3$, $\alpha=1.5$, $\beta=2$, for which the system admits the following equilibria:

$E_{np}\approx(0.8,0,0.4061)$	Stable node
$E_{npi}\approx(0.3156,1.703,0.4061)$	Stable node
$E_0\approx(0,0,0)$	Unstable node
$E_n\approx(0.8,0,0)$	Unstable node
$E_i\approx(0,0,1)$	Unstable node
$E_s\approx(0.7632,0.3128,0.4061)$	Attracting Saddle

The Jacobian matrix of the system $A(E_s)$ has two stable eigenvectors: $\mathbf{v}_1=(0.9975;0.0450;0.0551)$, $\mathbf{v}_2=(0.0218;0.1387;0.9901)$. On the bi-dimensional invariant stable subspace E^s, we take the ellipse whose semi-axes are $\mathbf{v}_1$ and $\mathbf{v}_2$ rescaled of a factor 0.02. We integrate the separatrix surface starting from $N=15$ points. To increment the number of points we integrate the trajectories of other $N_1=15$ points on a bigger ellipse, this time rescaling the eigenvectors of a factor 0.1. Once that a sufficient separatrix points are obtained, we apply a refinement to avoid the unnecessary information. Because the surface is almost parallel to plane $p=0$ and approaches the prey null-plane, we have to consider the two sets

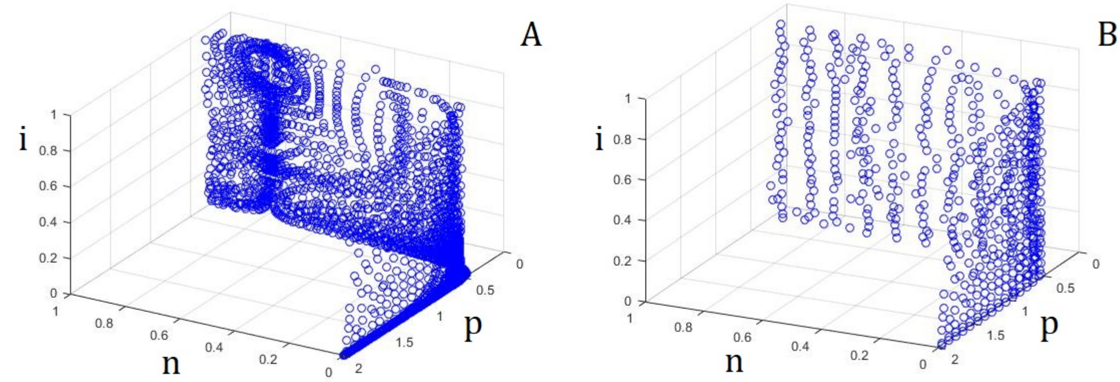

Figure 4.5: A) The blu circles are the points obtained by backward integration. B) The refinement points by considering $M = 30$, $P = Q = 10$, sub-intervals. The parameters values for the model are: $r = 10$, $k = 0.8$, $\theta = 0.1$, $\mu = 0.3$, $\alpha = 4$, $\beta = 4$.

of points: C_2 and C_3 presented in previous section. In Figure 4.6 we show all the points found with backward integration and on right picture the refinement considering $M = 30$, $P = Q = 10$ sub-intervals on x,y,z-axis, respectively.

Now, we can reconstruct the surface with the Moving Least Squares approximant. As before, we use the Wendland $C2$ compactly supported function centered at the evaluation point $\mathbf{y}$ as weighted function, considering $\epsilon = 2$ and 70 evaluation points (Figure 4.6).

The surface continues approaching the plane $n = 0$. This indicates that the separatrix manifold bends toward higher values of predators when the prey population becomes small. Of course, since in this model it is not assumed an external foraging, by considerably reducing the prey population, the predators have no sufficient resources to sustain themselves, no matter how strong they cooperate in hunting. In Figure 4.7 we confront the different detection methods: the red points are found with the bisection procedure, while the blue ones are detected employing the new strategy. The points obtained are quite the same, showing the validity of both methods.

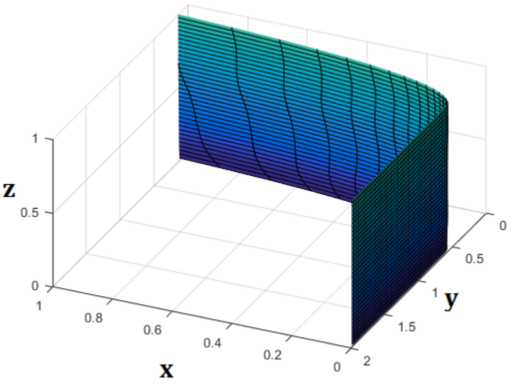

Figure 4.6: Reconstruction of the separatrix using the MLS method, by fixing $r = 10$, $k = 0.8$, $\theta = 0.1$, $\mu = 0.3$, $\alpha = 4$, $\beta = 4$.

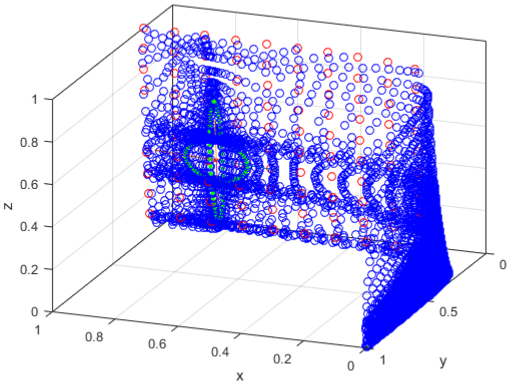

Figure 4.7: Confront between the two different detection method for separatrix surface for the model (3.1)–(3.3). The red dots represent the point found with the bisection procedure, while the blue ones are depicted by employing the new strategy. Parameters: $r = 10$, $k = 0.8$, $\theta = 0.1$, $\mu = 0.3$, $\alpha = 2$, $\beta = 2$.

4.5 Multi-stability and complex attractors

Until now we have considered only bi-stable systems, with the reconstruction of only one separatrix surface.

We will show as this procedure works with multi-stable models with any number of contemporary stable steady state. In fact, it depends only on the saddle points and their manifolds.

Moreover, to complete the analysis we will show the reconstruction of a separatrix manifold when the stable equilibrium is a periodic attractor.

4.5.1 Tri-stable eco-epidemiological model

In this section we present a model analyzed in [62]. Also in this study, the authors have the goal to understand how the presence of the Allee effect with the spread of a disease, influences the population dynamics in a prey-predator ecosystem. The a-dimensional model considered is:

$$\begin{aligned}
\frac{dS}{dt} &= S\left[r(S-\theta)(1-S-I)-\beta I-aP\right], && (4.5)\\
\frac{dI}{dt} &= \beta SI-aIP-\mu I, && (4.6)\\
\frac{dP}{dt} &= P\left[bS+\alpha I-d\right] && (4.7)
\end{aligned}$$

where the prey density is split into susceptible (S) and infected (I) population and P represents the predator density. In this model the Allee effect is not induced as in the previous example, but is a dynamical feature already modeled by the term:

$$r\left(S-\theta\right)\left(1-S-I\right), \tag{4.8}$$

where θ is the Allee threshold and r is the maximum birth rate of species. In this case, if the initial conditions of susceptible are below θ the populations die out, otherwise converges to 1.

The disease spreads only in horizontal way and we report only the frequency-dependent transmission, where β is the transmissibility. The predation is modeled by the Holling Type I function: aIP, where a is the attack rate of predators. The

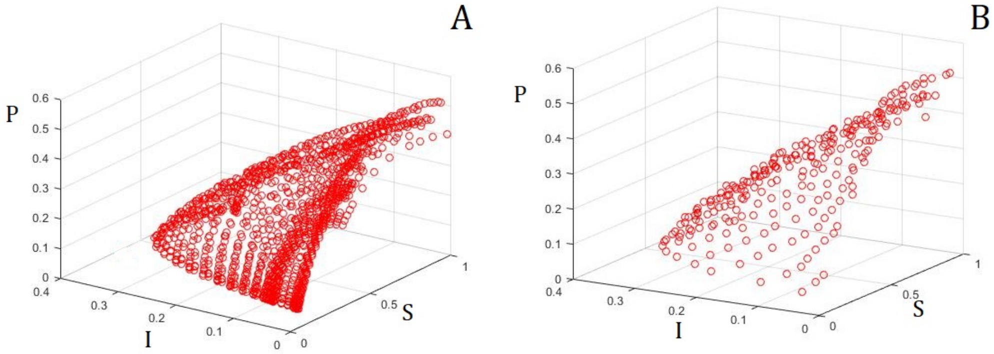

Figure 4.8: A) Scattered data on invariant manifold of saddle E_{s_1} for the model (4.5)–(4.7); B) Refinement of the scattered data considering $P = Q = M = 10$ sub-intervals.

parameters b and α represent the total effect to predator by consuming susceptible and infected prey, respectively. Finally the predators die with a natural death rate m and the infected suffer of an additional disease-induced death rate μ.

The authors, through the model analysis and integrating some initial conditions on the phase space, give some general information about the basins of attraction. However here we employ our method to obtain a more accurate representation of the phase space reconstructing the different domains [35].

Letting $\beta = 1.5$, $\theta = 0.2$, $a = 2$, $b = 1.35$, $\mu = 1$ and $d = 1$ the system admits three stable equilibria: the origin $E_0 \equiv (0, 0, 0)$, the disappearance of the disease $E_1 \approx (0.7407, 0, 0.0701)$ and the predator extinction $E_2 \approx (0.6667, 0.0791, 0)$.

For the reconstruction of their basins of attraction we consider the invariant manifolds of the attractive saddle points $E_{s_1} \equiv (\theta, 0, 0)$ and $E_{s_2} \approx (0.7329, 0.0211, 0.0497)$. We integrate the first separatrix considering $M = 30$ equispaced points on two ellipses generated by the two eigenvectors of the saddle E_{s_1}, namely $\mathbf{v}_1 \approx (0.4099, 0, 0.9121)$ and $\mathbf{v}_2 \approx (0.329, 0.9442, 0)$ rescaled of a factor 0.04 and 0.1, respectively. Then, through a backward integration we obtain all the scattered data on the manifold, that are refined considering the two matrices C_2, C_3 with $P = Q = M = 10$ sub-intervals on x, y and z-axis.(Figure 4.8). The same procedure is applied to the other saddle. This time the eigenvectors are complex conjugated:

$$\mathbf{v}_{1,2} \approx (0.9817, -0.0088 \pm 0.08731i, -0.0552 \pm 0.1599i).$$

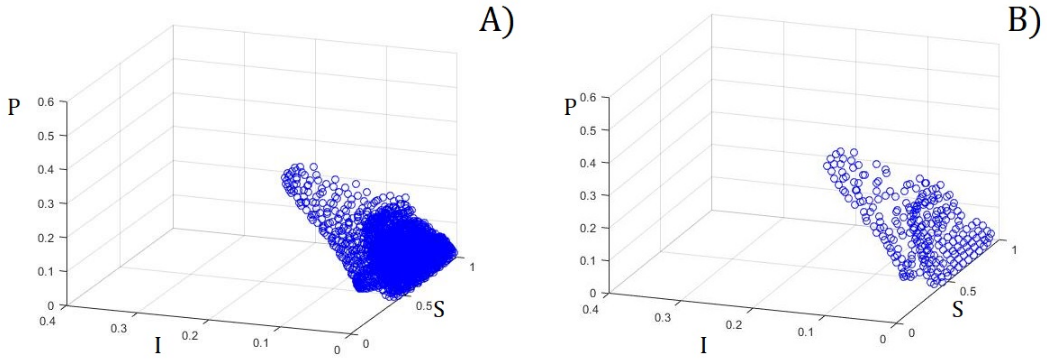

Figure 4.9: A) Scattered data on invariant manifold of saddle E_{s_2} for the model (4.5)–(4.7) ; B) Refinement of the scattered data considering $M = P = 15$ sub-intervals.

Therefore we generate the ellipse considering the real and the complex part as semi-axes. The separatrix points are obtained considering the eigenvectors rescaled of a factor 0.02 and 0.04 and then they are refined considering $M = 15$ and $P = 15$ sub-interval on x and y-axis (Figure 4.9). This surface separates the basins of the two stable points E_1 and E_2. All the points lying outside the red surface evolve toward the origin. Finally we approximate the two surfaces (Figure 4.8C) applying the MLS approximant using the Wendland C^2 compactly supported function with the shape parameter $\epsilon = 3$ and considering 60 evaluation points $\mathbf{y}$ (Figure 4.10).

4.5.2 Periodic attractors

To conclude the test and the analysis of this chapter we present another predator-prey model, but this time we choose a set of parameters that induces a complex dynamics with the appearance of periodic orbits, [56]:

$$\frac{dN}{dt} = rN(1-N) - \frac{NP}{h+N}, \tag{4.9}$$

$$\frac{dP}{dt} = \frac{NP}{h+N} - mP - \mu iP, \tag{4.10}$$

$$\frac{di}{dt} = i\left((\beta P - \mu)(1-i) - \frac{N}{h+N}\right). \tag{4.11}$$

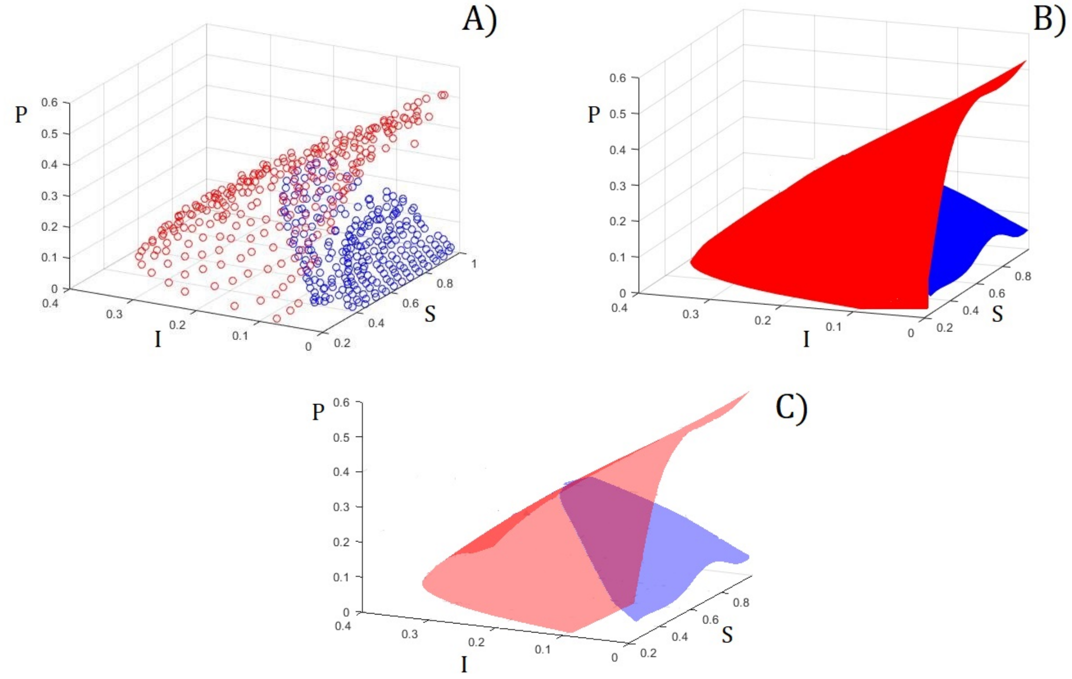

Figure 4.10: A) Scattered data of the two invariant manifolds. B), C) Reconstruction of the two invariant manifolds.

The model represents a predator-prey dynamics ($N - P$), where predators suffers of a disease and i is the prevalence of the infected on the entire population $i = \frac{I}{P}$. In the following table we resume all the parameters and their meaning:

Parameter	Biological Meaning
r	Per-capita growth rate
$\frac{NP}{h+N}$	Predation
m	Natural per-capita death-rate
β	Transmissibility of the disease
μ	Death rate of infected prey

In [56] two relatively models are analyzed. Here we focus only on the density-transmission case. Despite the simplicity of the model the authors observe quasi-periodicity, torus, oscillation and even chaos. Such complex behavior means that small changes to parameters or initial conditions can have large effect on the biological system in long term. Therefore the reconstruction of the separatrix offers an important tool to study the vector field and the biological dynamics.

When $\mu = 2, r = 0.5, h = 0.1, m = 0.2, \beta = 27.4$ the system is tri-stable among the disease-free predator prey oscillation, a coexistent torus and the coexistent equilibrium $E_1 \approx\equiv (0.6955, 0.1211, 0.3371)$.

Here we reconstruct the separatrix manifold between the coexistent torus and the steady state E_1 by considering the saddle coexistence point $E_{s_1} \approx (0.1212, 0.0972, 0.174)$.

The Jacobian matrix admits two complex conjugate eigenvalues λ_1 and λ_2 and one real positive λ_3, presenting an attracting saddle.

We take $N = 20$ points on the ellipse generated by the two vectors: $\mathbf{v}_1 \approx (0.1293, -0.0158, -0.9633)$ and $\mathbf{v}_2 \approx (-0.0389, -0.2315, 0)$, representing respectively, the real and the imaginary part of the complex eigenvectors.

In Figure 4.11A the red curve represents a trajectory evolving toward the fixed point while the green one represents the limit torus.

Finally the manifold is reconstructed by considering again the Wendland C^2 function with the shape parameter $\epsilon = 5$ (Figure 4.11B).

To conclude the analysis of the phase-space, we detect the tipping points lying between the basins of the two periodic attractors. We find the invariant stable

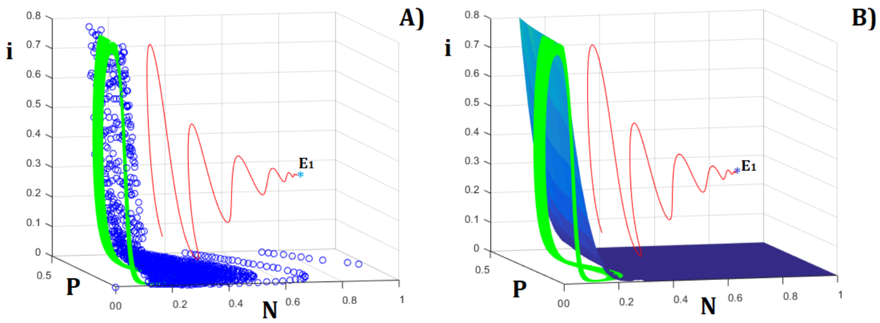

Figure 4.11: A)In blu the scattered data lying on the invariant manifold. In red it is represented the trajectory of the point $P_1 \equiv (0.3, 0.3, 0.15)$, in green the coexistent torus starting from the point $P_2 \equiv (0.1, 0.2, 0.4)$. The values of the parameters are: $\mu = 2, r = 0.5, h = 0.1, m = 0.2, \beta = 27.4$. B) Reconstruction of the surface

manifold of the saddle $E_{s_2} \equiv (1, 0, 0)$. In this case the surface is more complicated respect the others considered: it follows the trajectories of the endemic torus (green curves on Figure 4.12). Since the two periodic attractors are very close, the reconstruction results quite confusing. In Figure 4.12B we show both the scattered surfaces detected, the limit torus in green and the disease free oscillation in black.

4.6 Conclusions

In the first part of this thesis we address the analysis of dynamical systems. In particular we focus on the study of the basins of attraction of a multi-stable model, through the reconstruction of separatrix surfaces.

Starting from the bisection method present in literature, we modify the detection procedure, applying the vector field topology.

We underline as the invariant manifolds of saddle points represent the separatrix requested. The new method local approximates the separatrix points and considerably reduces the computational cost respect the previous procedure.

Using the knowledge of meshless method, we employ a Moving Least Squares method to reconstruct and to reconnect the manifolds. Working in a three dimensional space, it is possible using the explicit formula to obtain the Lagrange

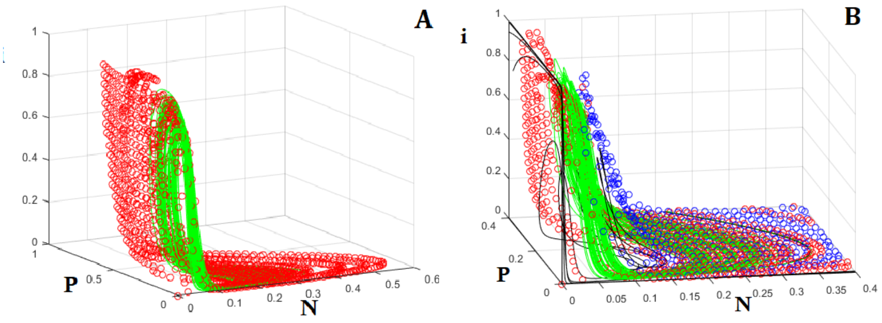

Figure 4.12: A) In green the limit stable torus. In red are represented the tipping points lying on the separatrix between the two periodic attractors. B) In red and in blue are represented the two different scattered surfaces. In green the coexistent torus and in black the disease-free oscillation. The parameters are the same of Figure 4.11.

multipliers and consequently the MLS approximant. This allows to avoid the resolution of any systems. The Radial Basis Functions are considered as weight functions, governing the influence of the data. They represent a good choice, decreasing with the distance between the points. In particular we use the compactly supported functions, avoiding to include the approximation data sites too far from the evaluation point and focusing on the local approximation.

Several numerical examples are presented in order to test the new algorithm. In particular, thanks to the reconstruction of the basins of attraction, it was possible to give a more completeness on the analysis of the Allee effect in a predator-prey model with cooperative predators, suffering of an infectious disease.

This algorithm could be applied to multi-stable models with any number of stable points. In fact the procedure presented is applied to each saddle point of the model analyzed. In particular is not influenced on the presence of complex attractors, such as limit cycle or torus. This kind of detection strategies yields good results for most topologies except for focus saddle with strong circulation that can intersect the seeding ellipse, for which the reconstruction is still unstable.

The separatrix reconstruction arises as an important task in the analysis of the dynamical models. It gives a better interpretation of the future outcomes of a dynamical systems, giving to the researchers the possibility to prevent the threshold state subject to regime shift. Therefore they could start operations to change the eco-systems state with knowledge and reason, allowing a better management of the phenomenon dynamics.

Chapter 5

Meshless Particle Methods

The meshless methods have gained increasing interest in many area of the sciences [1, 2, 3, 4, 26, 27, 69, 47, 66, 99]. For their adaptable and ductility, they could deal with several physics problems. In the first part of this thesis we have considered a Moving Least Squares method to reconstruct the surfaces and consequently analyze the basins of attraction of dynamical models.

Now we are focusing on a class of procedures called Meshless Particle Method (MPM) which are employed to solve astrophysics, oceanografic, physic phenomena. As the name suggests, these methods use a finite number of discrete particles to describe the entire continuous system and to record the motion of the problem. These MPMs were first developed to compensate the limitation of the grid algorithms in dealing with particular features such as the large deformations of the problem domain, moving material interfaces or deformable boundaries. In fact, these new characteristics pose great challenges to numerical simulations with the mesh based methods. Evolving the system in space and in time, for each step there are different spacial configurations, therefore a new discretization of the model is required. On the contrary, the great advantage of the MPMs is that it is not required any connectivity law or predefine structure between the particles involved. Therefore, even with complex boundary conditions the discretization is simple and does not change at each temporal step.

The approximation is not influenced by the problems scale, there are many methods developed in order to deal with micro-scale [31, 59, 111] to even astrophysics dimension [41, 54, 55]. These characteristics makes the methods suitable for different applications, therefore even if an approximation procedure born to deal with some specific science field, it could easily adapted to other kind of problems.

Considering the dynamical systems, we have dealt with variables evolving only on time, thus the models analyzed were represented by systems of ordinary differential equations (ODEs). However, especially in physics phenomena, the configuration of the systems changes in the space domain. Therefore the problems studied are modeled by means of Partial Differential Equations (PDEs). Obtaining analytical solutions for such systems is even more complicated and is not usually possible. Then the numerical efforts have been made in seeking the approximation.

The first step to deal with these problems is the discretization of the domain to provide an approximation for the values of the field functions and its derivatives at any evaluation point. There are two different possible approach: the Eulerian and the Lagrangian method. In the first case the particle frame is fixed and any point represents an interpolation data, but new points may be added where there is need for increased accuracy. Otherwise the Lagrangian specification of the field is an approach following the particles, both in space and time and points may be added or deleted in order to maintain a prescribed sampling density.

If the domain is not already discrete or presenting a particular density representation then it is required an initial particles distribution. In literature already exists several triangulations for $2D$ and $3D$ domains, already coded in software packages. Then, the particles could be chosen as the centers of these triangular mesh or even both as center and nodes. An other idea, it is to consider one of the several distributions already employed in numerical field such as: Sobol points [100], Halton [53] or even random points.

Following the same idea presented for the MLS method, to approximate a function f in a particular point $\mathbf{x}$, are considered the information of all neighboring particles influencing the point:

$$f(\mathbf{x}) = \sum_{j=1}^{N} \Phi_j(\mathbf{x}) f(\boldsymbol{\xi}_j) \tag{5.1}$$

where $f(\boldsymbol{\xi}_j)$ are the data measured at the N neighboring data sites $\boldsymbol{\xi}_j$ and Φ_j

represent the weight functions. These latter can be used for establishing set of discretized system equations using strong form, weak form or both.

These methods are ideally suited to simulate problems dominated by complex dynamics. In particular the lack of mesh significantly simplifies the model implementation and its parallelization.

Nowadays there are several particle methods [15, 25, 41, 76, 81, 90]. One of the first method and large used today is the Smoothed Particle Hydrodynamics (SPH) [79, 80]. The application of this method to a wide range, has led to significant extensions and improvements of the original procedure. The numerical aspects have been gradually improved and corrective methods where also proposed [71, 83, 98, 103]. However, there are still many modifications to develop, in order to obtain the same applicability and diffusion of the grid methods. In this part of the thesis we are focused our research in restoring the accuracy in approximating a function and its derivatives.

5.1 Smoothed Particle Hydrodynamics Method

The Smoothed Particle Hydrodynamics method was developed by Gingold and Monaghan [44] and Lucy [73] in 1977, to analyze astrophysical problems [43, 78] and later widely extended for applications to problems of continuum solid and fluid mechanics. It is a meshless Lagragian particle method where the coordinates move with the fluid. Nowadays the SPH method and its variants are the major type of particle methods and have been incorporated into many commercial code. It is fundamental based on two key steps: the first is the integral representation or *kernel approximation* and the second is the *particle approximation.*

The first step considers the representation of a function f by means of its integration with the Delta Dirac function δ.

Let $f(\mathbf{x}) \in \mathbb{R}$, $\mathbf{x} = \left(\mathbf{x}^{(1)}, ..., \mathbf{x}^{(d)}\right)$ and $\boldsymbol{\xi} = \left(\boldsymbol{\xi}^{(1)}, ..., \boldsymbol{\xi}^{(d)}\right) \in \mathbb{R}^d$, then the following identity holds:

$$f(\mathbf{x}) = \int_{\Omega} f(\boldsymbol{\xi})\delta(\mathbf{x}, \boldsymbol{\xi})d\boldsymbol{\xi} \tag{5.2}$$

where Ω is the problem domain and

$$\delta(\mathbf{x}, \boldsymbol{\xi}) = \begin{cases} 1 & \mathbf{x} = \boldsymbol{\xi} \\ 0 & \mathbf{x} \neq \boldsymbol{\xi} \end{cases}$$

is the Dirac Delta function.
If the function f is defined and continuous on Ω then the representation (5.2) is exact. By replacing the Delta function with a kernel $\mathsf{K}(\mathbf{x}, \boldsymbol{\xi}; h)$ we obtain the *kernel approximation*.

Definition 5. *Let be* $f : \Omega \subset \mathbb{R}^d \to \mathbb{R}$, $d \geq 1$, *the kernel approximation is defined as*

$$< f_h(\mathbf{x}) >:= \int_\Omega f(\boldsymbol{\xi})\mathsf{K}(\mathbf{x}, \boldsymbol{\xi}; h) d\Omega \tag{5.3}$$

with $\mathbf{x} = (x^{(1)}, ..., x^{(d)})$, $\boldsymbol{\xi} = (\xi^{(1)}, ..., \xi^{(d)}) \in \Omega$, $h \in \mathbb{R}$.

The function $\mathsf{K}(\mathbf{x}, \boldsymbol{\xi}; h)$ is named *kernel function* and h is the *smoothing length* but it is equivalent to the shape parameter introduced in the previous chapters. Therefore it localizes the influence of the kernel function. This latter must satisfies some conditions in order to obtain a good approximation.
First, it is considered the normalization condition:

$$\int_\Omega \mathsf{K}(\mathbf{x}, \boldsymbol{\xi}; h) d\Omega = 1.$$

It is called unity condition too, because the kernel represents a partition of unity of the domain. When the smoothing length approaches zero the kernel function approximates the Dirac Delta function:

$$\lim_{h \to 0} \mathsf{K}(\mathbf{x}, \boldsymbol{\xi}; h) = \delta(\mathbf{x}, \boldsymbol{\xi}).$$

It is further required the kernel to be sufficiently smooth and if it is even, then it is proven a second order of accuracy [68]. In fact the error can be estimated by means of Taylor series expansion of $f(\boldsymbol{\xi})$ around the point $\mathbf{x}$:

$$
\begin{aligned}
< f_h(\mathbf{x}) >= \int_\Omega \left[f(\mathbf{x}) + f'(\mathbf{x})(\boldsymbol{\xi} - \mathbf{x}) + \mathcal{O}(|\boldsymbol{\xi} - \mathbf{x}|^2) \right] \mathsf{K}(\mathbf{x}, \boldsymbol{\xi}; h) d\boldsymbol{\xi} = \\
= f(\mathbf{x}) \int_\Omega \mathsf{K}(\mathbf{x}, \boldsymbol{\xi}; h) d\boldsymbol{\xi} + \\
+ f'(\mathbf{x}) \int_\Omega (\boldsymbol{\xi} - \mathbf{x}) \mathsf{K}(\mathbf{x}, \boldsymbol{\xi}; h) d\boldsymbol{\xi} + \mathcal{O}(h^2). \quad (5.4)
\end{aligned}
$$

By considering $\boldsymbol{K}$ as even function, it follows that $(\boldsymbol{\xi} - \mathbf{x})\mathsf{K}(\mathbf{x}, \boldsymbol{\xi}; h)$ is an odd function then:

$$
\int_\Omega (\boldsymbol{\xi} - \mathbf{x}) \mathsf{K}(\mathbf{x}, \boldsymbol{\xi}; h) d\boldsymbol{\xi} = 0
$$

and for the unity condition we obtain:

$$
< f_h(\mathbf{x}) >= f(\mathbf{x}) + \mathcal{O}(h^2). \quad (5.5)
$$

However one could use a kernel that does not satisfy some of the above conditions and in this case the accuracy order is not guaranteed.

When the entire domain is represented by a finite number of particles the kernel approximation is discretized, obtaining the particles representation.

Definition 6. *Given a set of data sites* $\Xi = \left\{\boldsymbol{\xi}_j\right\}_{j=1}^N \subset \Omega$ *and the corresponding measurements* $\left\{y_j = f(\boldsymbol{\xi}_j)\right\}_{j=1}^N \in \mathbb{R}$*, the particle approximation of the function is defined as*

$$
f_h(\mathbf{x}) := \sum_{j=1}^N f(\boldsymbol{\xi}_j) \mathsf{K}(\mathbf{x}, \boldsymbol{\xi}_j; h) d\Omega_j, \quad (5.6)
$$

where $d\Omega_j$ *is the measure of the subdomain* Ω_j *associated to each data site and the triple* $(\mathsf{K}, \Xi, \mathrm{h})$ *essentially characterizes the approximation.*

The SPH method is widely used, but it still suffers of some problems working with non uniform data distribution. Despite all the algorithms developed in the years to restore the stability and the accuracy of the standard method, there still needs of improvements.

5.2 SPH numerical behavior

In this section we present some numerical simulations to test the method and to show the advantages and the limitations of the standard SPH method.

We have conducted experiments considering the approximation of some test functions, originally proposed in the ACM Transaction Software Packages [91, 105]:

$$f(x^{(1)},x^{(2)}) = 16x^{(1)}x^{(2)}(1-x^{(1)})(1-x^{(2)}), \tag{5.7a}$$

$$f(x^{(1)},x^{(2)}) = \frac{1}{9}tanh(9(x^{(2)}-x^{(1)})+1), \tag{5.7b}$$

$$f(x^{(1)},x^{(2)}) = \frac{1.25+cos(5.4x^{(2)})}{6+6(3x^{(1)}-1)^2}. \tag{5.7c}$$

Here we present the results taking into account the bi-variate functions, depicted in Figure 5.1.

Any function $K(\mathbf{x},\boldsymbol{\xi};h)$ with the properties listed in previous paragraph can be employed as smoothing kernel function. Being a smooth infinitely differentiable function, a common and suitable choice is the Gaussian function

$$\mathsf{K}_1(\mathbf{x},\boldsymbol{\xi};h) = \frac{1}{h^d\sqrt{\pi^d}}e^{-\frac{\|\boldsymbol{\xi}-\mathbf{x}\|_2^2}{h^2}},$$

where the dimensional constant $\alpha_d = 1/h^d\sqrt{\pi^d}$ is to satisfy the unity condition requirement.

This kernel function will be employed in the approximation, centered in different data sets, taken in number as the progression: $(2^n+1)^2$. Gridded, Halton, Sobol and random points are taken as data sequences and we will refer to these sets as $\Xi_G, \Xi_H, \Xi_S, \Xi_R$. The second and third ones are available in MATLAB$^{@}$ Statistics and Machine Learning Toolbox as *haltonset* and *sobolset*, respectively. The former was introduced by J.H. Halton [53] and the latter by I.M. Sobol [100]. The random points are generated by means of the random function of MATLAB$^{@}$. The evaluation points $\{\mathbf{x}_1,...,\mathbf{x}_M\}$ are on a regular mesh layed out over the computational domain. For all the simulations M=1600, $\Omega=[0,1]^2$ and the Voronoi tessellation is adopted to define Ω_j. In Figure 5.2 we show N=289 data sites for the four data sequences $\Xi_G, \Xi_H, \Xi_S, \Xi_R$ and the M evaluation points.

The following formulas are adopted to estimate the accuracy of the solution:

$$MAE := \max_{1 \le i \le M} |f_h(\mathbf{x}_i) - f(\mathbf{x}_i)|, \tag{5.8}$$

$$RMSE := \sqrt{\frac{\sum_{i=1}^{M} |f_h(\mathbf{x}_i) - f(\mathbf{x}_i)|^2}{M}}, \tag{5.9}$$

$$MEAN := \frac{\sum_{i=1}^{M} |f_h(\mathbf{x}_i) - f(\mathbf{x}_i)|}{M}. \tag{5.10}$$

In the discussion we will observe the convergence rate of the error $O(h^{(rate)})$ computed as:

$$rate = \frac{log(\frac{e_{n-1}}{e_n})}{log(\frac{h_{n-1}}{h_n})} \tag{5.11}$$

where e_{n-1} and e_n are the errors for two subsequently data sequences with h_{n-1} and h_n fixed respectively as the *fill-distance* [16, 33, 109]:

$$h_{\Xi,\Omega} = \sup_{\mathbf{x} \in \Omega} \min_{\boldsymbol{\xi}_j \in \Xi} \|\boldsymbol{\xi}_j - \mathbf{x}\|_2 \tag{5.12}$$

for the two data sets.

First of all, we show as the smoothing lenght h influences the approximation goodness. To this aim, in Figure 5.3, by fixing the data number to $N = 1089$, we plot the maximum absolute error (MAE), by varying h and for different data-set distributions.

For a complete overview, in Table 5.1 are reported the values of h_Ξ and the MAE, RMSE, MEAN error by considering $\Xi_G, \Xi_H, \Xi_S, \Xi_R$ with N=1089. The standard method usually does not yield to satisfactory results and by increasing the data density in Ω the accuracy slightly improves for the first few increased values as we observe in Figure 5.4.

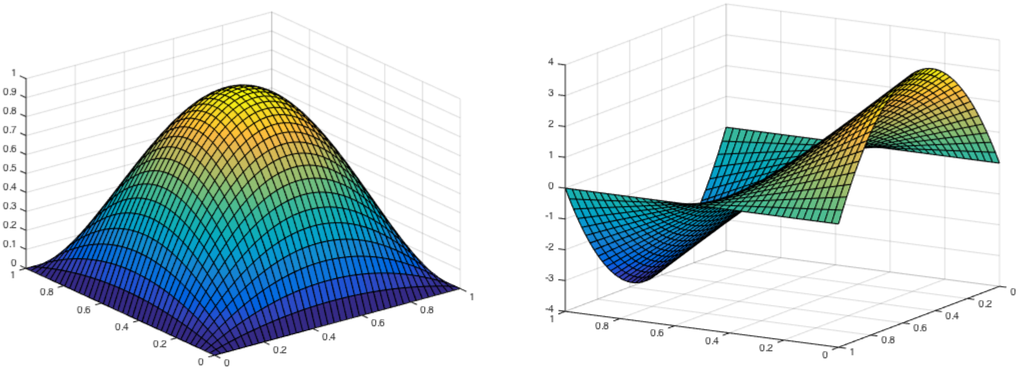

(a) Test function (4a)

(b) Test function (4a) - $\mathcal{D}_{x^{(1)}} f$

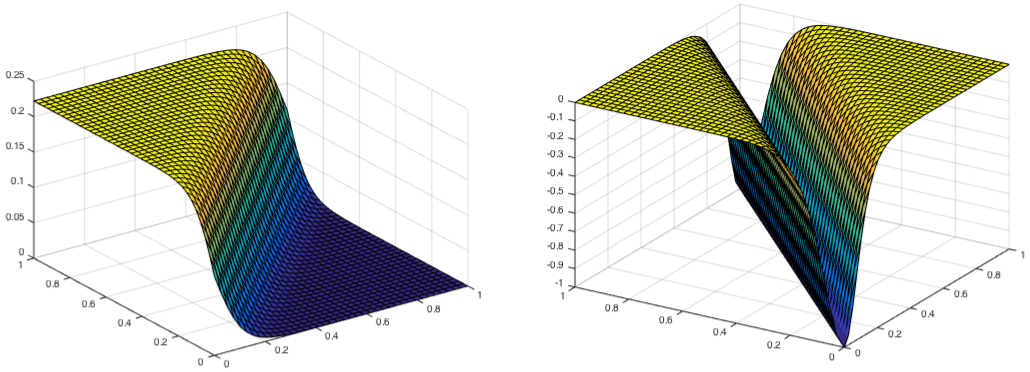

(c) Test function (4b)

(d) Test function (4b) - $\mathcal{D}_{x^{(1)}} f$

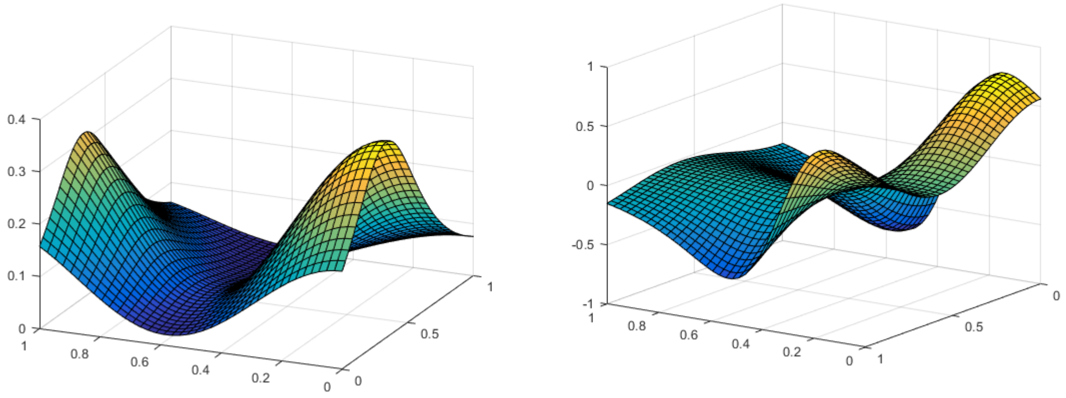

(e) Test function (4c)

(f) Test function (4c) - $\mathcal{D}_{x^{(1)}} f$

Figure 5.1: Test functions (left) and their first derivatives (right) used in the numerical experiments.

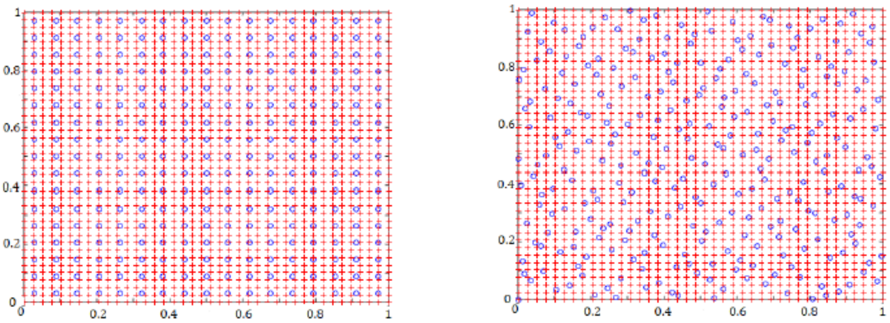

(a) Gridded data (b) Halton data

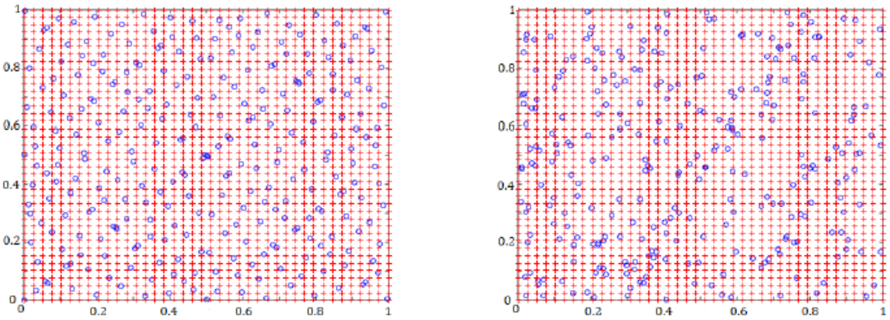

(c) Sobol data (d) Random data

Figure 5.2: The blue circles as the set of $N = 289$ data sites $\boldsymbol{\xi}_j$; the red crosses as the set of M=1600 evaluation points $\mathbf{x}_i$.

In Figure 5.5 we display the results obtained in approximating the derivatives of the function. We consider a uniform grid in the unity square domain. By increasing the data density, the results show the limit of the standard SPH method suffering from several drawbacks. Analogous conclusions are reached with the data sets Ξ_H, Ξ_S, Ξ_R and by approximating the derivatives along the $x^{(2)}$ direction.

From these simulations we observe as the approximation of the derivatives via standard SPH is poor and it is not according with the second order of accuracy claimed in the previous sections. This is due because the estimation of error in equation (5.5) refers to the kernel approximation. In particular, the SPH discretization makes reference to a set of data for which the conditions, valid for the kernel approximation, are not always preserved. For instance, when data near the boundary of the problem domain or with irregular data distribution are consid-

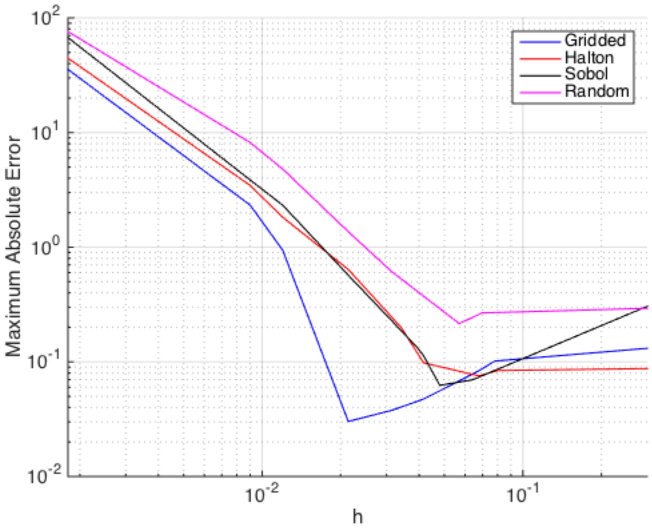

Figure 5.3: Maximum absolute error vs. h for N=1089 data sites in $\Xi_G, \Xi_H, \Xi_S, \Xi_R$.

Table 5.1: MAE, RMSE, MEAN error with h_Ξ - N=1089 - Test function (5.7a)

	MAE	RMSE	MEAN	h_Ξ
gridded data	0.0302	0.0104	0.0072	0.0214
Halton data	0.0753	0.0214	0.0162	0.0680
Sobol data	0.0624	0.0184	0.0124	0.0560
random data	0.2157	0.0353	0.0226	0.0570

ered, due to the unbalanced contribution to the discretized summations.

The aim of our research is to improve the standard method obtaining an approximation accuracy of any desired order for the function and its derivative. Many techniques have been devised to alleviate these problems and some of these have been documented in [12, 70, 71, 72]. To accomplish this goal we consider the Taylor series expansion of the trial solution. The improved method computes simultaneously the approximation of the function and its derivatives. In this way the lower order derivative is not involved in computing the higher order one. Moreover this procedure is appealing because allows to improve the accuracy without changes on the kernel function. These features avoid unphysical results such as negative values for variables, representing un-significant real states.

In the next section we will discuss on the basic idea of the improved approach

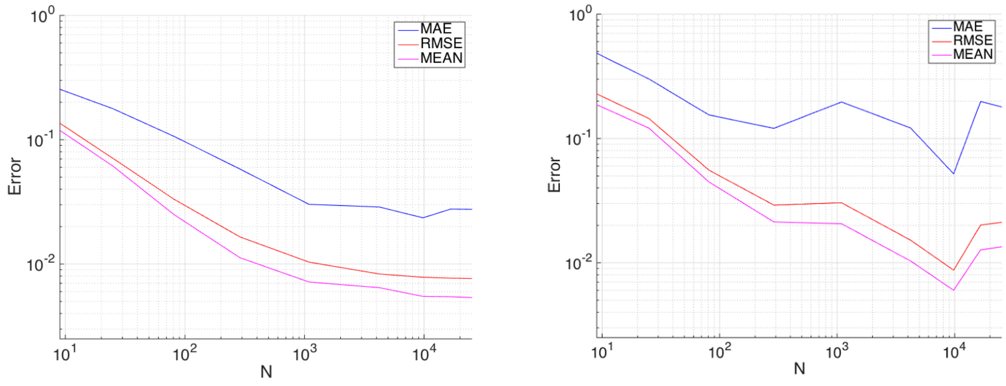

(a) Gridded data

(b) Halton data

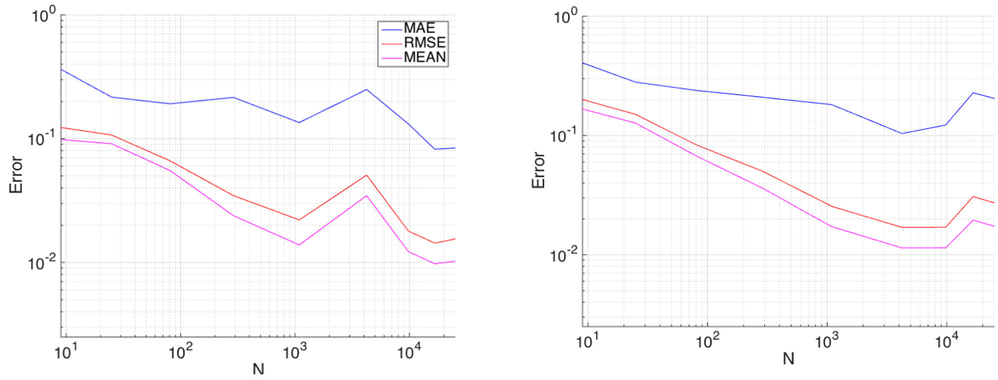

(c) Sobol data

(d) Random data

Figure 5.4: Error versus the number of data in $\Xi_G, \Xi_H, \Xi_S, \Xi_R$. Test function (5.7a).

coupled with some validation results.

5.3 Enhancing approximation

To ensure the 1-*st* order of accuracy for the kernel approximation we consider the Taylor expansion of $f(\boldsymbol{\xi})$, retaining only the first term, multiplying for the kernel function and integrating over Ω w.r.t. the variable $\boldsymbol{\xi}$

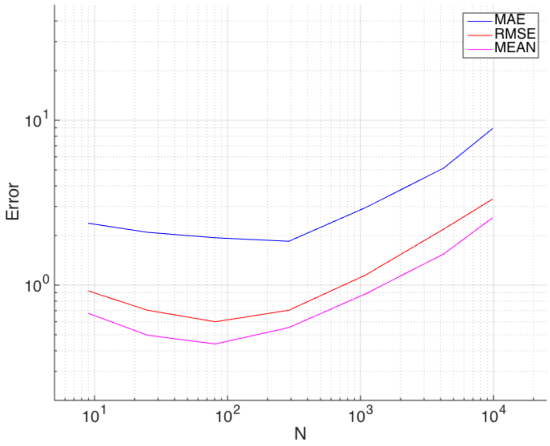

Figure 5.5: Error versus the number of data in Ξ_G for $\mathcal{D}_{x^{(1)}} f$. Test function (5.7a).

$$\int_\Omega f(\boldsymbol{\xi})\mathsf{K}(\mathbf{x},\boldsymbol{\xi};h)d\Omega = \int_\Omega f(\mathbf{x})\mathsf{K}(\mathbf{x},\boldsymbol{\xi};h)d\Omega + \int_\Omega O(h)\mathsf{K}(\mathbf{x},\boldsymbol{\xi};h)d\Omega, \tag{5.13}$$

$$f(\mathbf{x}) = \frac{\int_\Omega f(\boldsymbol{\xi})\mathsf{K}(\mathbf{x},\boldsymbol{\xi};h)d\Omega}{\int_\Omega \mathsf{K}(\boldsymbol{x},\boldsymbol{\xi};h)d\Omega} + O(h). \tag{5.14}$$

The corresponding discrete formulation is

$$f(\mathbf{x}) = \frac{\sum_{j=1}^{N} f(\boldsymbol{\xi}_j)\mathsf{K}(\mathbf{x},\boldsymbol{\xi}_j;h)d\Omega_j}{\sum_{j=1}^{N} \mathsf{K}(\mathbf{x},\boldsymbol{\xi}_j;h)d\Omega_j} + O(h). \tag{5.15}$$

The requirement of the unity condition for the kernel function corresponds to assure the first order of accuracy-or 0-*th* order of consistency (k=0) for the kernel approximation, but it is not always assured for the discrete counterpart. So we proceed in the approximation by adopting the (5.15) instead of (5.6) to improve the results.

In Figure 5.6 are plotted the numerical results obtained in approximating the test function (5.7a) with the data sets $\Xi_G, \Xi_H, \Xi_S, \Xi_R$. We increase the data density in the unit square domain. By comparing the Figure 5.4 with Figure 5.6, the improvements in the approximation are underlined. In the Tables 5.2 and 5.3, the errors and the convergence rate are reported referring to gridded and random data sets. Therefore the theoretical assumptions are confirmed by the numerical simulations, making evidence of a less accurate approximation for data in Ξ_R. In Figure 5.7 we summarize the maximum absolute error for the test functions (4b) and (4c) for the different data sequences $\Xi_G, \Xi_H, \Xi_S, \Xi_R$.

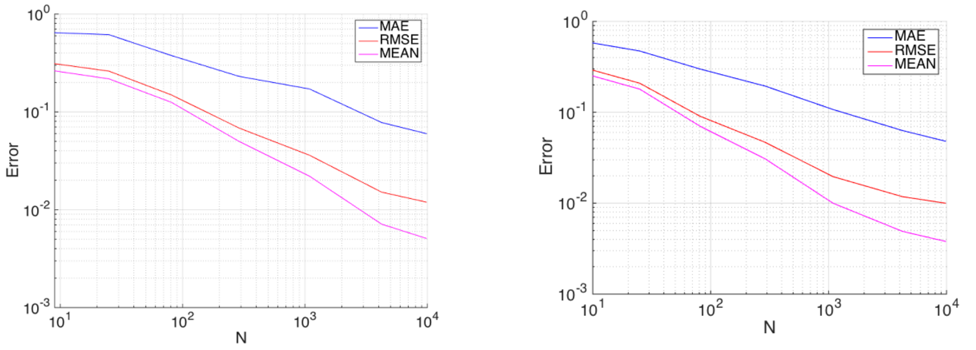

(a) Gridded data

(b) Halton data

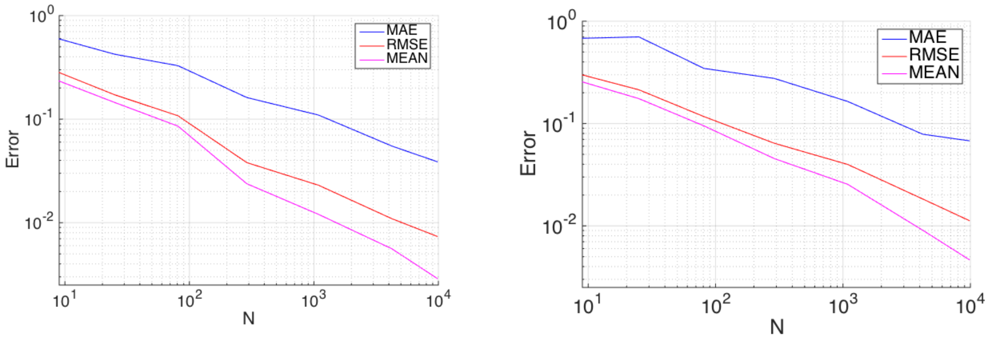

(c) Sobol data

(d) Random data

Figure 5.6: k=0. Error versus the number of data in $\Xi_G, \Xi_H, \Xi_S, \Xi_R$. Test function (5.7a).

5.3.1 Higher order of accuracy

Now, to extend the results of the previous section, we generate methods with higher approximation order by taking into account the Taylor series expansion of

Table 5.2: k=0. MAE, RMSE, MEAN error for data in Ξ_G. Test function (5.7a). Data used in the Figure 5.6(a).

N	f						h_Ξ
	MAE	*rate*	RMSE	*rate*	MEAN	*rate*	
9	0.5097	–	0.2178	–	0.1849	–	0.2357
25	0.3556	0.7046	0.1203	1.1627	0.0923	1.3603	0.1414
81	0.2136	0.8672	0.0592	1.2047	0.0368	1.5642	0.0786
289	0.1175	0.9402	0.0283	1.1629	0.0136	1.5640	0.0415
1089	0.0616	0.9723	0.0142	1.0435	0.0052	1.4407	0.0214
4225	0.0316	0.9865	0.0072	0.9898	0.0026	1.0399	0.0109
16641	0.0160	0.9950	0.0037	0.9733	0.0013	1.0134	0.0055
66049	0.0080	0.9968	0.0018	0.9971	6.40e-04	1.0046	0.0028

Table 5.3: k=0. MAE, RMSE, MEAN error for data in Ξ_R. Test function (5.7a). Data used in the Figure 5.6(d).

N	f						h_Ξ
	MAE	*rate*	RMSE	*rate*	MEAN	*rate*	
9	0.6812	–	0.2986	–	0.2552	–	0.4398
25	0.7022	-0.1035	0.2136	1.1417	0.1751	1.2845	0.3280
81	0.3457	0.9830	0.1170	0.8355	0.0949	0.8499	0.1595
289	0.2759	0.4228	0.0642	1.1262	0.0454	1.3813	0.0936
1089	0.1643	1.4872	0.0398	1.3698	0.0255	1.6619	0.0661
4225	0.0786	1.1075	0.0183	1.1683	0.0091	1.5523	0.0340
16641	0.0398	0.6855	0.0071	0.9538	0.0030	1.1179	0.0126
66049	0.0229	1.0415	0.0041	1.0440	0.0015	1.2564	0.0074

the function $f(\boldsymbol{\xi})$ up to the order k

$$f(\boldsymbol{\xi}) = \sum_{|\alpha| \leq k} \frac{1}{\alpha!}(\boldsymbol{\xi} - \mathbf{x})^{\alpha} \mathcal{D}^{\alpha} f(\mathbf{x}) + O(h^{k+1}), \tag{5.16}$$

where $\alpha = (\alpha_1, \alpha_2, ..., \alpha_d) \in \mathbb{N}^d$ is a multi-index with $|\alpha| = \sum_{i=1}^{d} \alpha_i$, $\alpha! = \alpha_1!\alpha_2!...\alpha_d!$ and the differential operator is defined as:

$$\mathcal{D}^{\alpha} := \frac{\partial^{|\alpha|}}{(\partial_{x^{(1)}})^{\alpha_1} ... (\partial_{x^{(d)}})^{\alpha_d}}.$$

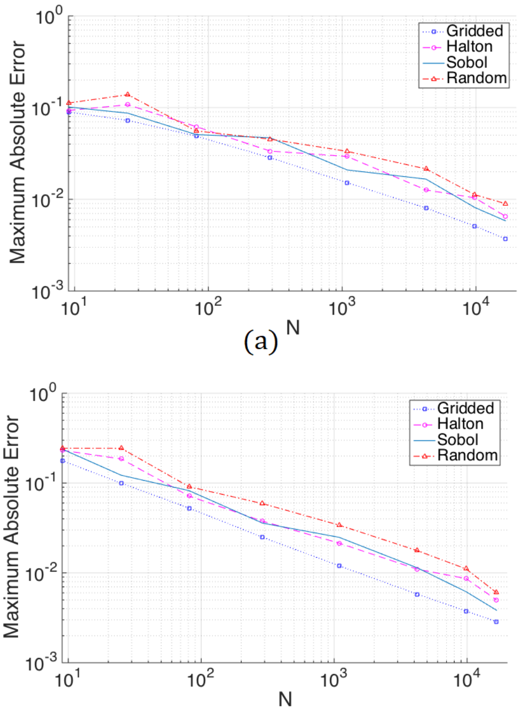

(a)

(b)

Figure 5.7: k=0. MAE versus number of data in $\Xi_G, \Xi_H, \Xi_S, \Xi_R$. (a) Test function (4b) and (b) test function (4c).

Hence, the (5.16) is multiplied for the kernel function and its derivatives up to the order k and integrated over Ω w.r.t. the variable $\boldsymbol{\xi}$:

$$\begin{aligned}
\int_\Omega f(\boldsymbol{\xi})\mathsf{K}(\mathbf{x},\boldsymbol{\xi};h)d\Omega &= \sum_{|\alpha|\le k} \frac{1}{\alpha!}\int_\Omega (\boldsymbol{\xi}-\mathbf{x})^\alpha \mathcal{D}^\alpha f(\mathbf{x})\mathsf{K}(\mathbf{x},\boldsymbol{\xi};h)d\Omega + \\
&+ \int_\Omega O(h^{k+1})\mathsf{K}(\mathbf{x},\boldsymbol{\xi};h)d\Omega \\
&\vdots \\
\int_\Omega f(\boldsymbol{\xi})\mathcal{D}^k\mathsf{K}(\mathbf{x},\boldsymbol{\xi};h)d\Omega &= \sum_{|\alpha|\le k} \frac{1}{\alpha!}\int_\Omega (\boldsymbol{\xi}-\mathbf{x})^\alpha \mathcal{D}^\alpha f(\mathbf{x})\mathcal{D}^k\mathsf{K}(\mathbf{x},\boldsymbol{\xi};h)d\Omega + \\
&+ \int_\Omega O(h^{k+1})\mathcal{D}^k\mathsf{K}(\mathbf{x},\boldsymbol{\xi};h)d\Omega.
\end{aligned}$$

In linear algebra notation, neglecting the error, the improved formulation corresponds to the point-wise linear systems:

$$< \mathbf{A}^{(k)} > \mathbf{c}^{(k)} =< \mathbf{b}^{(k)} > \tag{5.17}$$

where

$$< \mathbf{A}^{(k)} >= \begin{pmatrix} \int_\Omega \mathsf{K}(\mathbf{x}, \boldsymbol{\xi}; h) d\Omega & \dots & \frac{1}{k!} \int_\Omega (\xi^{(d)} - x^{(d)})^k \mathsf{K}(\mathbf{x}, \boldsymbol{\xi}; h) d\Omega \\ \vdots & \dots & \vdots \\ \int_\Omega \mathcal{D}^k \mathsf{K}(\mathbf{x}, \boldsymbol{\xi}; h) d\Omega & \dots & \frac{1}{k!} \int_\Omega (\xi^{(d)} - x^{(d)})^k \mathcal{D}^k \mathsf{K}(\mathbf{x}, \boldsymbol{\xi}; h) d\Omega \end{pmatrix}$$

$$\mathbf{c}^{(k)} = \begin{pmatrix} f(\mathbf{x}) \\ \vdots \\ \mathcal{D}^k_{x^{(d)}} f(\mathbf{x}) \end{pmatrix}$$

$$< \mathbf{b}^{(k)} >= \begin{pmatrix} \int_\Omega f(\boldsymbol{\xi}) \mathsf{K}(\mathbf{x}, \boldsymbol{\xi}; h) d\Omega \\ \vdots \\ \int_\Omega f(\boldsymbol{\xi}) \mathcal{D}^k \mathsf{K}(\mathbf{x}, \boldsymbol{\xi}; h) d\Omega \end{pmatrix}$$

where the notation $\mathcal{D}^k_{x^{(d)}}$ indicates that the operator is applied with the multi-index having $k_d = k$.

Now, we discretize the formulation for the function and its derivatives estimate up to order k at the evaluation point $\mathbf{x}$

$$\mathbf{A}^{(k)} = \begin{pmatrix} \sum_{j=1}^{N} \mathsf{K}(\mathbf{x}, \boldsymbol{\xi}_j; h) d\Omega_j & \dots & \frac{1}{k!} \sum_{j=1}^{N} (\xi_j^{(d)} - x^{(d)})^k \mathsf{K}(\mathbf{x}, \boldsymbol{\xi}_j; h) d\Omega_j \\ \vdots & \dots & \vdots \\ \sum_{j=1}^{N} \mathcal{D}^k \mathsf{K}(\mathbf{x}, \boldsymbol{\xi}_j; h) d\Omega_j & \dots & \frac{1}{k!} \sum_{j=1}^{N} (\xi_j{}^{(d)} - x^{(d)})^k \mathcal{D}^k \mathsf{K}(\mathbf{x}, \boldsymbol{\xi}_j; h) d\Omega_j \end{pmatrix}$$

$$\mathbf{c}^{(k)} = \begin{pmatrix} f(\mathbf{x}) \\ \vdots \\ \mathcal{D}^k_{x^{(d)}} f(\mathbf{x}) \end{pmatrix}$$

$$\mathbf{b}^{(k)} = \begin{pmatrix} \sum_{j=1}^{N} f(\xi_j)\mathsf{K}(\mathbf{x}, \xi_j; h) d\Omega_j \\ \vdots \\ \sum_{j=1}^{N} f(\boldsymbol{\xi}_j)\mathcal{D}^k\mathsf{K}(\mathbf{x}, \boldsymbol{\xi}_j; h) d\Omega_j \end{pmatrix}.$$

Solving the system provides simultaneusly approximation values for the function f with accurate order $k+1$ and of order $k+1-p$ for the derivatives of order p. To give evidence of this assertion, we consider the error vector

$$\mathbf{e}^{(k)} = \begin{pmatrix} O(h^{k+1}) \sum_{j=1}^{N} \mathsf{K}(\mathbf{x}, \boldsymbol{\xi}_j; h) d\Omega_j \\ \vdots \\ O(h^{k+1}) \sum_{j=1}^{N} \mathcal{D}^k\mathsf{K}(\mathbf{x}, \xi_j; h) d\Omega_j \end{pmatrix}$$

and the system matrix $\mathbf{A}^{(k)}$ approximated as

$$\mathbf{A}^{(k)} \cong \underbrace{\begin{pmatrix} p_{11} & \dots & p_{1k} \\ \vdots & \ddots & \vdots \\ p_{k1} & \dots & p_{kk} \end{pmatrix}}_{\mathbf{P}} \begin{pmatrix} 1 & & & \\ & h & & \\ & & \ddots & \\ & & & h^k \end{pmatrix}.$$

So, in computing the solution the error is about

$$(\mathbf{A}^{(k)})^{-1}\mathbf{e}^{(k)} \cong \begin{pmatrix} 1 & & & \\ & \frac{1}{h} & & \\ & & \ddots & \\ & & & \frac{1}{h^k} \end{pmatrix} \mathbf{P}^{-1} \begin{pmatrix} O(h^{k+1}) \sum_{j=1}^{N} \mathsf{K}(\mathbf{x}, \xi_j; h) d\Omega_j \\ O(h^{k+1}) \sum_{j=1}^{N} \mathcal{D}\mathsf{K}(\mathbf{x}, \xi_j; h) d\Omega_j \\ \vdots \\ O(h^{k+1}) \sum_{j=1}^{N} \mathcal{D}^k\mathsf{K}(\mathbf{x}, \xi_j; h) d\Omega_j \end{pmatrix} \cong \begin{pmatrix} O(h^{k+1}) \\ O(h^k) \\ \vdots \\ O(h) \end{pmatrix}.$$

In the following we report the numerical test for the function (5.7a). We require a first and second order, k=1 and k=2 in approximating the function and its derivatives. Tables 5.4 and 5.5 present the simulations with k=1, while the second order of accuracy is shown in Tables 5.6 and 5.9. Analyzing these results, we observe a good approximation, almost reaching the convergence predicted by the theory. In Figure 5.8, by fixing N=1089, we focus on the MAE comparing SPH and the improved method with k=0, k=1 and k=2. We observe that the error is reduced inside the domain and it is always present on the boundaries but a significant decrease is with k=1,2.
We conclude this section presenting the MAE for finer data locations concerning the three functions (5.7a), (5.7b), (5.7c) with the standard SPH formulation and with the modified one by varying k=0,1,2. In Figures 5.9, 5.10 and 5.11 we show the maximum absolute error versus the number of data in Ξ_G, Ξ_H, Ξ_S, Ξ_R.

The results presented are promising and satisfying, however the computational demanding could represents a limit in managing high number of data. To this aim in the next chapter we deal with some techniques to speed up the method.

Table 5.4: k=1. MAE, RMSE for data in Ξ_G. Test function (5.7a).

N	f				$\mathcal{D}_{x^{(1)}}f$				h_Ξ
	MAE	$rate$	$RMSE$	$rate$	MAE	$rate$	$RMSE$	$rate$	
9	0.3016	–	0.1424	–	2.7931	–	1.0237	–	0.2357
25	0.1158	1.8745	0.0563	0.1818	1.6832	0.9914	0.5379	1.2598	0.1414
81	0.0366	1.9596	0.0183	1.9120	0.9237	1.0207	0.2512	1.2949	0.0786
289	0.0114	1.8258	0.0052	1.9690	0.4825	1.0211	0.1131	1.2540	0.0415
1089	0.0035	1.8001	0.0014	1.9784	0.2461	1.0145	0.0530	1.1431	0.0214
4225	9.54e-04	1.9052	3.64e-04	1.9909	0.1241	1.0111	0.0268	1.0089	0.0109
16641	2.45e-04	1.9874	9.27e-05	1.9996	0.0629	0.9935	0.0134	1.0134	0.0055
66049	6.39e-05	1.9771	2.33e-05	1.9994	0.0319	0.9855	0.0067	0.9999	0.0028
96721	4.38e-05	1.9857	1.57e-05	2.0526	0.0264	0.9909	0.0056	0.9264	0.0023

Table 5.5: k=1. MAE, RMSE for data in Ξ_R. Test function (5.7a).

N	f				$\mathcal{D}_{x^{(1)}}f$				h_Ξ
	MAE	$rate$	$RMSE$	$rate$	MAE	$rate$	$RMSE$	$rate$	
9	0.5337	–	0.1925	–	2.8825	–	1.0814	–	0.4398
25	0.2936	2.0375	0.1518	0.8063	2.4489	0.5558	0.8345	0.8838	0.3280
81	0.1295	1.1353	0.0602	1.2815	1.4324	0.7437	0.4485	0.8609	0.1595
289	0.0857	0.7732	0.0235	1.7659	0.9766	0.7185	0.2333	1.2259	0.0936
1089	0.0416	2.0767	0.0116	2.0340	0.7202	0.8744	0.1350	1.5700	0.0661
4225	0.0106	2.0559	0.0031	1.9577	0.3799	0.9611	0.0597	1.2276	0.0340
16641	0.0011	2.2823	4.53e-04	1.9375	0.1711	0.8036	0.0233	0.9478	0.0126
66049	7.73e-04	0.6629	1.54e-04	2.0273	0.0960	1.0858	0.0127	1.1402	0.0074
96721	3.79e-04	2.9256	9.79e-05	1.8595	0.0859	0.4563	0.0103	0.8597	0.0058

Table 5.6: k=2. MAE for data in Ξ_G. Test function (5.7a).

N	f		$\mathcal{D}_{x^{(1)}}f$		$\mathcal{D}^2_{x^{(1)}}f$		h_Ξ
	MAE	*rate*	MAE	*rate*	MAE	*rate*	
9	0.2647	–	1.9477	—	4.5084	–	0.2357
25	0.0741	2.4917	0.8781	1.5591	2.9491	0.8306	0.1414
81	0.0146	2.7587	0.3074	1.7855	1.7288	0.9094	0.0786
289	0.0028	2.8822	0.0921	1.8941	0.9434	0.9485	0.0415
1089	3.32e-04	2.9417	0.0253	1.9473	0.4939	0.9756	0.0214
4225	4.44e-05	2.9710	0.0066	1.9737	0.2528	0.9876	0.0109
16641	5.73e-06	2.9934	0.0017	1.9831	0.1279	0.9961	0.0055
66049	7.29e-07	2.9954	4.30e-04	1.9934	0.0643	0.9532	0.0028
96721	4.11e-07	2.9954	2.94e-04	1.9959	0.0532	0.9673	0.0023

Table 5.7: k=2. MAE for data in Ξ_R. Test function(5.7a).

N	f		$\mathcal{D}_{x^{(1)}}f$		$\mathcal{D}^2_{x^{(1)}}f$		h_Ξ
	MAE	*rate*	MAE	*rate*	MAE	*rate*	
9	15.5032	–	37.2568	—	68.8620	—	0.4398
25	3.4298	5.1438	31.2706	0.5972	49.2390	1.1437	0.3280
81	0.7152	2.1742	9.7030	1.6229	49.8307	-0.0166	0.1595
289	0.3016	1.6194	3.2224	2.0675	26.2748	1.2004	0.0936
1089	0.0242	7.2410	0.9811	3.4140	5.9107	4.2828	0.0661
4225	0.0016	4.0504	0.3792	1.4286	4.4230	0.4357	0.0340
16641	3.37e-04	1.5692	0.0548	1.9487	3.7019	0.1793	0.0126
66049	3.99e-05	4.0176	0.0083	3.5404	0.8011	2.8826	0.0074
96721	3.00e-05	1.2219	0.0146	-2.3887	0.0146	-47520	0.0058

Table 5.8: k=2. RMSE for data in Ξ_R. Test function(5.7a).

N	f		$\mathcal{D}_{x^{(1)}}f$		$\mathcal{D}^2_{x^{(1)}}f$		h_Ξ
	RMSE	*rate*	RMSE	*rate*	RMSE	*rate*	
9	0.6575	–	2.2986	—	3.6311	—	0.4398
25	0.2018	4.0278	1.8702	0.7034	3.5045	0.7034	0.3280
81	0.0379	2.3202	0.5166	1.7841	3.0262	1.7841	0.1595
289	0.0096	2.5729	0.1566	2.2388	1.1947	2.2388	0.0936
1089	0.0012	5.8605	0.0518	3.1739	0.4512	3.1739	0.0661
4225	1.06e-04	3.6944	0.0137	2.0001	0.2175	2.0001	0.0340
16641	1.39e-05	2.0466	0.0027	1.6361	0.1547	0.3432	0.0126
66049	1.73e-06	3.9153	5.60e-04	2.9516	0.0427	2.4187	0.0074
96721	1.37e-06	0.9577	5.77e-04	-0.1200	0.0802	-2.5873	0.0058

Table 5.9: k=2. MEAN for data in Ξ_R. Test function(5.7a).

N	f		$\mathcal{D}_{x^{(1)}}f$		$\mathcal{D}^2_{x^{(1)}}f$		h_Ξ
	MEAN	*rate*	MEAN	*rate*	MEAN	*rate*	
9	0.1512	–	0.7934	—	2.2061	—	0.4398
25	0.0749	2.3926	0.7176	0.3425	2.2544	-0.0738	0.3280
81	0.0118	2.5671	0.1746	1.9601	1.1652	0.9152	0.1595
289	0.0020	3.3536	0.0539	2.2055	0.4935	1.6112	0.0936
1089	3.85e-04	4.6827	0.0218	2.6055	0.2133	2.4088	0.0661
4225	3.83e-05	3.4661	0.0058	1.9948	0.0810	1.4554	0.0340
16641	3.27e-06	2.4788	9.62e-04	1.8099	0.0384	0.7519	0.0126
66049	4.65e-07	3.6734	2-88e-04	2.2694	0.0152	1.7448	0.0074
96701	2.70e-07	2.3176	1.95e-04	1.6593	0.0162	-0.2748	0.0058

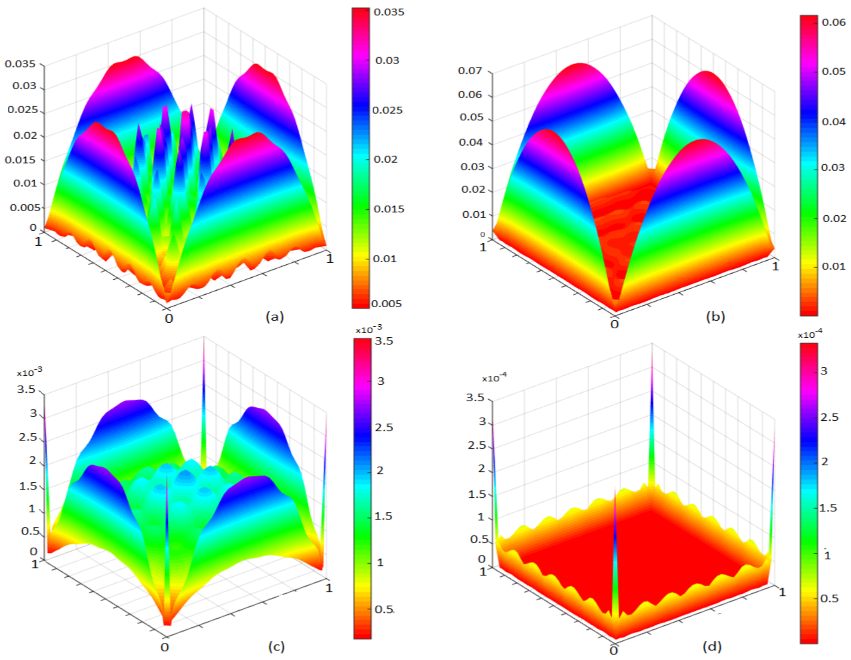

Figure 5.8: MAE for (a) SPH standard; (b) Improved method with k=0, (c) k=1, (d) k=2. N=1089 data in Ξ_G. Function test (5.7a).

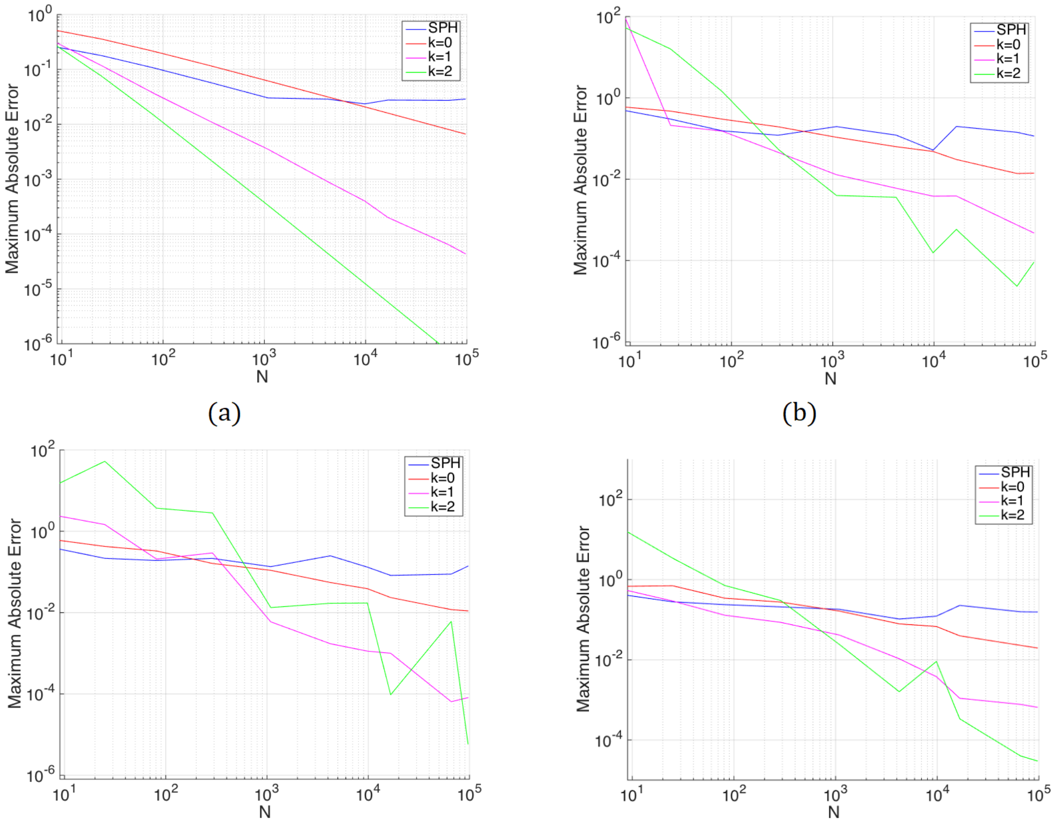

(a) (b)

(c) (d)

Figure 5.9: Function test (5.7a). Comparison of MAE on the function with the standard SPH formulation and the improved ones with k=0,1,2. (a) Gridded data; (b) Halton data; (c) Sobol data; (d) Random data.

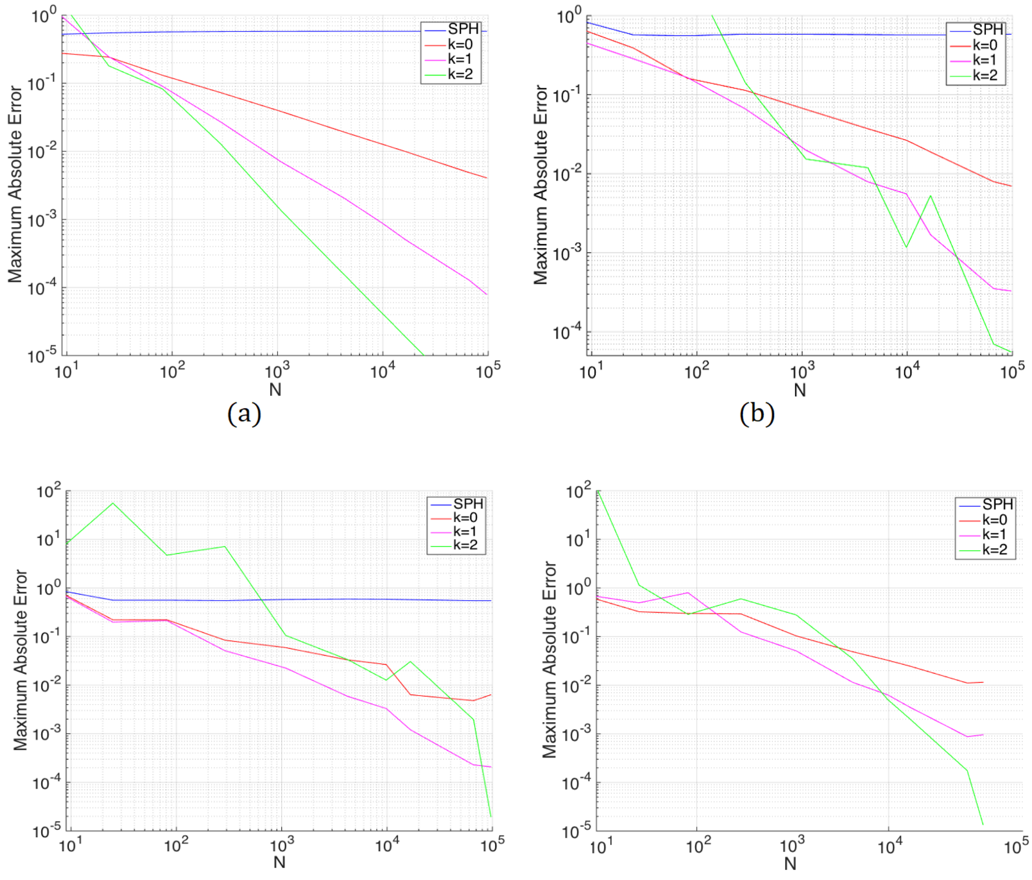

(a) (b)

(c) (d)

Figure 5.10: Function test (5.7b). Comparison of MAE on the function with the standard SPH formulation and the improved ones with k=0,1,2. (a) Gridded data; (b) Halton data; (c) Sobol data; (d) Random data.

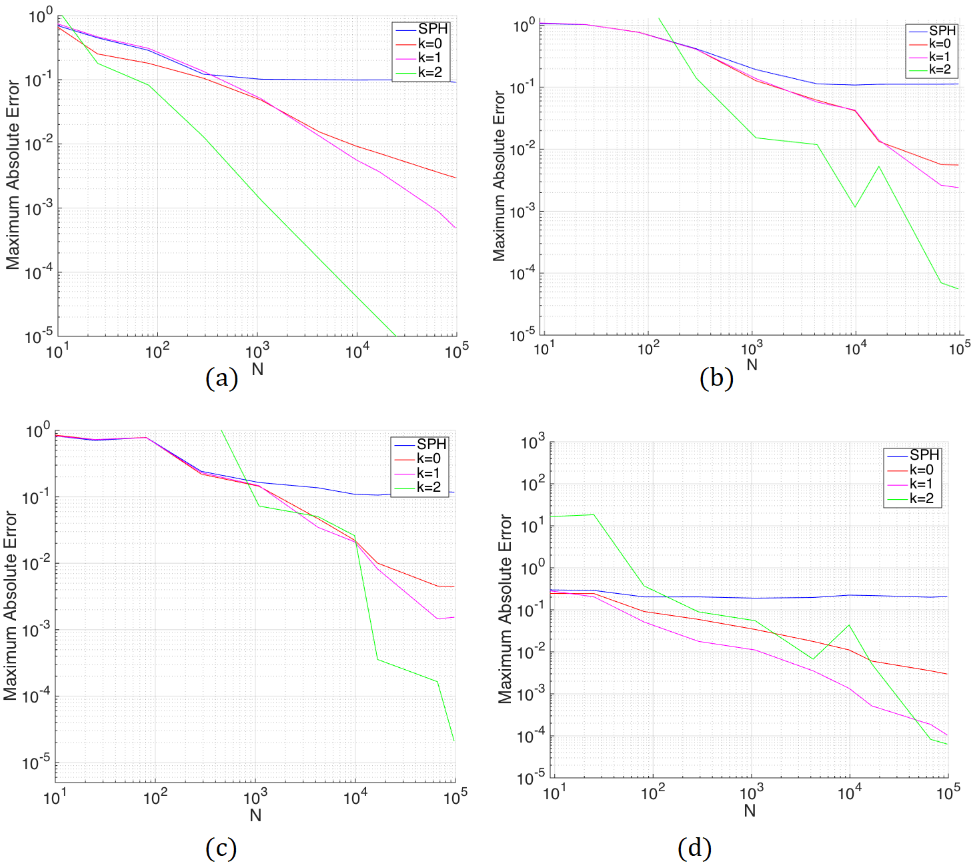

Figure 5.11: Function test (5.7c). Comparison of MAE on the function with the standard SPH formulation and the improved ones with k=0,1,2. (a) Gridded data; (b) Halton data; (c) Sobol data; (d) Random data.

Chapter 6

Computational skills

In previous chapter we have presented an enhancement to the SPH method in approximating a function and its derivatives. The method has proven to provide an accuracy of any desired order. However the computational effort is quite expensive compared to the original method. In fact for each evaluation point, we have to build and solve the linear system (5.17). The size of the system is described by the quantity

$$s_{k,d} = \frac{(d+k)!}{d!k!}$$

depending on the problem dimension d and on the order of accuracy requested k. Consequently the computational cost required is

$$C_{k,d} \approx MNs_{k,d}\left(\frac{s_{k,d}+3}{2}\right). \tag{6.1}$$

From the numerical tests presented, we notice that often the maximum error is picked only in some boundary points. Therefore, to improve the accuracy of the approximation, one could be interested on consider only these particular points instead to recompute the procedure for all. In this case, passing from $k-1$ to k order of accuracy there are needed only of $\frac{d}{2k}s_{k-1,d}[\frac{(d+2k)}{k}s_{k-1,d}+1]$ more elements to end up the matrix $\mathbf{A}^{(k)}$ starting from the matrix $\mathbf{A}^{(k-1)}$. In fact, as shown in Figure 6.1, the matrix of higher order is partial composed by the matrices of lower order.

A first approach to speed up the computation, making the large scale problems

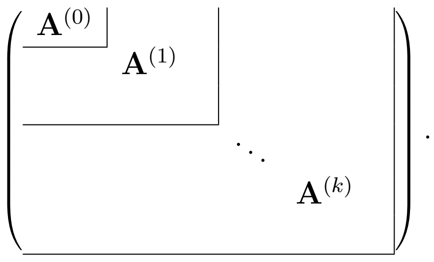

Figure 6.1: Skeleton of the matrix associated to the $(k+1)$-th order of accuracy.

tractable, is to split the matrix $\mathbf{A}^{(k)}$, by means of the matrices:

$$\mathbf{K}^{(k)} = \begin{pmatrix} \mathsf{K}(\mathbf{x}, \xi_1; h) & \mathsf{K}(\mathbf{x}, \xi_2; h) & \dots & \mathsf{K}(\mathbf{x}, \xi_N; h) \\ \vdots & \vdots & \dots & \vdots \\ \mathcal{D}^k\mathsf{K}(\mathbf{x}, \xi_1; h) & \mathcal{D}^k\mathsf{K}(\mathbf{x}, \xi_2; h) & \dots & \mathcal{D}^k\mathsf{K}(\mathbf{x}, \xi_N; h) \end{pmatrix} \tag{6.2}$$

$$\mathbf{V} = \begin{pmatrix} d\Omega_1 & & & \\ & d\Omega_2 & & \\ & & \ddots & \\ & & & d\Omega_N \end{pmatrix} \tag{6.3}$$

$$\mathbf{P}^{(k)} = \begin{pmatrix} 1 & (\xi_1^{(1)} - x^{(1)}) & \dots & \frac{1}{k!}(\xi_1^{(d)} - x^{(d)})^k \\ 1 & (\xi_2^{(1)} - x^{(1)}) & \dots & \frac{1}{k!}(\xi_2^{(d)} - x^{(d)})^k \\ \vdots & \vdots & \dots & \vdots \\ 1 & (\xi_N^{(1)} - x^{(1)}) & \dots & \frac{1}{k!}(\xi_N^{(d)} - x^{(d)})^k \end{pmatrix} \tag{6.4}$$

allowing to re-write the system as:

$$(\mathbf{K}^{(k)}\mathbf{V}\mathbf{P}^{(k)})\mathbf{c}^{(k)} = \mathbf{K}^{(k)}\mathbf{V}\mathbf{f} \tag{6.5}$$

where $\mathbf{f}$ collects the function values.

The resolution and the results are the same, but the process is faster passing from a BLAS level 1 to a BLAS level 3 [46].

However most of the computational cost is the construction of the elements of matrix $A^{(k)}$

and vector $b^{(k)}$. All these elements are constituted by the summation of the Gaussian kernel or its derivatives multiplied for different weights. To speed up this assembly procedure, in the next section we introduce a fast summation technique.

6.1 Improved Fast Gauss Transform

The Fast Gauss Transform (FGT) was introduced by Greengard and Strain [48, 49] for efficient evaluation of the Gauss transform, reducing the computational cost in computing the sum

$$G(\mathbf{x}_i) = \sum_{j=1}^{N} w_j e^{-\frac{\|\boldsymbol{\xi}_j - \mathbf{x}_i\|^2}{h^2}} \quad i = 1, ..., M \tag{6.6}$$

where w_j are the weight coefficients, $\left\{\boldsymbol{\xi}_j\right\}_{j=1}^{N} \subseteq \mathbb{R}^d$ are the centers of the Gaussian, h is the smoothing length and $\{\mathbf{x}_i\}_{i=1}^{M} \subseteq \mathbb{R}^d$ are the evaluation points.
Following the Fast Multipole Method (FMM) idea, Greengard and Strain proposed an Hermite series expansion centered at location $\mathbf{x}^*$

$$G(\mathbf{x}_i) = \sum_{\alpha \geq 0} C_\alpha h_\alpha \left(\frac{\mathbf{x}_i - \mathbf{x}^*}{h} \right)$$

where h_α is the d-dimensional Hermite function and $\alpha \in \mathbb{N}^d$ is a multi-index. The coefficient C_α represents the contribution of the centers in the approximation

$$\mathcal{C}_\alpha = \frac{1}{\alpha!} \sum_{j=1}^{N} w_j \left(\frac{\boldsymbol{\xi}_j - \mathbf{x}^*}{h} \right)^\alpha .$$

If each element of the Hermite series is truncated after k terms, then each $\mathcal{C}_\alpha$ is a d-dimensional matrix with k^d terms and the computational effort is reduced from $\mathcal{O}(MN)$ operations to $\mathcal{O}((M+N)k^d)$. However, increasing the problem dimension d, the term k^d grows exponentially, reducing the advantages of the fast summations. Afterthought, the authors work with a box data structure, involving meshes that are inefficient in high dimensions.
To overcome these limits, Yang et al. [94, 112, 113] proposes the Improved Fast Gauss Transform (IFGT), replacing the Hermite representation with the Taylor series expansion. Re-writing the exponential term as

$$e^{-\frac{\|\mathbf{x}_i-\boldsymbol{\xi}_j\|^2}{h^2}} = e^{-\frac{\|\mathbf{x}_i-\mathbf{x}^*\|^2}{h^2}} e^{-\frac{\|\boldsymbol{\xi}_j-\mathbf{x}^*\|^2}{h^2}} e^{\frac{2\left(\boldsymbol{\xi}_j-\mathbf{x}^*\right)\left(\mathbf{x}_i-\mathbf{x}^*\right)}{h^2}}$$

the first two terms can be evaluated independently. The only problem remains the evaluation of the one, where evaluation points and centers are linked. For this reason the multivariate Taylor series expansion is considered giving rise to the approximation [112]

$$\hat{G}(\mathbf{x}_i) = e^{-\frac{\|\mathbf{x}_i-\mathbf{x}^*\|^2}{h^2}} \sum_{|\alpha|\leq k-1} \mathcal{C}_\alpha \left(\mathbf{x}_i - \mathbf{x}^*\right)^\alpha \tag{6.7}$$

with

$$C_\alpha = \frac{2^{|\alpha|}}{\alpha!} \sum_{j=1}^{N} w_j e^{-\frac{\|\boldsymbol{\xi}_j-\mathbf{x}^*\|^2}{h^2}} \left(\frac{\boldsymbol{\xi}_j - \mathbf{x}^*}{h^2}\right)^\alpha .$$

Considering the rapidly decreasing of the Gaussian function, the space could be divided into cells, collecting the influences of the centers. In this way, by choosing a "cut-off" radius r_x for each evaluation point, only the cells lying within r_x are taking into account in the summation.

To this aim, chosen p different cells, the N centers $\boldsymbol{\xi}_j$ are divided into the sets: $S_1, ..., S_p$ with corresponding center $c_1, ..., c_p$. After the partition of the points is completed, the truncation number k is chosen for each cell, in order to obtain the precision required. For each $p-$th cell with center c_p, the influence of data $\boldsymbol{\xi}_j$ is computed

$$\mathcal{C}^p_\alpha = \frac{2^{|\alpha|}}{\alpha!} \sum_{\boldsymbol{\xi}_j\in S_p} w_j e^{-\frac{\|\boldsymbol{\xi}_j-\mathbf{c}_p\|^2}{h^2}} \left(\frac{\boldsymbol{\xi}_j - \mathbf{c}_p}{h}\right)^\alpha . \tag{6.8}$$

Thus for each evaluation point $\mathbf{x}_i$ the fast summation is found

$$\hat{G}(\mathbf{x}_i) = \sum_{\|\mathbf{x}_i-\mathbf{c}_p\|\leq r_x} \sum_{\alpha\leq k_{max}-1} \mathcal{C}^p_\alpha e^{-\frac{\|\mathbf{x}_i-\mathbf{c}_p\|^2}{h^2}} \left(\frac{\mathbf{x}_i - \mathbf{c}_p}{h}\right)^\alpha , \tag{6.9}$$

where k_{max} is the maximum truncation order.

Depending on the truncation of Taylor series and on the value of the cut-off radius r_x, the upper error bound can be estimated

$$\sum_j |w_j| \left(\frac{2^k}{k}\rho_\xi^k \rho_x^k + e^{-\left(\frac{\rho_x}{h}\right)^2}\right) \tag{6.10}$$

with ρ_ξ the upper bound of $\left(\boldsymbol{\xi}_j - \mathbf{x}^*\right)$ and ρ_x the upper bound of $(\mathbf{x}_i - \mathbf{x}^*)$.
Yang, considerably improved the original fast summation either in term of computational cost and in accuracy. However some problems could arise when the value of the smoothing length is low, such as in our case. In fact, in this case the error increases and it is necessary increasing the number p of cells and the truncation order k, making the procedure inefficient again.
To avoid this problem in [82] a tree-data structure is employed to speed up the research for fixed-radius nearest neighborood, in partitioning the data $\boldsymbol{\xi}_j$. Thus the n_c influential cells can be found in $\mathcal{O}(n_c logp)$ time.
If h is considerably low, it is better to find the $\boldsymbol{\xi}_j$ involved and compute the direct summation. Therefore, considering the data distribution, the smoothing length and the bound error required, the new routine chooses the best computation strategy between the following four:

1. Direct Evaluation
2. Direct Evaluation with tree-data structure
3. Improved Fast Gaussian Transform
4. Improved Fast Gaussian Transform with tree data structure.

In particular, after the best alternative is chosen, it is automatically found the best maximum truncation order k_{max} and the optimal number of cells p. Indicating with n_c and n_s the number of the cells and the data sites inside the radius r_x, the computational for the different strategy are reported on Table 6.1.

Table 6.1: Computational cost using the four different strategies

Cost direct	$\mathcal{O}(dMN)$
Cost direct +tree	$\mathcal{O}(d(N + Mn_s)logN)$
Cost IFGT	$\mathcal{O}(dNlogp + (N + Mn_c)r_{(k_{max}-1)d} + dMp)$
Cost IFGT+tree	$\mathcal{O}(N + Mn_c)(dlogp + r_{(k_{max}-1)d})$

In the next section we will show the computational performance in applying the IFGT strategies to our improved SPH method.

6.2 IFGT vs SPH

Opportunely combining the SPH method with the IFGT considerably speed up the method at a large number of evaluation points, by maintaining the accuracy order.
Each entries of the matrix $\mathbf{A}^{(k)}$ and $\mathbf{b}^{(k)}$ requires a summation and it is computed by using the IFGT with different weights, depending on the derivatives of the kernel. The algebra involved is quite tedious but thanks to the features of the Gaussian derivatives, we can exploit of a sort of symmetry and re-use terms already computed.
To make the discussion as simpler as possible, let consider $k = 1$ and $d = 2$, so we obtain a 3×3 system to build. In this case six fast summations are required:

$$\mathbf{1}_{IFGT} := \sum_{j=1}^{N} d\Omega_j \mathsf{K}(\mathbf{x}, \xi_j; h)$$

$$\mathbf{2}_{IFGT} := \sum_{j=1}^{N} (d\Omega_j \xi_j^{(1)}) \mathsf{K}(\mathbf{x}, \xi_j; h)$$

$$\mathbf{3}_{IFGT} := \sum_{j=1}^{N} (d\Omega_j \xi_j^{(2)}) \mathsf{K}(\mathbf{x}, \xi_j; h)$$

$$\mathbf{4}_{IFGT} := \sum_{j=1}^{N} (d\Omega_j \xi_j^{(1)} \xi_j^{(1)}) \mathsf{K}(\mathbf{x}, \xi_j; h)$$

$$\mathbf{5}_{IFGT} := \sum_{j=1}^{N} (d\Omega_j \xi_j^{(1)} \xi_j^{(2)}) \mathsf{K}(\mathbf{x}, \xi_j; h)$$

$$\mathbf{6}_{IFGT} := \sum_{j=1}^{N} (d\Omega_j \xi_j^{(2)} \xi_j^{(2)}) \mathsf{K}(\mathbf{x}, \xi_j; h)$$

these are coupled with different weights giving rise to the corrective matrix $\mathbf{A}^{(1)}$:

$$A_{11}^{(1)} = \mathbf{1}_{IFGT}$$

$$A_{12}^{(1)} = \mathbf{2}_{IFGT} - x_i^{(1)} \mathbf{1}_{IFGT}$$

$$A_{13}^{(1)} = \mathbf{3}_{IFGT} - x_i^{(2)} \mathbf{1}_{IFGT}$$

$$A_{21}^{(1)} = \tfrac{2}{h^2} A_{12}^{(1)}$$

$$A_{22}^{(1)} = \tfrac{2}{h^2} [\mathbf{4}_{IFGT} + (x_i^{(1)})^2 \mathbf{1}_{IFGT} + 2 x_i^{(1)} \mathbf{2}_{IFGT}]$$

$$A_{23}^{(1)} = \frac{2}{h^2}[\mathbf{5}_{IFGT} - x_i^{(2)} f2_{IFGT} - x_i^{(1)} \mathbf{3}_{IFGT} - x_i^{(1)} x_i^{(2)} \mathbf{1}_{IFGT}]$$

$$A_{31}^{(1)} = \frac{2}{h^2} A_{13}^{(1)}$$

$$A_{32}^{(1)} = \frac{2}{h^2} A_{23}^{(1)}$$

$$A_{33}^{(1)} = \frac{2}{h^2}[\mathbf{6}_{IFGT} + (x_i^{(2)})^2 \mathbf{1}_{IFGT} - 2x_i^{(2)} \mathbf{3}_{IFGT}].$$

The Figure 6.2 compares the cost of direct summation versus the IFGT summation and shows the efficiency greatly improved by making use of the IFGT. We compare the CPU times which need to generate and to solve the linear system (5.17) with or without the IFGT for k=1 and k=2 with the same approximation error referring to the test function (5.7a) with data in Ξ_G. In the Tables 6.2 and 6.3 the CPU times for k=1 and k=2 respectively with gridded and random data in approximating the test function (5.7a) are reported. The simulations are conducted on a computer equipped with a processor Intel(R) Core (TM) i7-3537U CPU 2.00GHz.

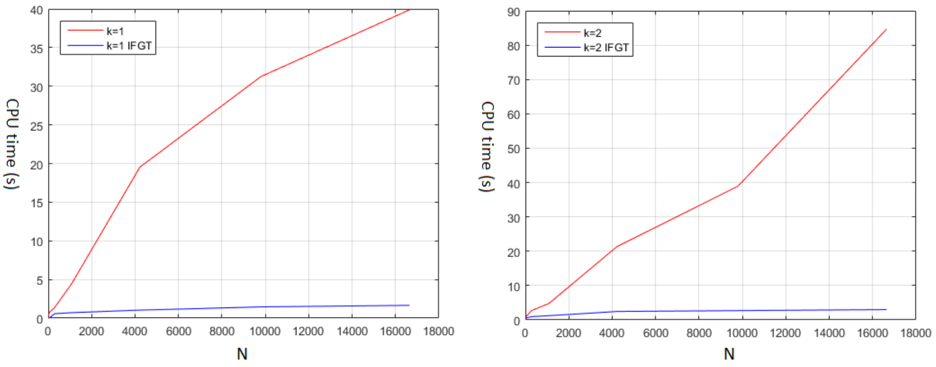

Figure 6.2: CPU times (s) versus N in Ξ_G: (a) k=1; (b) k=2.

In this second part of the thesis we have analyzed a particular class of meshless method: the particle methods, focusing on the Smoothed Particle Hydrodynamics. We present an improved SPH strategy based on Taylor series expansion to restore the accuracy of the standard method. Through several numerical investigations we give evidence of the enhancements in approximating a function and its derivatives. We work with a

Table 6.2: CPU times (s) versus N. Data in Ξ_G. Test function(5.7a).

N	k=1	k=1	k=2	k=2
		IFGT		IFGT
9	0.1539	0.0255	0.7095	0.1756
81	0.8124	0.0264	1.3353	0.4532
289	1.3506	0.5747	2.7261	0.9541
1089	4.4933	0.7062	4.8085	1.2359
4225	19.5425	1.0367	21.3708	2.4587
16641	39.8844	1.6538	84.6397	3.0125

Table 6.3: CPU times (s) versus N. Data in Ξ_R. Test function(5.7a).

N	k=1	k=1	k=2	k=2
		IFGT		IFGT
9	0.5099	0.0253	0.6818	0.1856
81	0.7778	0.0341	1.0210	0.4232
289	1.3719	0.5747	1.3925	0.9824
1089	3.6146	0.7062	3.6724	1.2523
4225	10.6324	1.0985	16.0703	2.6577
16641	42.3251	1.5315	79.7602	3.1543

Gaussian kernel that it is infinitely differentiable, radial and strictly positive definite function. This choice allows us to employ a IFGT strategies to speed up the computational cost.

We address the basic features of the method, conducting many experiments with various data sets and considering several bi-variate test functions. Satisfactory results and computational advantages with uniform and non uniform large data sets encourage to proceed in the approximation of a function and its derivatives with the combined methodology.

Chapter 7

Conclusions and Future Work

This thesis presents new and accurate numerical strategies working with meshless methods in the study of dynamical models and in the approximation field.

In the first part, we have presented a numerical tool for better understanding of dynamical phenomena.

The goal is to reconstruct the domains of attractions of a particular model in order to know in advance all the possible outcomes. To accomplish this task, we have developed an algorithm to detect and to reconnect the threshold points lying between two different basins. Considering the vector field topology, we have demonstrated that the separatrix surfaces are the invariant manifolds of the saddle points. Therefore a new detection strategy has been shown. Comparing to the bisection method, the computational effort is considerably reduced. In particular, this new algorithm could be applied to more complex systems, admitting periodic stable configurations, such as limit cycle or limit torus.

Once the invariant manifolds are detected, we reconstruct them by employing a Moving Least Squares (MLS) mesh-free approximant. This method presents a number of advantages dealing with the scattered data problems. In fact, we do not need to face with any linear systems. Instead, we have to solve small weighted problems depending on the different evaluation points. In particular, working with bi-dimensional data measurements, as in our applications, the explicit formula for the Lagragian multipliers are found. As result the computational cost is further reduced.

The several numerical applications have shown as the separatrix is a fundamental key to better interpret the dynamical process that could not emerged from a standard equilibrium and stability analysis. For example, we have provided a study on the Allee effect induced by the hunting cooperation coupled with an infectious disease. Dealing with a three dimensional systems was impossible to study the Allee threshold without the separatrix reconstruction. The results obtained, show interesting insights on the classification of the Allee effects, enlightening that for a strong cooperation the Allee threshold approaches zero. Therefore the strong Allee effect previously observed, actually is more similar to the weak one and the predators almost always coexist with the prey, reducing the bistability to an only possible outcome. Being the critical population density needed for survival, the Allee threshold is important, especially when it comes to population management.

The proposed algorithm works for almost all the dynamical models, however, if the system admits a focus saddle with strong circulation, the detection of the separatrix points results less accurate. Therefore, future developments are focused on working to couple the old bisection method with the new strategy, in order to preserve the goodness of approximation and the efficiency of the method in this particular case.

In the second part, we have presented a new modified Smoothed Particle Hydrodynamics method based on the Taylor series expansion. Many numerical tests have been shown to give evidence of the accuracy, convergence and computational cost. It has been demonstrated that the method provides concurrently, accuracy of any order in approximating a function and order $k+1-p$ to approximate the $p-th$ derivative.

Dealing with the infinitely smooth differentiable Gaussian kernel functions it has been possible using the Improved Fast Gauss Transform to reduce the computational demanding in assembly the system matrices. The satisfactory results and the computational advantages obtained with different data distributions, encourage to proceed in the approximation of a function and its derivatives with this new methodology.

This work has wide possibilities for future developments. In particular, the research will investigate the application of the IFGT to enhance a meshfree solver, for the analysis of the electromagnetic fields over time. Moreover, we will focus on developing new iterative strategies in order to avoid the generation of the linear systems in improving the SPH approximation.

Bibliography

[1] G. Ala, G.E. Fasshauer, E. Francomano, S. Ganci and M.J. McCourt, A meshfree solver for the MEG forward problem, IEEE Transactions on Magnetics, Vol. 51(3), 5000304 (2015).

[2] G. Ala, G.E. Fasshauer, E. Francomano, S. Ganci and M.J. McCourt, An augumented MFS approach for brain activity reconstruction, Mathematics and Computers in Simulation, Article in press, DOI 10.1016/j.matcom.2016.11.009 (2017).

[3] G. Ala and E. Francomano, Numerical Investigations of an Implicit Leapfrog Time-Domain Meshless Method, Journal on Scientific Computing, Vol. 62(3), 898–912 (2014).

[4] G. Ala, G.E. Fasshauer, E. Francomano, S. Ganci and M.J. McCourt, The method of Fundamental Solutions in solving coupled boundary value problems for M/EEG, SIAM, Journal on Scientific Computing, Vol. 37, Issue 4, B570–B590 (2015).

[5] W.C. Allee, Animal Aggregations. A study in General Sociology. University of Chicago Press, Chicago (1931).

[6] G. Backus and F. Gilbert, The resolving power of gross earth data, Geophys. J. R. Astr. Soc., Vol. 16, 169–205 (1968).

[7] A.M. Bate and F.M. Hilker, Complex Dynamics in an Eco-epidemiological Model, Bull. Math. Biol., Vol. 75, 2059–2078 (2013).

[8] A.M. Bate and F.M. Hilker, Disease in group-defending prey can benefit predators, Theoretical Ecology, Vol. 7, 87–10 (2014).

[9] R. Batra and L. Hesselink, Topology based vector field comparison using graph methods, In Proceeding IEEE Visualization '99, 25–28 (1999).

[10] S.K. Behera and T. Yamagata, Influence of the Indian Ocean Dipole on the Southern Oscillation, Journal of the Meteorological Society of Japan. Ser. II, Vol. 81, Issue 1, 169–177 (2003).

[11] B.E. Beisner, D.T. Haydon and K. Cuddington, Alternative stable states in ecology, Frontiers in Ecology and the Environment, Vol. 1, 376–382 (2003).

[12] T. Belytschko, Y. Krongauz, J. Dolbow and C. Gerlach, On the completeness of meshfree methods, Int J Numer Methods Eng, Vol. 43, 785–819 (1998).

[13] L. Berec, D.S. Boukal and M. Berec, Linking the Allee effect, sexual reproduction, and temperature-dependent sex determination via spatial dynamics, American Naturalist, Vol. 157, 217–230 (2001).

[14] L. Berec and D.S. Boukal, Implications of mate search, mate choice and divorce rate for population dynamics of sexually reproducing species. Oikos, Vol. 104, 122–132 (2004).

[15] K. Binder, The Monte Carlo method in condensed matter physics, Springer Berlin (1988).

[16] J. Bonet and S. Kulasegaram, Correction and stabilization of smooth particle hydrodynamics methods with applications in metal forming simulations, Int J Numer Methods Eng, Vol. 47, 1189–1214 (2000).

[17] D.D. Briske, S.D. Fuhlendorf and F.E. Smeins, A unified framework for assessment and application of ecological thresholds, Rangeland Ecology & Management, Vol. 59, 225–236 (2006).

[18] M. Cardenas-Garcia, J. Andres Arzola Flores and P. Pardo Ruiz, Nonlinear dynamical model for a cancer cell death, Journal of Advances in Biology, Vol. 9, Issue 2, 1862-1865 (2016).

[19] S.R. Carpenter, D. Ludwig and W.A. Brock, Management of eutrophication for lakes subject to potentially irreversible change, Ecological Applications, Vol. 9, 751–771 (1999).

[20] R. Cavoretto, S. De Marchi, A. De Rossi, E. Perracchione and G. Santin, Approximating basins of attraction for dynamical systems via stable radial bases, AIP Conference Proceedings, Vol. 1738, 390003-1–390003-4 (2016).

[21] R. Cavoretto, S. Chaudhuri, A. De Rossi, E., F. Moretti, M.C. Rodi and E. Venturino, Approximation of Dynamical System's Separatrix Curves, AIP Conference Proceedings, ICNAAM, 1389-1220–1389-1223 (2011).

[22] R. Cavoretto, A. De Rossi, E. Perracchione and E. Venturino, Graphical Representation of separatrices of attraction basins in two and three-dimensional dynamical systems, International Journal of Computational Methods, Vol. 14, 1750008-1–1750008-16 (2017).

[23] R. Cavoretto, A. De Rossi, E. Perracchione and E. Venturino, Robust approximation algorithms for the detection of attraction basins in dynamical systems, Journal of Scientific Computing, Vol. 68, 395–415 (2016).

[24] R. Cavoretto, A. De Rossi, E. Perracchione and E. Venturino, Reliable approximation of separatrix manifolds in competition models with safety niches, International Journal of Computer Mathematics, Vol. 92, 1826–1837 (2015).

[25] S. Chen and G.D. Doolen, Lattice Boltzmann method for fluid flows, Annual Review of Fluid Mechanics, Vol. 30, 329–346 (1998).

[26] X. Chen and J.H. Jung, Matrix stability of multiquadric radial basis function methods for hyperbolic equations with uniform centers, Journal of Scientific Computing, Vol. 51(3), 683–702 (2012).

[27] A. Chowdhury, A. Wittek, K. Miller and G.R. Joldes, An element free galerkin method based on the modified moving least squares approximation, Journal of Scientific Computing, 1–15 (2016).

[28] F. Courchamp, L. Berec and J. Gascoigne, Allee Effects in Ecology and Conservation. Oxford University Press, New York (2008).

[29] F. Courchamp and D.W. Macdonald, Crucial importance of pack size in the African wild dog, Lycaon pictus, Animal Conservation, Vol. 4, 169–174 (2001)

[30] S. Creel and N.M. Creel, Communal hunting and pack size in African wild dogs, Animal Behavior, Vol. 50, 1325–1339 (1995).

[31] P. Espanol, Fluid particle model, Physical Review E, Vol. 57, Issue 3, 2930-2948 (1998).

[32] G.E. Fassahuer, Meshfree Approximation Methods with MATLAB, World Scientific Publishing Co., Singapore (2007).

[33] G.E. Fasshauer and M. McCourt, Kernel-based Approximation Methods using MATLAB, Interdiscip. Math. Sci., Vol. 19, World Scientific (2015).

[34] E. Francomano, F.M. Hilker, M. Paliaga and E. Venturino, An efficient method to reconstruct invariant manifolds of saddle points, Dolomites Research Notes on Approximation, Vol.10, 25–30 (2017).

[35] E. Francomano, F. Hilker, M. Paliaga and E. Venturino, Analysis of the Allee threshold via moving least square approximation, Proceedings of Dolomites Workshop on Constructive, Approximation and Applications (DWCAA) (2016).

[36] E. Francomano, F.M. Hilker, M. Paliaga and E. Venturino, On Basins of Attraction for a Predator-Prey Model Via Meshless Approximation, AIP Conference Proceedings, Vol. 1776, 070007-1–07007-4 (2016).

[37] E. Francomano, F.M. Hilker, M. Paliaga and E. Venturino, Separatrix reconstruction to identify tipping points in an eco-epidemiological model, Applied Mathematics and Computation, Vol. 318, 80–91 (2018).

[38] E. Francomano and M. Paliaga, Detecting 3D multistability with a meshfree reconstruction of invariant manifolds of saddle point, Mathematical Methods in the Applied Sciences, DOI: 10.1002/mma.4889 (2018).

[39] E. Francomano and M. Paliaga, Highlighting numerical insights of an efficient SPH method, Applied Mathematics and Computation, Vol.339, 899-915 (2018).

[40] E. Francomano and M. Paliaga, Towards an efficient meshfree solver, AIP Conference Proceedings, Vol. 1776, 070008 (2016).

[41] R.A. Gentry, R.E. Martin and B.J. Daly, An Eulerian differencing method for unsteady compressible flow problems. Journal of Computational Physics, Vol. 1, 87–118 (1966).

[42] G. Gimmelli, B.W. Kooi and E. Venturino, Ecoepidemic models with prey group defense and feeding saturation, Ecological Complexity, Vol. 22, 50–58 (2015)

[43] R.A. Gingold and J.J. Monaghan, Kernel estimates as a basis for general particle method in hydrodynamics, J. Comput. Phys., Vol. 46, 429–453 (1982).

[44] R.A. Gingold and J.J. Monaghan, Smoothed particle hydrodynamics: theory and application on spherical stars, Monthly Notices Roy. Astronom. Soc., Vol. 181, 375–389 (1977).

[45] A. Globus, C. Levitt and T. Lasinski, A tool for visualizing of three dimensional vector field, Proceedings or the 2nd Conference on Visualization 1991, 33–40 (1991).

[46] G.H. Golub and C.F. Van Loan, Matrix Computations, 4th edn. Johns Hopkins, University Press, Baltimore, MD (2012).

[47] M. Griebel, M.A. Schweitzer, Meshfree Methods for Partial Differential Equations II, Lectures Notes in Computational Science and Engineering, Vol. 43 (2005).

[48] L. Greengard and J. Strain, The fast Gauss transformation. SIAM J. Sci. Statist. Comput., Vol. 12(1), 79–94 (1991).

[49] L. Greengard and V. Rokhlin, A fast algorithm for particle simulations, Journal of computational physics, Vol. 135, 280–292 (1997).

[50] D.M. Grobman, Homeomorphisms of systems of differential equations, in Doklady Akademii Nauk SSSR, Vol. 128, 880–881 (1959).

[51] P.M. Groffman, J.S. Baron, T. Blett, A.J. Gold, I. Goodman, L.H. Gunderson, B.M. Levinson, M.A. Palmer, H.W. Paerl, G.D. Peterson, N.L. Poff, D.W. Rejeski , J.F. Reynolds, M.G. Turner, K.C. Weathers and J. Wien, Ecological thresholds: The key to successful environmental management or an important concept with no practical application?, Ecosystems, Vol. 9, 1–13 (2006).

[52] J. Guckenheimer and P.J. Holmes, Nonlinear Oscillations, Dynamical Systems, and Bifurcations of Vector Fields, Applied Mathematical Sciences, Vol. 42, Berlin, New York: Springer-Verlag (1997).

[53] J.H. Halton, On the efficiency of certain quasi-random sequences of points in evaluating multi-dimensional integrals, Num. Math. 2, 84–90 (1960).

[54] F.H. Harlow, The particle-in-cell method for numerical solution of problems in fluid dynamics, Proceedings of Symposia in Applied Mathematics (1963).

[55] F.H. Harlow, The particle-in-cell computing method for fluid dynamics, In Methods in Computational Physics, Fundamental Methods in Hydrodynamics, Vol. 3, Academic Press, New York (1964).

[56] P. Hartman, A lemma in the theory of structural stability of differential equations, in Proc. A.M.S., Vol. 11, Issue 4, 610–620 (1960).

[57] J. Helman and L. Hesselink, Visualizing vector field topology in fluid flows, IEEE Computer Graphics and Applications 11 (May), 36–46 (1991).

[58] F.M. Hilker, M. Paliaga and E. Venturino, Diseased Social Predators, Bull. Math. Biol., Vol. 79, Issue 10, 2175-2196 (2017).

[59] P.J. Hoogerbrugge, J.M.V.A. and Koelman, Simulating microscopic hydrodynamic phenomena with dissipative particle dynamics, Europhysics Letters, Vol. 19, Issue 3, 155–160 (1992).

[60] C.S. Holling, Resilience and stability of ecological systems, Annual Review of Ecology and Systematics, Vol. 4, 1–23 (1973).

[61] G.R. Joldesa, H.A. Chowdhurya, A. Witteka, B. Doylea and K. Millera, Modified moving least squares with polynomial bases for scattered data approximation, Applied Mathematics and Computation, Vol. 266, 893–902 (2015).

[62] Y. Kang, S.K. Sasmal, A.R. Bhowmick and J. Chattopadhyay, Dynamics of a predator-prey system with prey subject to Allee effects and disease, Mathematical Biosciences and Engineering, Vol. 11, Issue 4, 877–918 (2014).

[63] J. Krause and G.D. Ruxton, Living in groups. Oxford University Press, Oxford (2002).

[64] P. Lancaster and K. Salkauskas, Surfaces generated by Moving Least Squares Methods, Mathematics of Computation, Vol. 37, 115, 141-158 (1981).

[65] R.C. Lewontin, The meaning of stability, Brookhaven Symposia in Biology, Vol. 22, 13–24 (1969).

[66] B. Li, F. Habbal and M. Ortiz, Optimal transportation meshfree approximation schemes for fluid and plastic flows, J. Numer. Meth. Engng, Vol. 83, 1541–1579 (2010).

[67] L.D. Libersky and A.G. Petscek, Smooth particle hydrodynamics with strength of materials, Proceedings of the next free-lagrangian method, Vol. 35, Springre, 248–257 (1991).

[68] G.R. Liu and M.B. Liu, Smoothed Particle Hydrodynamics - A Mesh-Free Particle Method, World Scientific Publishing, Singapore (2003).

[69] M.B. Liu, and G.R. Liu, Smoothed particle hydrodynamics (SPH): An overview and recent developments, Archives of Computational Methods in Engineering, Vol. 17(1), 25–76 (2010).

[70] M.B. Liu, G.R. Liu and K.Y. Lam, Constructing smoothing functions in smoothed particle hydrodynamics with applications, J. Comput. Appl. Math., Vol. 155, 263–284 (2003).

[71] M.B. Liu, W.P. Xie and G.R. Liu, Restoring particle inconsistency in smoothed particle hydrodynamics, Appl. Numer. Math., Vol. 56(1), 19–36 (2006).

[72] W.K. Liu, S. Jun and Y.F. Zhang, Reproducing kernel particle methods, Int. Jour. Meth. Fluids, Vol. 20(8–9), 1081–1106 (1995).

[73] L.B. Lucy, A numerical approach to the testing of fusion process, Astron J, Vol. 82, 1013–1024 (1977).

[74] A.M. Lyapunov, Stability of Motion, Academic Press, New-York London (1966).

[75] R.M. May, Thresholds and breakpoints in ecosystems with a multiplicity of stable states, Nature, Vol. 269, 471–477 (1977).

[76] N. Metropolis and S. Ulam, The Monte Carlo method, Journal of American Statistical Association, Vol. 44, 335–341 (1949).

[77] T.A. McMahon, R.M. Vogel, M.C. Peel and G.S Pegram, Global streamflows: Characteristics of annual streamflows, Journal of Hydrology, Vol. 347, 243–259 (2007).

[78] J.J. Monaghan and J.C. Lattanzio, A refined particle method for astrophysical problems, Astron Astrophys, Vol. 149, 135–143 (1985).

[79] J.J. Monaghan, An introduction to SPH, Comput Phys Commun, Vol. 48, 89–96 (1988).

[80] J.J. Monaghan, Smoothed particle hydrodynamics, Ann Rev Astron Astrophys, Vol. 30, 543–574 (1992).

[81] J.J. Monaghan, Simulating free surface flows with SPH. Journal of Computational Physics, Vol. 110, 399–406 (1994).

[82] V.I. Morariu, B.V. Srinivasan, V.C. Raykar, R. Duraiswami and L.S. Davis, Automatic online tuning for fast Gaussian summation, Advances in Neural Information Processing Systems (NIPS 2008), Vol. 21, 1113–1120 (2009).

[83] J.P. Morris, Analysis of smoothed particle hydrodynamics with applications, Ph. D. thesis, Monash University (1996).

[84] P.J. Mumby, A. Hastings and H.J. Edwards, Thresholds and the resilience of Caribbean coral reefs, Nature, Vol. 450, 98–101 (2007).

[85] J.D. Murray, Mathematical Biology I: An Introduction, third edition. Springer, New York (2002).

[86] S. Philip and G. Jan van Oldenborgh, Shifts in ENSO coupling processes under global warming, Geophysical Research Letters, Vol. 33, L11704 (2006).

[87] R.M. Peterman, A simple mechanism that causes collapsing stability regions in exploited salmonid populations, Journal of Fisheries Research Board of Canada, Vol. 34, 1130–1142 (1977).

[88] P. Petraitis, Multiple Stable States in Natural Ecosystems. Oxford University Press, Oxford (2013).

[89] R. Precup, M.A. Serban and D. Trif, Asymptotic stability for a model of cell dynamics after allogenic bone marrow transplation, Nonlinear Dynamics and Systems Theory, Vol. 13, Issue 1, 79–92 (2013).

[90] Y.H. Qian, S. Succi and S.A. Orszag, Recent advances in lattice Boltzmann computing, In Stauffer (Ed.): Annual Reviews of Computational Physics, Volume III, World Scientific, Singapore (2000).

[91] R.J. Renka and R. Brown, Algorithm 792 : accuracy test of ACM algorithms for interpolation of scattered data in the plane. ACM Trans. Math. Softw., Vol. 25, 78–94 (1999).

[92] Z. Ratajczak, J.B. Nippert and T.W. Ocheltree, Abrupt transition of mesic grassland to shrubland: evidence for thresholds, alternative attractors, and regime shifts. Ecology, Vol. 95, 2633–2645 (2004).

[93] D.R. Rubenstein and I.J. Lovette, Temporal Environmental Variability Drives the Evolution of Cooperative Breeding in Birds, Current Biology, Vol. 17, Issue 16, 1414–1419 (2007)

[94] V. Raykar, C. Yang, R. Duraiswami, and N. Gumerov. Fast computation of sums of Gaussians in high dimensions, UMD-CS-TR-4767, (2005).

[95] D. Ruelle, Ergodic theory of differentiable dynamical system, Publications Mathematiques de l'Institut des Hautes Etudes Scientifiques, Vol.50, Issue 1, 27–58 (1979)

[96] M. Scheffer, Critical Transitions in Nature and Society. Princeton University Press, Princeton (2009).

[97] D. Shepard, A two dimensional interpolation function for irregularly spaced data, Proc. 23rd Nat. Conf. ACM,517–524 (1968).

[98] H.F. Schwaiger, An implicit corrected SPH formulation for thermal diffusion with linear free surface boundary conditions, International Journal for Numerical Methods in Engineering, Vol. 75(6), 647–671 (2008).

[99] C. Shu, H.Ding and K.S. Yeo, Local radial basis function-based differential quadrature method and its application to solve two-dimensional incompressible Navier-Stokes equations, Comput. Methods Appl. Mech. Eng. , Vol. 192(7-8), 941–954 (2003).

[100] I.M. Sobol, Distribution of points in a cube and approximate evaluation of integrals, U.S.S.R Comput. Maths. Math. Phys., Vol. 7, 86–112 (1967).

[101] P.E. Stander, Cooperative hunting in lions: role of individual. Behavioral Ecology and Sociobiology, Vol. 29, Issue 6, 445–454 (1992).

[102] J.P. Sutherland, Multiple stable points in natural communities. American Naturalist, Vol. 108, 859–873 (1974).

[103] J.W. Swegle,D.L. Hicks and S.W. Attaway, Smoothed particle hydrodynamics stability analysis, Journal of Computational Physics, Vol. 116, Issue 1, 123–134 (1995).

[104] M. Teixeira Alves and F.M. Hilker, Hunting cooperation and Allee effects in predators, Journal of Theoretical Biology, Vol. 419, 13–22 (2017).

[105] W.I. Thacker, W.I. Zhang, L.T Watson, J.B. Birch, M.A. Iyer and M.W. Berry, Algorithm 905: SHEPPACK-modified Shepard algorithm for interpolation of scattered multivariate data, ACM Trans. Math. Softw., Vol. 37(3), 1–20 (2010).

[106] H. Theisel, T. Weinkauf, H.C. Hege and H.P. Seidel, Saddle Connectors- an approach to visualizing the topological skeleton of complex 3D vector fields, Visualization, IEEE (2003).

[107] X. Tricoche, G. Scheuermann, and H. Hagen, A topology simplification method for 2D vector fields. In Proc. IEEE Visualization, 359–366 (2000).

[108] I. Trotts, D. Kenwright and R. Haimes, Critical points at infinity: a missing link in vector field topology, In Proc. NSF/DoE Lake Tahoe Workshop on Hierarchical Approximation and Geometrical Methods for Scientific Visualization (2000).

[109] H. Wendland, Scattered Data Approximation. Cambridge University Press, Cambridge (2010).

[110] T. Wishgoll and G. Scheuermann, Detection and visualization of closed streamlines in planar flows, IEEE Transactions on Visualization and Computer Graphics Vol. 7, Issue 2, 165â-172 (2001).

[111] S. Wolfram, Cellular Automata, Los Alamos Science, Vol. 9, 2–21 (1983).

[112] C. Yang, R. Duraiswami, N. A. Gumerov, and L. S. Davis. Improved fast Gauss transform and efficient kernel density estimation,Proceedings Ninth IEEE International Conference on Computer Vision, (2003).

[113] C. Yang, R. Duraiswami and L. S. Davis. Efficient kernel machines using the improved fast Gauss transform, Advances in neural information processing systems, (2004).